MULTISCALE SOLUTION TECHNIQUES FOR HIGH-CONTRAST ANISOTROPIC PROBLEMS

A Dissertation

by

JUN REN

Submitted to the Office of Graduate and Professional Studies of
Texas A&M University
in partial fulfillment of the requirements for the degree of

DOCTOR OF PHILOSOPHY

Chair of Committee,	Yalchin Efendiev
Committee Members,	Michael King
	Raytcho Lazarov
	Jay R. Walton
Head of Department,	Emil Straube

December 2015

Major Subject: Mathematics

ABSTRACT

Anisotropy occurs in a wide range of applications. Examples include porous media, composite materials, heat transfer, and other fields in science and engineering. Due to the anisotropy, the physical property could vary significantly only in certain directions. As such, the discrete problem will have a very large condition number for traditional numerical methods. In addition, many anisotropic materials contain multiple scales and their physical properties could vary in orders of magnitude. These large variations bring an additional small-scale parameter into the problem. Thus, a proper treatment of the anisotropy not only helps to design robust iterative methods, but also provides accurate approximations of the problem.

Various well-developed techniques have been used to address anisotropic problems, such as multigrid methods, adaptive methods, and domain decomposition techniques. More recently, a large class of accurate reduced-order methods have been introduced and applied to many applications. These include multiscale finite element, multiscale finite volume, and mixed multiscale finite element methods.

The primary focus of this dissertation is to study a multiscale finite element method for the approximation of heterogeneous problems involving high-anisotropy, high-contrast, parameter dependency. First, we design robust two-level domain decomposition preconditioners using multiscale coarse spaces. Next, a general formulation of heterogeneous problem is investigated using this multiscale finite element method. Then, a multilevel multiscale finite element method is proposed and analyzed to reduce the computational cost. Last, this multiscale finite element method is extended to a convection-diffusion problem.

ACKNOWLEDGEMENTS

I would like to convey my deepest gratitude to my advisor Dr. Yalchin Efendiev, who has always provided me with great support and guidance throughout this work. During my graduate study in Texas A&M University, his strong enthusiasm for knowledge and mathematical rigor encourages me to challenge myself in various aspects of my life. It is an extremely invaluable experience to work with and learn from Yalchin.

I am grateful to the rest of my committee members: Dr. Michael King, Dr. Raytcho Lazarov, and Dr. Jay R. Walton, for their encouragement and insightful comments. I would like to extend my thanks to the Department of Mathematics, Texas A&M University, for the generous financial support over the years.

I would like to express my appreciation to Wing Tat Leung, Dr. Juan Galvis, Dr. Michael Prescho, and Dr. Eric T. Chung, for their stimulating discussions and help. They are always helpful, enthusiastic and informative.

Last but not least, my greatest gratitude goes to my wife, my parents, and parents-in-law, for their unconditional support and endless love throughout my studies. I dedicate this dissertation to my family, with all my heart.

TABLE OF CONTENTS

LIST OF FIGURES

LIST OF TABLES

I INTRODUCTION

I.1 Background and motivation

Many problems arising from various physical and modern engineering applications are multiscale in nature. Examples include porous media, composite materials, heat transfer, atmosphere/ocean science, and image processing. These types of problems often involve high-contrast coefficients. For example, fractured media usually have large variations in their conductivity. These large variations bring an additional small-scale parameter into the multiscale problem. Traditional numerical methods for these problems therefore lead to a large ill-conditioned system of linear equations. On the other hand, full resolution of the fine-scale information of the coefficient is often prohibitively expensive. Hence, we wish to design a proper numerical method so that it can efficiently and accurately resolve complex systems.

Furthermore, many natural and man-made materials exhibit anisotropic behavior. The source of anisotropy can be due to the heterogeneous medium and/or highly irregular computational domain geometry over which the solution is sought. For example, in porous media or other applications, high anisotropy can be caused by the presence of fractures or other high conductivity thin inclusions that can have preferred high-conductivity directions. Because of high variations among the background media and fracture conductivities, the conductivity can have high anisotropy at the fine computational-grid scale. On the other hand, the source of anisotropy could have a physical base. Recently, research has been conducted to develop compound materials with anisotropic properties. For example, a cloaking device has been developed in which a material shell is designed to have specific anisotropic acoustic and electromagnetic properties such that it can divert pressure and light

waves around a region of space unscathed. We note that the existence of high-anisotropy brings extra difficulties in numerical computations because of the large condition number of the linear system. It has some additional difficulties compared to isotropic high-contrast problems that we will discuss later. The investigation of numerical methods for such challenging problems has motivated the research which is documented in this dissertation.

Over the past few decades, lots of efforts have been put into the multiscale problems. They include upscaling [9, 20, 22, 46, 54], multiscale finite element [1, 4, 34, 44], multiscale finite volume [21, 45, 47, 48, 49], multiscale finite difference [3], and other multiscale methods [13]. A characteristic of multiscale methods is to recover a fine-scale solution from the coarse-scale solution. The construction of the multiscale solution space distinguishes them from the standard finite element methods. In particular, most multiscale methods have applied local computations for the determination of coarse basis functions. Numerous papers have shown that the standard multiscale methods are suitable for various applications [8, 9, 35, 36, 45]. However, these approaches have proven to be inadequate for solving problems with high-contrast due to the range of scales and the large number of variables involved. Some previous approaches are developed for solving isotropic multiscale problems with high-contrast coefficients [6, 23, 25, 30, 31, 38, 39]. However, the performance of these approaches deteriorate when applied to anisotropic problems. *Because of high anisotropies, numerically solving multiscale problems becomes more difficult and we observe: (1) a comparatively large coarse space may arise due to the highly-anisotropic regions; (2) more computational time may be required because of the large condition numbers; (3) a different testing space is needed to be considered.* Hence, to solve problems involving high-anisotropy, high-contrast, and uncertainties, a more general multiscale method is desirable for constructing a reduced-dimensional approximation of the solution.

In this dissertation, we consider a generalized multiscale finite element method that hinges on the construction of coarse solution space in which a set of locally computed multiscale basis functions are generated. These basis functions generate a solution space, called the snapshot space. Then, some dimension-reduction techniques have been used to reduce the dimension of the snapshot space. The resulting reduced-dimensional space is called the offline space. The offline basis functions that constitute the offline space are coupled via a respective global formulation to compute the global solution. In the case of parameter dependency, where the parameter can represent the uncertainties, an online space is constructed using the offline space to form the multiscale solution space. In the next section, a brief description to each chapter of this dissertation is given.

I.2 Description of the dissertation

In Chapter II, we discuss robust two-level domain decomposition preconditioners for highly-anisotropic heterogeneous multiscale problems. We present a construction of a multiscale coarse space in the two-level overlapping domain decomposition method. The coarse space used in this construction is based on local spectral problems. Two types of partition of unity functions involved in the eigenvalue problem are discussed. We discuss the robustness of the preconditioner with respect to the contrast and the anisotropy of the medium. Analysis and numerical experiments are provided for the validation of robust preconditioners with respect to the number of iterations and the dimension of the coarse space.

A general highly-anisotropic heterogeneous multiscale problem is studied in Chapter III. We solve this problem in the Generalized Multiscale Finite Element Methods (GMsFEM) framework. To construct the multiscale solution space, the GMsFEM framework follows an offline-online procedure. At the offline stage, we first construct

a snapshot space. The snapshot space contains local solutions which can provide an accurate approximation of the solution and can guarantee some conservation properties. Next, using appropriate local spectral decomposition, we identify the offline space, which is a reduced-dimensional space. Then, the offline space is used at the online stage for the creation of the multiscale basis functions to form the online space. These multiscale basis functions can be re-used for any input parameter to solve the problem. The key to the construction of these two spaces (offline and online) is the design of appropriate local spectral problems for identifying dominant modes that can capture important features at the fine scale.

In Chapter IV, we develop a multilevel framework for the GMsFEM. To save the computational cost, a hierarchical construction of the multiscale solution space is proposed. In particular, an expensive part of the computations involves the calculations of snapshot solutions. We propose a nested sequence of snapshot spaces using multilevel grids to save the computational cost without sacrificing much the accuracy. The snapshot space at a given coarse level is built based on the coarse spaces that are computed from the previous finer grids. Our main contribution in this chapter is the innovative algorithm for hierarchically building accurate coarse solution spaces. Some convergence analysis and supporting numerical examples are presented.

In Chapter V, we develop a multiscale method for coupled flow and transport in heterogeneous porous media. We consider convection-dominated transport equations coupled with the flow equations. Mixed finite element framework is used for a coupled system to achieve a mass conservation. Multiscale spaces are constructed using the mixed GMsFEM, which constructs the snapshot spaces and performs a local spectral decomposition in the snapshot space. The resulting approach uses a few multiscale basis functions in each coarse block (for both the pressure and the concentration)

to solve the coupled system. Our main contributions are: (1) the development of a mass conservative GMsFEM for coupled flow and transport; (2) the development of a multiscale method for convection-dominated transport problem by choosing appropriate test and trial spaces within Petrov-Galerkin mixed formulation.

II ROBUST TWO-LEVEL DOMAIN DECOMPOSITION PRECONDITIONERS FOR HIGH-CONTRAST ANISOTROPIC FLOWS IN MULTISCALE MEDIA[1]

II.1 Introduction

In this chapter, we attempt to address the main issues in the design, analysis, and experimental justification of robust preconditioners for finite element systems arising in the approximation of highly anisotropic multiscale diffusion problems [25].

We consider the second order elliptic problem with heterogeneous coefficients in a polygonal domain $\Omega \subset \mathbb{R}^d$, $d = 2, 3$:

$$\begin{aligned} -\mathrm{div}(\kappa(x)\nabla u) &= f \quad \text{in } \Omega, \\ u(x) &= 0 \quad \text{on } \partial\Omega. \end{aligned} \tag{II.1}$$

Here, $\kappa(x) = \{\kappa_{ij}\}_{i,j=1}^d$, $d = 1, 2, 3$, is a heterogeneous spatial conductivity (or permeability) field with multiple scales, high-contrast, and high-anisotropy.

Now, we introduce the concept of material contrast and anisotropy. Assume that $\kappa(x)$ is symmetric and uniformly positive definite in Ω. That is, for each $x \in \Omega$, there are $\kappa_{\max}(x) \geq \kappa_{\min}(x) > 0$ such that $\kappa_{\min}(x) q^T q \leq q^T \kappa(x) q \leq \kappa_{\max}(x) q^T q$, for all $q \in \mathbb{R}^d$. Then, the contrast in κ is defined as

$$\eta = \frac{\max\limits_{x\in\Omega} \kappa_{\max}(x)}{\min\limits_{x\in D} \kappa_{\min}(x)}.$$

[1]Part of the data reported in this chapter is reprinted with permission from "Robust Two-level Domain Decomposition Preconditioners for High-contrast Anisotropic Flows in Multiscale Media" by Yalchin Efendiev, Juan Galvis, Raytcho Lazarov, Svetozar Margenov and Jun Ren. Comput. Methods Appl. Math., Vol.12(4), 2012, pp. 415–436, Copyright [2012] by DE GRUYTER. DOI: 10.2478/cmam-2012-003. http://www.degruyter.com/view/j/cmam.2012.12.issue-4/cmam-2012-0031/cmam-2012-0031.xml

The parameter η is an important physical parameter for highly heterogeneous media. Throughout this dissertation, the value of $\kappa_{\min}$ is not close to zero. Test results for a low $\kappa_{textmin}$, for example 0.0001, will be studied in the future (see [7]). As for the high-anisotropy, we denote $0 < \mu_1(x) \leq \cdots \leq \mu_d(x)$ as the eigenvalues of the matrix $\kappa(x)$ for any $x \in \Omega$, and $q_j(x)$ as the corresponding eigenvectors, $j = 1, \ldots, d$. Note that $\kappa(x)$ has the following property

$$\kappa(x) = \mu_1(x) q_1(x) q_1^T(x) + \cdots + \mu_d(x) q_d(x) q_d^T(x). \tag{II.2}$$

We know that the ratio $\mu_d(x)/\mu_1(x)$ characterizes the anisotropy of this material. In the case of $\mu_d(x)/\mu_1(x) = 1$, i.e. $\mu_1(x) = \mu_2(x) = \cdots = \mu_d(x)$, the material is of isotropy. If $\mu_d(x)/\mu_1(x) >> 1$, then the material becomes highly anisotropic. For example, in 2-D media, where $\mu_2(x) >> \mu_1(x)$ for x in some sub-domain, then this sub-domain represents a high conductivity in the direction of the eigenvector $q_2(x)$. In this chapter, we consider a high-contrast and high-anisotropy problem and we aim to design and theoretically justify iterative methods for the corresponding finite element discretizations of such problem that work for large variations of η, e.g., $\eta \approx 10^8$.

High-contrast problems are quite challenging, but the high-anisotropy adds another dimension of difficulty, which we would like to discuss it in this chapter. An initial discussion on the issues related to the numerical solution of such problems was presented in [25]. In this chapter, we discuss the construction of the preconditioner for such problems and make exhaustive numerical experiments on a series of 2-D problems. Our work is based on recent achievements in overlapping domain decomposition theory [51, 52] and mathematical modeling in highly heterogeneous media like diffusion, conduction, elastic deformations, etc. The case of isotropic media has

been subject to numerous studies, e.g., [6, 23, 25, 30, 31, 38, 39, 41, 42]. We note that the coarse spaces play an essential role in two-level domain decomposition preconditioners. It is also known [25] that, for anisotropic problems, the coarse spaces could have a large dimension. This is due to the fact that the fine-scale features within the regions of high-anisotropy need to be sufficiently represented on a coarse mesh.

In order to make the preconditioners robust with respect to the contrast and the anisotropy, in this chapter, we propose a number of remedies and construct the coarse spaces such that they contain essential features of the fine-scale solution. The construction of the coarse spaces is based on recently introduced methods [23, 39].

The rest of this chapter is organized as follows. In Section II.2, we introduce the finite element method for this problem on a fine mesh that resolves the heterogeneity of the media. In Section II.3, we present the framework of the overlapping domain decomposition method and two-level overlapping Schwarz preconditioners. In Section II.4, we discuss the construction of the coarse solution space. Our numerical experiments are presented in Section II.5. We provide the analysis of the preconditioner in Section II.6 and finish this chapter by offering some concluding remarks in Section II.7.

II.2 Problem formulation

Given a forcing term f, we consider the weak formulation of problem (II.1). We seek $u \in H_0^1(\Omega)$ such that

$$a(u,v) := \int_\Omega \kappa(x)\nabla u \cdot \nabla v dx = \int_\Omega f v dx, \quad \text{for all } v \in H_0^1(\Omega). \tag{II.3}$$

Now, we introduce a Galerkin finite element approximation of (II.3). Let $\mathcal{T}_h$, $0 < h < 1$, be a family of fine triangulations. It is assumed that h is sufficiently

small to capture the spatial variation of $\kappa(x)$. Without loss of generality, we assume that $\kappa_{ij}(x)$, $i,j = 1,\ldots,d$ are piecewise constant functions on each finite element in $\mathcal{T}_h$. We denote by $V^h(\Omega)$ the standard finite element space of continuous and piecewise linear functions with respect to $\mathcal{T}_h$. Denote also by $V_0^h(\Omega)$ the subspace of $V^h(\Omega)$ with vanishing values on $\partial\Omega$. Similar notations, $V^h(D)$ and $V_0^h(D)$, are used for any sub-domain $D \subset \Omega$. Further, we shall refer to the spaces $V_0^h(\Omega)$ and $V^h(\Omega)$ as to fine-grid spaces.

The discrete problem reads as follows. We seek $u \in V_0^h(\Omega)$ such that

$$a(u,v) = f(v) \quad \text{for all } v \in V_0^h(\Omega),$$

or in matrix form

$$Au = b, \tag{II.4}$$

where for all $u, v \in V^h(\Omega)$ (considered as vectors), we have $u^T A v = a(u,v)$ and $v^T b = \int_\Omega fv$. For the notational convenience, we will denote the continuous variables and the corresponding discrete quantities with the same symbols.

II.3 Domain decomposition framework

II.3.1 Overlapping decomposition and local spaces

We introduce a non-overlapping decomposition $\{D_i\}_{i=1}^N$ of Ω that is aligned with the mesh $\mathcal{T}_h$ and denote by $H = \max_i \operatorname{diam}(D_i)$. We denote by $\{D_i'\}_{i=1}^N$ the overlapping decomposition obtained from the original non-overlapping decomposition $\{D_i\}_{i=1}^N$ by enlarging each sub-domain D_i to $D_i' = D_i \cup \{x \in \Omega, \operatorname{dist}(x, D_i) < \delta_i\}$, $i = 1,\ldots,N$. Without loss of generality, we require $\{D_i'\}_{i=1}^N$ is also aligned with the mesh $\mathcal{T}_h$,

Let $V_0^h(D_i')$ be finite element space with support in D_i'. Denote by $R_i^T : V_0^h(D_i') \to$

V^h the extension by zero operator. Then, we define the preconditioner

$$B_{1L}^{-1} = \sum_{i=1}^{N} R_i^T A_i^{-1} R_i, \tag{II.5}$$

where the local matrix $A_i,\ i = 1, \ldots, N$, is defined by

$$v^T A_i w = a(v, w) \quad \text{for all } v, w \in V^i = V_0^h(D_i'). \tag{II.6}$$

In order to improve the robustness with respect to the underlying physical parameters, a coarse space that *helps to propagate information globally* must be added to the preconditioner.

II.3.2 General concept of coarse spaces and two-level method

Given a coarse triangulation $\mathcal{T}_H$ of Ω, we denote by $\{x_i\}_{i=1}^{N_v}$ the interior vertices of $\mathcal{T}_H$ and define its neighborhood

$$\omega_i = \{K \in \mathcal{T}_H; \quad x_i \in \overline{K}\}, \quad i = 1, \ldots, N_v. \tag{II.7}$$

We introduce coarse basis functions (to be specified later) $\{\Phi_{i,\ell}, 1 \leq \ell \leq L_i, 1 \leq i \leq N_v\}$ with $\Phi_{i,\ell}$ supported in ω_i. Here, for each interior node x_i, L_i is an integer that is specified in (II.13) and it is related to the decay of the eigenvalues of the generalized eigenvalue problem (II.10). We re-enumerate the set of basis functions (using a single index) to $\{\Phi_I\}_{I=1}^{N_c}$, $N_c = \sum_{i=1}^{N_v} L_i$, and form the coarse space as

$$V_0 = \text{span}\{\Phi_I\}_{I=1}^{N_c}.$$

We also define the coarse matrix (of size $N_c \times N_c$) by

$$A_0 = R_0 A R_0^T, \tag{II.8}$$

where $R_0^T = [\Phi_1, \ldots, \Phi_{N_c}]$ is the coarse basis functions matrix that maps the coarse space to the fine space. Now, with these coarse matrices A_0 and R_0, we define a two-level additive preconditioner of the form

$$B^{-1} = R_0^T A_0^{-1} R_0 + \sum_{i=1}^{N} R_i^T A_i^{-1} R_i = R_0^T A_0^{-1} R_0 + B_{1L}^{-1}, \tag{II.9}$$

where B_{1L}^{-1} is given by (II.5).

II.4 Coarse space construction

II.4.1 Local eigenvalue problems

In this subsection, we study a multiscale coarse space for the construction of the preconditioner (II.9).

We present a set of localized eigenvalue problems following [23]. In particular, for any neighborhood ω_i related to the coarse node x_i, we introduce the following generalized eigenvalue problem. Find the eigenpair (λ, ψ), $\psi \in \widetilde{V}_h(\omega_i)$ such that

$$\int_{\omega_i} \kappa \nabla \psi \cdot \nabla \phi \, dx = \lambda \int_{\omega_i} \widetilde{\kappa} \psi \, \phi \, dx \quad \text{for all } \phi \in \widetilde{V}_h(\omega_i). \tag{II.10}$$

Here, $\widetilde{V}_h(\omega_i) = V_h(\omega_i) \cap V_0^h(\Omega)$ and $\widetilde{\kappa}$ is a *scalar* defined by

$$\widetilde{\kappa}(x) = H^2 \sum_{j=1}^{N_v} \kappa(x) \nabla \chi_j \cdot \nabla \chi_j, \tag{II.11}$$

where $\{\chi_i\}_{i=1}^{N_v}$ is a partition of unity subordinate to $\{\omega_i\}_{i=1}^{N_v}$. The choice of $\{\chi_i\}_{i=1}^{N_v}$

will be discussed in the next subsection.

The problem (II.10) is equivalent to the following symmetric algebraic eigenvalue problem

$$A^{\omega_i}\psi = \lambda M^{\omega_i}\psi, \tag{II.12}$$

where the matrices A^{ω_i} and M^{ω_i} are defined by

$$v^T A^{\omega_i} w = \int_{\omega_i} \kappa \nabla v \cdot \nabla w dx \quad \text{for all } v, w \in \widetilde{V}^h(\omega_i),$$

and

$$v^T M^{\omega_i} w = \int_{\omega_i} \widetilde{\kappa} v w dx \quad \text{for all } v, w \in \widetilde{V}^h(\omega_i),$$

respectively. Denote its eigenvalues and eigenvectors by $\{\lambda_\ell^{\omega_i}\}$ and $\{\psi_\ell^{\omega_i}\}$, respectively. Now, we order the eigenvalues as $0 \leq \lambda_1^{\omega_i} \leq \lambda_2^{\omega_i} \leq \cdots \leq \lambda_i^{\omega_i} \leq \ldots$. We note that, $\lambda_1^{\omega_i} = 0$ and $\psi_1^{\omega_i}$ is a constant vector.

Once we have the above eigenfunctions, the coarse basis functions are defined by

$$\Psi_{i,\ell} = I^h(\chi_i \psi_\ell^{\omega_i}) \quad \text{for } 1 \leq \ell \leq L_i \text{ and } 1 \leq i \leq N_v, \tag{II.13}$$

where I^h is the fine-grid nodal finite element interpolation operator and L_i is an integer number specified for each $i = 1, \ldots, N_v$. Then, the spectral multiscale space is formed as

$$V_0 = \text{span}\{\Psi_{i,\ell} : 1 \leq \ell \leq L_i \text{ and } 1 \leq i \leq N_v\}. \tag{II.14}$$

Remark II.4.1. *The coarse-space V_0 and the corresponding coarse problems can be used as a multiscale method to approximate, on the coarse-grid, the solution of the problem* (II.3)*, a procedure studied in the case of scalar coefficients in [6, 33]. Convergence to the reference solution (or the fine-grid solution) is expected when*

more and more additional eigenvectors are included in the coarse space.

II.4.2 Partition of unity

In this subsection, we attempt to test two choices of the partition of unity $\{\chi_i\}_{i=1}^{N_v}$ and further discuss the effect of the partition of unity on the dimension of the resulting coarse space.

Case 1: piecewise linear (or bilinear) functions. If we choose $\chi_i = \chi_i^{lin}$ to be piecewise linear (or bilinear) functions [5], then by (II.2) for a 2-D domain, we have

$$\kappa(x)\nabla\chi_i(x)\cdot\nabla\chi_i(x) = \kappa_{\max}(x)(q_{\max}^T(x)\nabla\chi_i^{lin}(x))^2 + \kappa_{\min}(x)(q_{\min}^T(x)\nabla\chi_i^{lin}(x))^2. \tag{II.15}$$

Taking into account (II.15) and the fact that $H^2|\nabla\chi_i^{lin}|^2 = O(1)$, we get the following form of the associated Rayleigh quotient

$$\begin{aligned}
\mathcal{Q}(v) = \frac{v^T A^{\omega_i} v}{v^T M^{\omega_i} v} &= \frac{\displaystyle\int_{\omega_i} \kappa\nabla v\cdot\nabla v}{\displaystyle\int_{\omega_i} \widetilde{\kappa} v^2} \\
&= \frac{\displaystyle\int_{\omega_i} \left(\kappa_{\max}(q_{\max}^T\nabla v)^2 + \kappa_{\min}(q_{\min}^T\nabla v)^2\right)}{\displaystyle H^2\int_{\omega_i}(\sum_j \kappa_{\max}\left(q_{\max}^T\nabla\chi_j^{lin}\right)^2 + \kappa_{\min}(q_{\min}^T\nabla\chi_j^{lin})^2\right) v^2} \\
&\le \frac{\displaystyle\int_{\omega_i} \left(\kappa_{\max}(q_{\max}^T\nabla v)^2 + \kappa_{\min}(q_{\min}^T\nabla v)^2\right)}{\displaystyle H^2\int_{\omega_i}\sum_j \left((\kappa_{\max}-\kappa_{\min})(q_{\max}^T\nabla\chi_j^{lin})^2 + \kappa_{\min}|\nabla\chi_j^{lin}|^2\right) v^2}.
\end{aligned}$$

We see that this quotient is small for functions v that satisfy

- $\nabla v = 0$ for every region where both $\kappa_{\max}(x)$ and $\kappa_{\min}(x)$ have high values;
- $q_{\max}^T\nabla v = 0$ for regions where $\kappa_{\max}(x)$ has high values and $\kappa_{\min}(x)$ is of order

1.

We conclude that the number of small eigenvalues is related to the number of independent functions (that can be represented on the fine grid) that are constant along $q_{\max}$ (that is along trajectories of high-anisotropy) and therefore vary along $q_{\min}$ only.

Case 2: multiscale partition of unity. We propose to use the multiscale finite element partition of unity. This is motivated by the fact that the multiscale basis functions χ_i^{ms} minimize the energy $\int_{\omega_i} \kappa \nabla \chi_i^{ms} \cdot \nabla \chi_i^{ms}$ for a given boundary condition. The multiscale finite element basis function χ_i^{ms} is numerically computed through the following problem

$$-\mathrm{div}(\kappa \nabla \chi_i^{ms}) = 0 \ \text{ in } \omega_i, \quad \chi_i^{ms} = \chi_i^{lin} \ \text{ on } \partial\omega_i. \tag{II.16}$$

With such choice of the partition of unity functions, we expect that they can eliminate interior inclusions and high-anisotropy lines that do not touch boundaries of ω_i. We present an illustrative example below to show the advantage of the multiscale finite element partition of unity over the piecewise linear (or bilinear) partition of unity.

We consider a conductivity field

$$\kappa(x) = \begin{pmatrix} \cos(\theta) & -\sin(\theta) \\ \sin(\theta) & \cos(\theta) \end{pmatrix}^T \begin{pmatrix} 1 & 0 \\ 0 & \kappa_{22}(x) \end{pmatrix} \begin{pmatrix} \cos(\theta) & -\sin(\theta) \\ \sin(\theta) & \cos(\theta) \end{pmatrix}, \tag{II.17}$$

where κ_{22} is depicted in Figure II.1. The high-anisotropy lines are lines that form an angle of $-\theta$ with the horizontal axis.

We compute the number of small eigenvalues for the case of $\{\chi_i^{lin}\}$. Numerically, we verify that there are 12 small eigenvalues for the angles $\theta = 0$. In this case, the

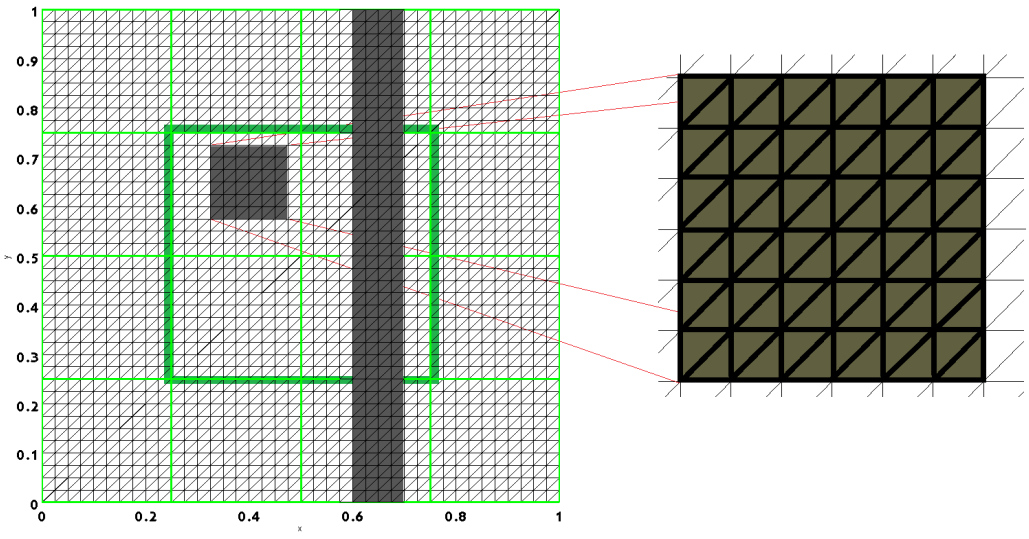

Figure II.1: Left: the fine mesh and function κ_{22} used in (II.17). The function η has value 1 in the background region and value 10^9 in the inclusions (gray). Right: the fine mesh inside the inclusion. See [25].

high-anisotropy lines are vertical lines. This is due to the fact that, since the mesh is structured inside the inclusion, we can then represent 12 independent functions that are constant in the vertical direction and vary along the horizontal direction only. Examining Table II.1, we make the following observations. For $\theta = \pi/2$, there are also 7 small eigenvalues, a fact that is justified in the same manner. For $\theta = -\pi/4$, there are 38 small eigenvalues, while for $\theta = \pi/3$ we observe only 4 small eigenvalues. For the mesh shown on Figure II.1, all these results can be easily explained using the fact that the fine-grid finite element functions are piece-wise linear in each triangle.

On the other hand, if we use $\{\chi_i^{ms}\}$, we see in Table II.1 that, for this example, we consistently get less small eigenvalues for all the angles θ.

θ	# of small eigenvalues for χ_i^{lin}	# of small eigenvalues for χ_i^{ms}
$-\pi/3$	4	2
$-\pi/4$	38	1
0	12	5
$\pi/4$	4	2
$\pi/3$	4	2
$\pi/2$	28	7

Table II.1: Comparison of the number of small eigenvalues corresponding to the use of χ_i^0 and χ_i^{ms}. Sub-domain: shown in Figure II.1 (left). $\kappa(x)$: defined in (II.17). See [25].

II.5 Numerical results

In this section, we show representative numerical results for the additive preconditioner (II.9) with the spectral multiscale space defined in (II.14). We consider the equation $-\text{div}(\kappa(x)\nabla u) = 1$ with the boundary condition $u = 0$ on $\partial\Omega$. We take $\Omega = [0,1] \times [0,1]$ and construct a coarse mesh $\mathcal{T}_H$ by dividing Ω into 10×10 equal squares ($H = 1/10$). The construction of the fine mesh $\mathcal{T}_h$ is obtained by dividing each coarse-grid cell into 10×10 identical squares ($h = 1/100$). Note that the dimension of the fine-grid finite element space is 10201.

We run the preconditioned conjugate gradient (PCG) until the l_2 norm of the residual is reduced by a factor of 10^{10}. We present the number of PCG iterations and the estimated condition number of the preconditioned system. In all examples, we consider values of the contrast η in the range $10^3 - 10^6$ and also give the dimension of the coarse spaces that were implemented.

We implement a two-level additive preconditioner with the following coarse spaces: (1) multiscale basis functions with linear boundary conditions (MS); (2) energy minimizing basis functions (EMF); (3) linear spectral coarse space with $\widetilde{\kappa}$ defined by (II.11) where the partition of unity functions are piecewise bilinear functions χ_i^{lin};

(4) multiscale spectral coarse space with $\widetilde{\kappa}$ defined by (II.11) where the partition of unity functions are the multiscale finite element basis functions χ_i^{ms}.

II.5.1 Examples of tensors with channels of high-anisotropy

We first use the coefficient tensor defined by (II.17) with $\theta = 0$. We consider several heterogeneous two-valued functions for κ_{22}. In this case, we have high-anisotropy along horizontal straight lines. The value of κ_{22} in the white background region is 1 and is η in the gray regions. We consider a number of cases, which differ by the position, the width , and the number of channels. The full description of all cases is given in Figure II.2. Note that the anisotropy in all cases is in the x_2-direction.

Horizontal channels. Two different widths of the channels are shown in Figure II.2, Cases 1 and 2. The results are presented in Tables II.2 and II.3. First, we remark that, the number of iterations in both cases does not change as the contrast increases when using the spectral coarse spaces (for both χ_i^{lin} and χ_i^{ms}). The two spectral coarse spaces seem to be robust with respect to the channel width. The multiscale coarse space (MS) and the energy minimizing coarse space (EMF) are not robust with respect to the channel width. Both, MS and EMF perform well for Case 2 (Table II.3) but not for Case 1 (Table II.2).

Regarding the dimension of the resulting coarse spaces, we see that, compared to the linear spectral coarse space (χ_i^{lin}), the dimension of the multiscale spectral coarse space (χ_i^{ms}) is lower. An important observation is that, as the channels get thinner and more numerous, the dimension of the linear spectral coarse space increases significantly, while the dimension of the multiscale spectral coarse space even decreases. This is due to the fact that, in Case 2, there is much less high-anisotropy lines (that is, vertical lines within high-anisotropy channels) that touch the edges of the coarse blocks. In our examples, the dimension of the matrix problem defining

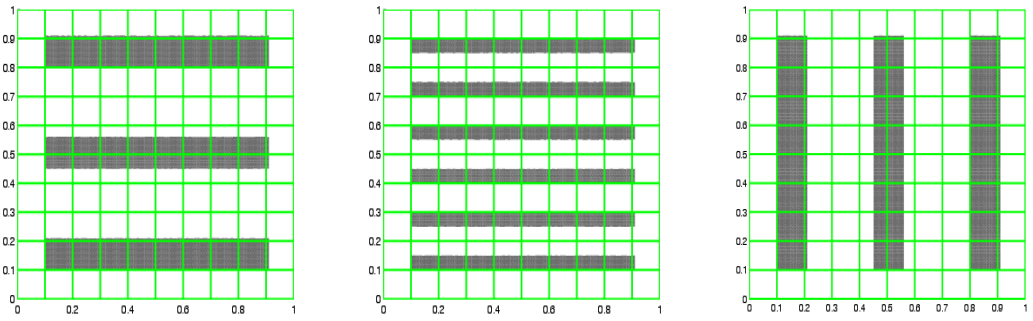

1.

2.

3.

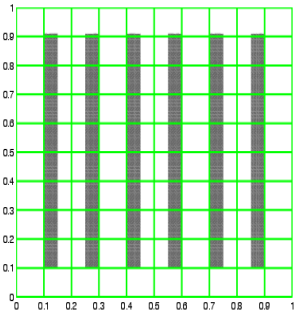

4.

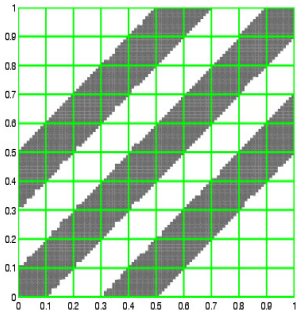

5.

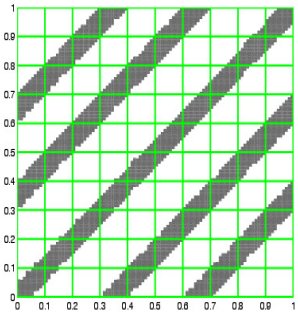

6.

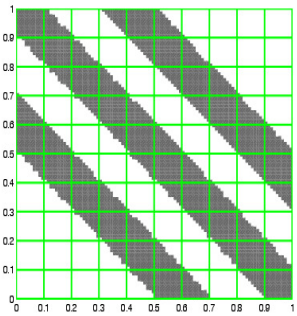

7.

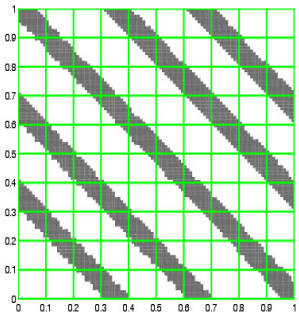

8.

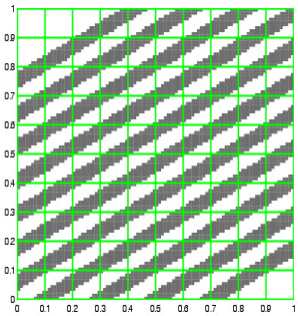

9.

Figure II.2: Coarse mesh and coefficients: $\kappa_{22}(x) = \eta >> 1$ in the gray region and $\kappa_{22}(x) = 1$ in the white background. From left to right and top to bottom (angle means the angle of inclination of the channel): **1.** Horizontal wide channels with width 1/10. **2.** Horizontal thin channels with width 1/25. **3.** Vertical wide channels with width 1/10. **4.** Vertical thin channels with width 1/25. **5.** Inclined wide channels with width $\sqrt{2}/10$ and angle $\pi/4$. **6.** Inclined thin channels with $\sqrt{2}/20$ and angle $\pi/4$. **7.** Inclined wide channels with width $\sqrt{2}/10$ and angle $3\pi/4$. **8.** Inclined thin channels with width $\sqrt{2}/10$ and angle $3\pi/4$. **9.** Inclined thin channels with width $\sqrt{2}/20$ and angle $3\pi/4$. See [25].

the local solvers is approximately 400 and, therefore, a coarse space of comparable size is preferred. We conclude that the multiscale spectral coarse space produces a robust coarse space of fairly appropriate size. The linear spectral coarse space is robust but it might be impractical since it could be much larger than the size of a local problem.

η	MS	EMF	Linear spectral	Multiscale spectral
10^3	151(2.8e+2)	56(2.6e+2)	45(18.0)	33(12.8)
10^4	344(2.7e+3)	320(2.5e+3)	36(12.0)	28(6.61)
10^5	562(2.7e+4)	531(2.6e+4)	41(13.5)	29(6.73)
10^6	818(2.7e+5)	743(2.6e+5)	28(5.42)	30(6.74)
Dim	81=0.79%	81=0.79%	1327=13.0%	776=7.6%

Table II.2: Number of iterations and estimated condition number for the PCG. Coefficient: shown in Figure II.2, Case 1. The dimension of the fine space: 10201. See [25].

η	MS	EMF	Linear spectral	Multiscale spectral
10^3	39(23.71)	33(13.37)	26(5.42)	26(5.84)
10^4	41(30.34)	33(13.38)	27(5.37)	25(5.39)
10^5	44(34.56)	33(13.38)	28(5.37)	25(5.39)
10^6	45(35.26)	33(13.38)	29(5.36)	25(5.39)
Dim	81=0.79%	81=0.79%	2298=22.5%	332=3.3%

Table II.3: Number of iterations and estimated condition number for the PCG. Coefficient: shown in Figure II.2, Case 2. The dimension of the fine space: 10201. See [25].

Vertical channels. Now, we consider the vertical channels with different widths. See Cases 3 and 4 in Figure II.2. The number of iterations and the dimension of the

local coarse spaces are displayed in Table II.4. The coarse spaces MS and EMF fail to produce robust preconditioners in this case while the two spectral spaces are shown to give preconditioners that are robust with respect to the contrast. We observe that, in these two cases, the linear spectral coarse space and the multiscale spectral coarse space bring the same result for the iterations and dimension. Furthermore, the width and the number of the channels do not affect the iterations and dimension.

η	MS	EMF	Linear spectral	Multiscale spectral
10^3	115(1.64e+2)	131(3.36e+2)	52(25.7)	39(15.)
10^4	241(1.51e+3)	271(3.23e+3)	27(5.36)	27(5.5)
10^5	335(1.50e+3)	369(3.21e+3)	27(5.38)	28(5.5)
10^6	442(1.50e+5)	472(3.21e+5)	80(2.5e+2)	28(5.5)
Dim	81=0.79%	81=0.79%	621=6.1%	621=6.1%

η	MS	EMF	Linear spectral	Multiscale spectral
10^3	97(1.13e+2)	106(1.63e+2)	61(32.3)	43(16.7)
10^4	192(8.86e+2)	196(8.03e+2)	34(11.8)	27(5.42)
10^5	230(8.75e+3)	297(7.97e+3)	28(5.37)	27(5.44)
10^6	277(8.74e+4)	392(7.97e+4)	29(5.39)	29(5.44)
Dim	81=0.79%	81=0.79%	558=5.5%	558=5.5%

Table II.4: Number of iterations and estimated condition number for the PCG. Coefficient: shown in Figure II.2. Case 3: top table and Case 4: bottom table. The dimension of the fine space: 10201. See [25].

Inclined channels. These examples include inclined channels with angles $\pi/4$ and $3\pi/4$ and different widths. See Cases 5, 6,7 and 8 in Figure II.2. The results are presented in Table II.5 for the angle of inclination $\pi/4$. Note that the number of iterations is still independent of the contrast for the two spectral coarse spaces. We observe that the multiscale spectral coarse space works very well in reduction of the dimension. Particularly, when there are more and thinner high-conductivity channels in the region, the dimension of the local coarse spaces has decreased. However, the

linear spectral coarse space has almost the same dimension which is three times larger than the local solver dimension.

η	MS	EMF	Linear spectral	Multiscale spectral
10^4	259(3.17e+3)	223(3.12e+3)	20(5.83)	23(7.38)
10^6	368(3.16e+5)	345(3.10e+5)	21(12.6)	24(13.0)
Dim	81=0.79%	81=0.79%	1415=13.9%	759=7.44%

η	MS	EMF	Linear spectral	Multiscale spectral
10^4	74(6.83e+2)	60(1.06e+2)	19(5.17)	21(7.80)
10^6	83(6.75e+4)	53(1.16e+2)	14(4.97)	15(7.82)
Dim	81=0.79%	81=0.79%	1437=14.1%	179=1.75%

Table II.5: Number of iterations and estimated condition number for the PCG. Coefficient: shown in Figure II.2. Case 5: top table and Case 6 : bottom table. The dimension of the fine space: 10201. See [25].

In Table II.6, we present the numerical results for an angle of inclination of the channels $3\pi/4$. Though the angle of the channels changes, the number of iterations does not change for the proposed coarse spaces. The results show that the dimensions of the two spectral coarse spaces are not affected by the change of angle. This is an important observation, since in a realistic situation there will be channels with various angles of inclination.

The next coefficient in the numerical experiment is Case 9 of Figure II.2. In this example, we consider a number of inclined channels with an angle $3\pi/4$. The number of PCG iterations and estimated condition numbers are displayed in Table II.7. We note that the numbers of iterations are all very small in this case when the region is full of high-productivity channels. We find that, as the number of the channels is large, the dimension of the linear spectral coarse space is huge, while the dimension of the multiscale spectral coarse space remains appropriate.

η	MS	EMF	Linear spectral	Multiscale spectral
10^4	311(3.5e+3)	330(3.4e+3)	31(13.)	30(13.0)
10^6	645(3.4e+5)	595(3.4e+5)	31(13.4)	30(13.4)
Dim	81=0.79%	81=0.79%	1407=14%	879=8.6%

η	MS	EMF	Linear spectral	Multiscale spectral
10^4	171(1.2e+3)	204(1.5e+3)	25(11.6)	22(7.28)
10^6	364(1.2e+5)	375(1.5e+5)	14(5.10)	18(7.27)
Dim	81=0.79%	81=0.79%	1427=14.1%	407=4.1%

Table II.6: Number of iterations and estimated condition number for the PCG. Coefficient: shown in Figure II.2. Case 7: top table and Case 8: bottom table. The dimension of the fine space: 10201. See [25].

η	MS	EMF	Linear spectral	Multiscale spectral
10^3	41(42.7)	32(14.6)	20(4.98)	24(7.74)
10^4	42(59.4)	30(14.6)	19(4.99)	21(7.78)
10^5	40(62.7)	28(14.6)	17(4.99)	18(7.77)
10^6	39(63.1)	27(14.6)	16(4.99)	15(7.73)
Dim	81≈0.8%	81≈0.8%	3577≈35%	459≈4.5%

Table II.7: Number of iterations and estimated condition number for the PCG. Coefficient: shown in Figure II.2, Case 9. The dimension of the fine space: 10201. See [25].

II.5.2 Varying directions of high-anisotropy

Next, we test the coefficient which is of the form

$$\kappa(x) = \begin{pmatrix} \kappa_{11}(x) & 0 \\ 0 & \kappa_{22}(x) \end{pmatrix}.$$

The coefficients are depicted in Figure II.3. Unlike the cases mentioned above, the coefficient considered here has distinct anisotropy directions in different channels of high-anisotropy. We consider several heterogeneous two-valued functions for κ_{11} and

κ_{22}. The values of κ_{11} and κ_{22} in the white background region are 1 and high within the gray channels. The results for this case are displayed in Table II.8. As before, the number of iterations does not change as the value of the contrast increases. Furthermore, compared to the linear spectral coarse space, the multiscale spectral coarse space performs much better in reducing the dimension of the coarse spaces.

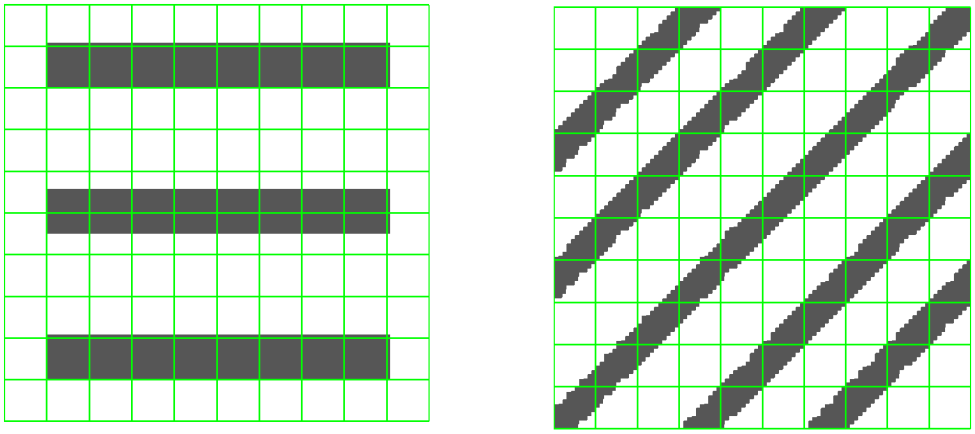

Figure II.3: Coefficient κ and the coarse mesh. Left: $\kappa_{11}(x) = \eta >> 1$ in the gray region and $\kappa_{11}(x) = 1$ in the white background (the width of each channel is 1/10). Right: $\kappa_{22}(x) = \eta >> 1$ in the gray region and $\kappa_{22}(x) = 1$ in the white background (the width of each channel is $\sqrt{2}/20$ and the angle is $\pi/4$). See [25].

η	MS	EMF	Linear spectral	Multiscale spectral
10^4	284(5.2e+3)	265(5.8e+3)	22(8.63)	22(8.62)
10^6	546(5.2e+5)	554(5.8e+5)	17(6.95)	19(8.85)
Dim	81≈0.8%	81≈0.8%	1377≈13%	387≈3.8%

Table II.8: Number of iterations and estimated condition number for the PCG. Coefficient: shown in Figure II.3. We set the tolerance to be 10^{-10}. $H = 1/10$, $h = 1/100$. The dimension of the fine space: 10201. See [25].

II.6 Analysis of the preconditioner

We follow the analysis in [27, 39]. We assume that the elements of $\mathcal{T}_h$ contained in Ω form a triangulation of Ω. Further, we use the notations introduced in section II.4. Namely, $\{\chi_i\}_{i=1}^{N_v}$ is the partition of unity defined by (II.16), $\Psi_{i,l}(x)$ are the local spectral basis functions defined in (II.13), and V_0 is the *local spectral multiscale* space defined in (II.14).

Now, we define the coarse interpolation operator $I_0 : V^h(\Omega) \to V_0$ by

$$I_0 v = \sum_{i=1}^{N_v} \sum_{\ell=1}^{L_i} \left(\int_{\omega_i} \widetilde{\kappa} v \psi_\ell^{\omega_i} dx \right) I^h(\chi_i \psi_\ell^{\omega_i}), \tag{II.18}$$

where I^h is the fine-scale nodal value interpolation operator.

For each coarse block K, define the union of the elements that share common edge with K, $\omega_K = \bigcup\{\omega_j;\ x_j \in \overline{K},\}$ and note that the weighted L^2-approximation and weighted H^1-stability properties hold (cf. e.g., [23, 39]):

Lemma II.6.1. *For all coarse element K, we have*

$$\int_K \widetilde{\kappa}(v - I_0 v)^2 dx \leq C \lambda_{K,L+1}^{-1} \int_{\omega_K} \kappa \nabla v \cdot \nabla v dx$$

and

$$\int_K \kappa \nabla I_0 v \cdot \nabla I_0 v dx \leq C \max\{1, \lambda_{K,L+1}^{-1}\} \int_{\omega_K} \kappa \nabla v \cdot \nabla v dx,$$

where $\lambda_{K,L+1} = \min_{x_i \in K} \lambda_{L_i+1}^{\omega_i}$ and the constant C does not depend on the contrast.

Using Lemma II.6.1, we can estimate the condition number of the preconditioned operator $B^{-1}A$ with B^{-1} defined in (II.9) using the coarse-space V_0 introduced in (II.14). Following [23, 27, 39], one has the following main result:

Lemma II.6.2. *The condition number of the preconditioned operator $B^{-1}A$ with B^{-1} defined in (II.9) satisfies the bound*

$$cond(B^{-1}A) \leq C(1 + \lambda_{L+1}^{-1}), \quad where \quad \lambda_{L+1} = \min_{1 \leq i \leq N_v} \lambda_{L_i+1}^{\omega_i},$$

with a constant C independent of the contrast η.

It can be easily shown that the eigenvalues of the local problem scale as $O(1)$ assuming $\xi_i = \chi_i$, $i = 1, \ldots, N = N_v$, in (II.11). The dependency of the condition number on δ and H is controlled by the partition of unity $\{\chi_i\}_{i=1}^{N_v}$. The condition number is independent of h and it is, in general, of order $O(H^2/\delta^2)$, see [39].

II.7 Concluding remarks

In this chapter, we have discussed robust two-level domain decomposition preconditioners for highly anisotropic heterogeneous multiscale problems. The existence of high-anisotropy within the material causes a high dimension of the coarse space, and burden the computation consequently. Particularly, we observe that the number of basis functions will increase within high-anisotropic sub-domains. To reduce the dimension, we design localized eigenvalue problems to form the reduced-dimensional spectral coarse space. Standard bilinear basis functions and multiscale basis functions are employed as the partition of unity. The numerical experiments confirm that the two spectral coarse spaces work well in reduction of the dimension and provide robust preconditioners in the sense that the width, angle, and number of anisotropic channels do not affect the number of iterations. Furthermore, the spectral coarse space using multiscale basis functions offers a more robust preconditioner with respect to the underlying physical parameters.

III A GENERALIZED MULTISCALE FINITE ELEMENT METHOD FOR HIGH-CONTRAST SINGLE-PHASE FLOW PROBLEMS IN ANISOTROPIC MEDIA[1]

III.1 Introduction

In this chapter, a more general parameter-dependent anisotropic flow problem is investigated in the framework of the Generalized Multiscale Finite Element Method (GMsFEM) [50]. Our objective is to extend the results of Chapter II and (1) consider parameter-dependent problems, where the parameter represents possible uncertainties, and (2) put the multiscale finite element into a more general framework, which allows using various snapshot spaces (e.g., harmonic snapshot spaces). Both of these extensions are important in extending the application range of anisotropic problems and the efficiency and accuracy of multiscale computations. The input variable used in GMsFEM can be characterized by: (1) uncertainties contained in the coefficients of the problem; (2) many source terms; (3) changing boundary conditions. The proposed approach treats these input parameters together and coarse spaces are constructed independent of the input space. This allows performing fast computations in the online stage as discussed below.

The GMsFEM [24] is a flexible framework that extends the Multiscale Finite Element Method (MsFEM) by systematically enriching the coarse solution spaces by taking into account small scale information and complex input spaces. Same as the other reduced-order methods, the objective of the GMsFEM is to construct a small dimensional coarse space from which the multiscale solution can be efficiently

[1]Part of the data reported in this chapter is reprinted with permission from "A generalized multiscale finite element method for high-contrast single-phase flow problems in anisotropic media" by J. Ren and M. Presho. Journal of Computational and Applied Mathematics, 277:202–214, 2015, Copyright[2015] by Elsevier.

and accurately approximated. This approach follows an offline-online procedure illustrated below.

1. Offline computation:
   - 1.0. Coarse grid generation;
   - 1.1. Construction of snapshot space that will be used to compute an offline space.
   - 1.2. Construction of a small dimensional offline space by performing dimension reduction in the space of local snapshots.
2. Online computations:
   - 2.1. For each input parameter, compute multiscale basis functions;
   - 2.2. Solution of a coarse-grid problem for any force term and boundary condition;
   - 2.3. Iterative solvers, if needed.

At the offline stage, we first construct a larger dimensional snapshot space upon a coarse grid. The snapshot space consists of local solution functions (via local problems) that can represent the solution space. In particular, the local problem is solved with all possible boundary conditions (and with various choices of input parameters) in Step 1.1. Next, a smaller dimensional offline space, as a subspace of the snapshot space, is constructed via a spectral decompositions in Step 1.2. Typically, the spectral decomposition is based on a local eigenvalue problem. Via the local eigenvalue problem, the offline space is then formed by the selected dominant modes. We emphasize here that oversampling techniques can be used in local computations to achieve more stringent error bounds [29].

For parameter-dependent problems, an online computation is needed. In Step 2.1, we construct online solution spaces that correspond to some specified values of the input parameter. To obtain a small dimensional subspace of the offline space, a spectral decomposition will be performed in the offline space. The identified dominant modes then generate the required online space. Finally, the resulting multiscale basis functions are coupled via a respective global formulation to compute the solution.

The goal of this chapter is to investigate the application of the GMsFEM to high-contrast flow problems with strong anisotropy. We consider a second order elliptic problem, where the coefficient exhibits parameter-dependence which models the physical characteristics of the porous medium. The strong anisotropy is aligned with one coordinate axis that is described by an extremely small parameter. Additionally, we incorporate a continuous Galerkin (CG) coupling mechanism to solve the global problem, and use an oversampling procedure in order to construct the localized basis functions. The proposed method is shown to yield decreasing errors that correspond to the selection of more dominant eigenfunctions in the coarse solution space. In other words, larger coarse spaces expectedly offer more accurate approximations. We validate the performance of the method through considering a variety of cases and numerical examples.

The rest of this chapter is organized as follows. In Section III.2, we formulate the model problem, introduce the notation to be used throughout this chapter. Section III.3 is devoted to the detailed construction of the coarse space. In particular, the construction of the snapshot space, offline space, and online space will be presented in subsections III.3.1, III.3.2, and III.3.3, respectively. A variety of numerical experiments are offered in Section III.4. We finish this chapter by offering some concluding remarks in Section III.5.

III.2 Problem formulation

In this study, we consider a second-order elliptic problem in a convex polygonal domain $\Omega \subset \mathbb{R}^n$, where $n = 2$ or 3:

$$\begin{aligned} -\text{div}(\kappa(x;\mu)\nabla u) &= f \quad \text{in} \quad \Omega, \\ u(x) &= 0 \quad \text{on} \quad \partial\Omega. \end{aligned} \tag{III.1}$$

Here, the coefficient $\kappa(x;\mu)$ represents the conductivity field of a highly heterogenous porous medium with high-anisotropy. In the two dimensional case that we study in this chapter, it is assumed that $\kappa(x;\mu)$ takes the form

$$\kappa(x;\mu) = (1-\mu)\kappa_1(x)+\mu\kappa_2(x) = (1-\mu)\begin{pmatrix} \kappa_1^1(x) & 0 \\ 0 & \frac{1}{\epsilon_1}\kappa_1^2(x) \end{pmatrix}+\mu\begin{pmatrix} \kappa_2^1(x) & 0 \\ 0 & \frac{1}{\epsilon_2}\kappa_2^2(x) \end{pmatrix},$$

where μ is taken to be a value in some parameter space. The terms κ_1^1, κ_1^2, κ_2^1 and κ_2^2 are of the same order of magnitude, whereas the parameters $0 < \epsilon_1, \epsilon_2 \leqslant 1$ can be very small, provoking the high anisotropy of the problem (see Figure III.1 for an illustration of $\kappa_1(x)$ and $\kappa_2(x)$) . While the anisotropic direction presented in this chapter is fixed and aligned with the $y-$axis, more general anisotropies can be applied to our method. For instance, the direction of the high-conductivity can vary in different regions.

In introducing the discrete form of the problem, we first comment on the notion of the coarse and fine mesh. Though there is some overlap with the notations of coarse grids introduced earlier in Chapter II, for convenience, we briefly introduce the coarse and fine grid notations as some extra coarse grid information will be used in this chapter. The domain Ω is assumed to be discretized by a coarse-grid partition

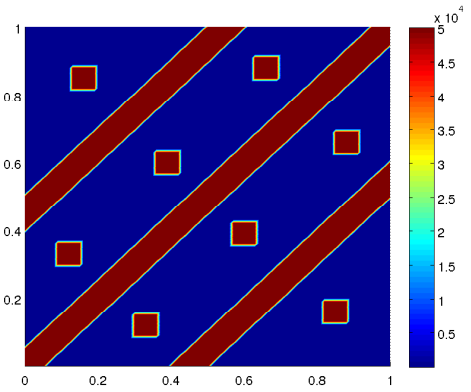

(a) y-directional component of $\kappa(x)$

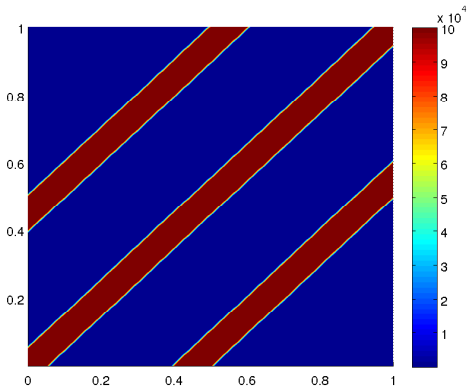

(b) y-directional component of $\kappa_1(x)$

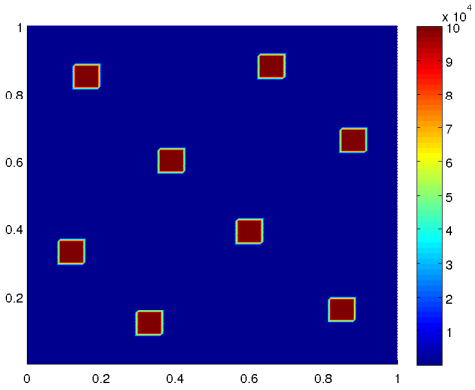

(c) y-directional component of $\kappa_2(x)$

Figure III.1: Illustration of y-directional anisotropic conductivities. See [50].

denoted by $\mathcal{T}^H$ of mesh size H. The conforming triangulation can be generated by triangles, quadrilaterals, tetrahedrals, etc. The fine mesh is obtained by splitting each sub-domain in T^H into a connected union of fine-grid blocks, and we denote it by $\mathcal{T}_h$ of mesh size h. Given a coarse discretization $\mathcal{T}^H$, we denote by $\{x_i\}_{i=1}^{N_v}$ (where N_v is the number of coarse nodes) the vertices of $\mathcal{T}^H$, and define the neighborhood ω_i of the node x_i by (II.7). Furthermore, we introduce a notation for an oversampled region denoted by ω_i^+. Generally, we choose ω_i^+ by adding a single or multiple layers

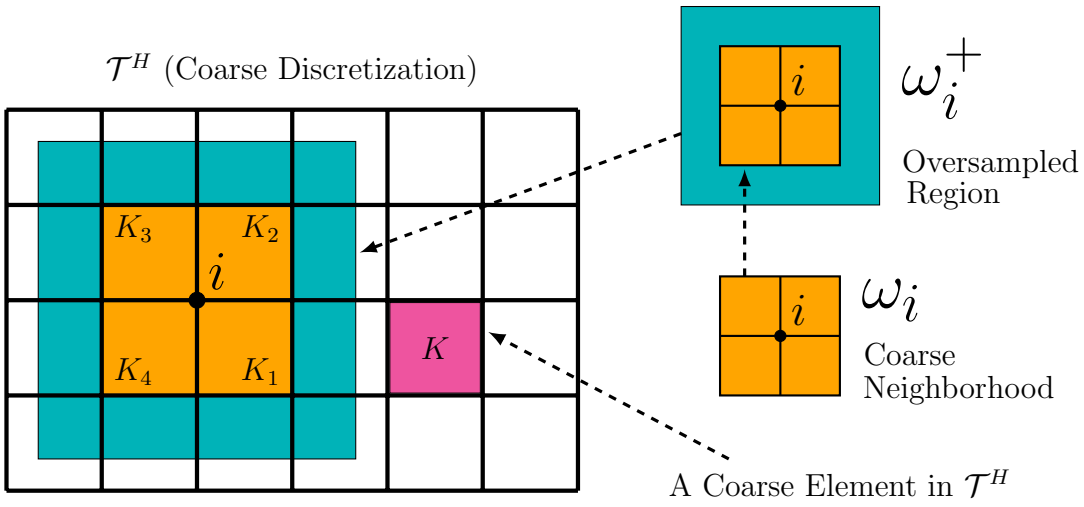

Figure III.2: Illustration of a coarse neighborhood and oversampled region. See [50].

of fine-grid blocks around ω_i. That is,

$$\omega_i^+ = \omega_i \cup \{n_i \text{ layer(s) of fine-grid blocks around } \omega_i,\ n_i \geqslant 1\}. \tag{III.2}$$

See Figure III.2 for an illustration of a neighborhood, oversampled region, and elements subordinated to the coarse discretization.

Next, we briefly outline the formation of coarse basis space. Throughout the chapter, we consider continuous Galerkin formulations only. We denote the online coarse basis space by V_{on}^+ which consists of $\{\psi_{i,k}^{+,\text{on}} : \ 1 \leq i \leq N_v,\ 1 \leq k \leq L_{i,\text{on}}\}$, where $L_{i,\text{on}}$ denotes the number of dominant eigenfunctions that are included on each coarse neighborhood. For each coarse node x_i, $\{\psi_{i,k}^{+,\text{on}} : \ 1 \leq k \leq L_{i,\text{on}}\}$ are computed by performing a spectral decomposition in the offline space V_{off}^+ via an eigenvalue problem on ω_i^+ or ω_i. We again note that an oversampling technique is used in local problems. The details of the offline-online localized spectral construction will be offered in the next section. Once the coarse space is formed, the discrete problem

reads as follows. We seek $u_H \in V_{\text{on}}^+$ such that

$$a(u_H, v; \mu) = (f, v), \quad \text{for all } v \in V_{\text{on}}^+, \tag{III.3}$$

where $a(u, v; \mu) = \int_\Omega \kappa(x; \mu) \nabla u \cdot \nabla v$ and $(f, v) = \int_\Omega fv$. For the notational convenience, we will denote the continuous variables and the corresponding discrete quantities with the same symbols.

III.3 Construction of the multiscale coarse space

In this section, we will discuss the construction of the multiscale solution space. We will first introduce the snapshot space, which contains an extensive set of basis functions formed by solutions of local problems with all possible boundary conditions. Then, we will present a space reduction technique which enables us to identify the dominant modes in the snapshot space. At the end, an online space is constructed for problems with parameter dependency.

III.3.1 Snapshot space

In the offline computation, we first construct a snapshot space V_{snap}^+ or $V_{\text{snap}}^{\omega_i}$, depending on the choice of domain for generating the space, where ω_i^+ is an oversampled region that contains the neighborhood ω_i. We note that in the case when ω_i is adjacent to the global boundary, no oversampled domain is used. For notational brevity, we will only use the superscript + for either choice of computation domain. For example, + may also be referred to a "non-oversampled" domain. Because the snapshot space consists of spatial fields defined on local fine grids, they are vectors of the dimension of the fine-grid resolution of a local coarse region. In general, the standard fine-scale finite element space defined on ω_i^+ will be used in the computation of snapshots.

One of benefits of constructing the localized snapshot space is that it can keep the local solution space independent of the global source term or boundary condition. In the case of a large parameter space, it can avoid the extremely expensive re-computation when the source term or boundary condition is changed. Another benefit is the elimination of unwanted degrees of freedom (Dof) in the parameter space. We note that there exist Dofs which may not contribute to the global solution, and as a result, such snapshots should not be considered in the offline space. Instead, we specify the parameter μ as a set of fixed values $\{\mu_j, 1 \leqslant j \leqslant J\}$, where J denotes the number of parameter values we choose in the snapshot generation. Each μ_j will be input to generate a single snapshot. We present two choices for generating the snapshot space, though other options may be also applicable.

First choice: harmonic snapshot. We consider snapshot space consisting of harmonic extension of fine-grid functions defined on $\partial\omega_i^+$. We solve

$$-\mathrm{div}(\kappa(x;\mu_j)\nabla\psi_{l,j}^{+,\mathrm{snap}}) = 0 \ \text{ in } \omega_i^+, \quad \psi_{l,j}^{+,\mathrm{snap}} = \delta_{l,m} \text{ on } \ \partial\omega_i^+,$$

where $\{\mu_j : 1 \leqslant j \leqslant J\}$ is a pre-specified set of parameter values, l, $m \in J(\partial\omega_i^+)$ (nodes on $\partial\omega_i^+$). The snapshot space corresponding to the oversampled region ω_i^+ can be written as

$$V_{\mathrm{snap}}^+ = \mathrm{span}\{\psi_{l,j}^{+,\mathrm{snap}} : 1 \leqslant j \leqslant J, \ \ l \in J(\partial\omega_i^+)\}.$$

Second choice: eigenvalue snapshot. We propose to solve the following zero Neu-

mann boundary value problem

$$-\text{div}(\kappa(x;\mu_j)\nabla\psi_{l,j}^{+,\text{snap}}) = \lambda_{l,j}^{+,\text{snap}}\tilde{\kappa}(x;\mu_j)\psi_{l,j}^{+,\text{snap}} \qquad \text{in } \omega_i^+. \tag{III.4}$$

Here, $\tilde{\kappa}$ is a scalar weight associated with the coefficient matrix $\kappa(x;\mu)$ and contains the relevant behavior of the solutions that needs to be represented by coarse basis functions $\{\chi_i^+\}$. In this chapter we define $\tilde{\kappa} = H^2\sum_i \kappa\nabla\chi_i^+ \cdot \nabla\chi_i^+$, where χ_i^+ is the standard multiscale basis function to be later defined in problem (III.17). Note that the eigenvalue problem (III.4) is an extension of the spectral problem (II.10) in Chapter II to a parameter-dependent case. Discretization of (III.4) yields a generalized eigenvalue problem of the form

$$A^{+,\text{snap}}(\mu_j)\psi = \lambda M^{+,\text{snap}}(\mu_j)\psi, \quad \text{in } \omega_i^+, \tag{III.5}$$

where we define the local matrix $A^{+,\text{snap}}(\mu_j)$ and the mass matrix $M^{+,\text{snap}}(\mu_j)$ by

$$A_{m,n}^{+,\text{snap}}(\mu_j) = \int_{\omega_i^+} \kappa(x;\mu_j)\nabla\phi_m \cdot \nabla\phi_n \quad \text{and} \quad M_{m,n}^{+,\text{snap}}(\mu_j) = \int_{\omega_i^+} \tilde{\kappa}(x;\mu_j)\phi_m\phi_n, \tag{III.6}$$

and ϕ_n are standard fine-scale basis functions.

We denote the eigenvalues and eigenvectors of (III.6) by $\{\lambda_{l,j}^{+,\text{snap}}\}$ and $\{\psi_{l,j}^{+,\text{snap}}\}$, respectively, and order the first L_i eigenvalues as

$$0 \leqslant \lambda_{1,j}^{+,\text{snap}} \leqslant \lambda_{2,j}^{+,\text{snap}} \leqslant \cdots \leqslant \lambda_{L_i,j}^{+,\text{snap}}.$$

Then, the L_i eigenvectors corresponding to the first L_i smallest eigenvalues generate

a local snapshot space. That is,

$$V_{\text{snap}}^{+} = \text{span}\{\psi_{l,j}^{+,\text{snap}} : 1 \leqslant j \leqslant J, \quad 1 \leqslant l \leqslant L_i\}. \tag{III.7}$$

We re-numerate the snapshot functions by a single index to create the snapshot matrix

$$R_{\text{snap}}^{+} = \left[\psi_1^{+,\text{snap}}, \cdots, \psi_{L_{\text{snap}}}^{+,\text{snap}}\right] \quad \text{and} \quad R_{\text{snap}} = \left[\psi_1^{\text{snap}}, \cdots, \psi_{L_{\text{snap}}}^{\text{snap}}\right],$$

where $\psi_k^{\text{snap}} = I^{\omega_i}(\psi_k^{+,\text{snap}})$ is the restriction of $\psi_k^{+,\text{snap}}$ to ω_i, and the dimension of the local snapshot space is $L_{\text{snap}} = J * L_i$.

Remark III.3.1. *The eigenvalues of (III.5) vanish asymptotically which can enable us to select the high-energy modes by picking small eigenvalues (see [33, 39]). Intuitively speaking, the dominant eigenvectors corresponding to the small eigenvalues own high energy at the place where the high conductivity occurs. Thus, there is a close relation between high-energy modes and the structure of the spatial fields. In [39], it was shown that the number of small eigenvalues depends on the number of inclusions and channels within the local region, and the choice of the partition of unity $\{\chi_i^+\}$ in computing $\tilde{\kappa}$. Recall that in Chapter II, multiscale basis functions are employed to be the partition of unity, which offers an efficient reduction in the dimension of the multiscale coarse space. Here, in the framework GMsFEM (with snapshot spaces, oversampling techniques), the localized eigenvalue problems still show great performance in reducing the dimension of the coarse space.*

Remark III.3.2. *We note that the space of snapshots involves solving local problems for a set of parameter values $\{\mu_j\}$. For each single snapshot set $V_{snap}^{+}(\mu_j)$, the eigenvectors are independent and orthogonal with respect to the mass matrix $M^{+}(\mu_j)$.*

The snapshot space V_{snap}^{+} corresponding to the coarse node i is the combination of all the single snapshots, i.e. $V_{snap}^{+} = \cup_j V_{snap}^{+}(\mu_j)$. In order to guarantee that the snapshot matrix R_{snap}^{+} is healthy for the offline space construction, it is desirable to remove the dependency in V_{snap}^{+}. Furthermore, even if R_{snap}^{+} does not have dependent elements, the truncated matrix R_{snap} can still do. This occurs when the independent components are only within the area $\omega_i^{+} \backslash \omega_i$. In the parameter independent case, there is no such issue. Without loss of generality, in this chapter both matrices R_{snap}^{+} and R_{snap} are assumed to be linearly independent.

III.3.2 Offline space

The main goal at the offline stage is to construct a small dimensional space V_{off}^{+} in the space of snapshots using a dimension reduction technique. To perform a dimension reduction, typically we use an auxiliary spectral decomposition of the space V_{snap}^{+}. More precisely, we are trying to seek a possibly small dimensional subspace $V_{\text{off}}^{+} \subset V_{\text{snap}}^{+}$ such that for any $\psi \in V_{\text{snap}}^{+}(\mu^*)$ (μ^* is chosen in the parameter space), it can be approximated in V_{off}^{+} in an appropriate sense.

Due to the fact that the space of snapshots involves solving local problems for various choices of the input parameters and source terms, the offline space as a subspace can be re-used to generate the multiscale basis functions for any input parameter at the online stage without repeated computation. Thus, the offline (pre-computation) stage saves us a considerable computation time at the online stage. Also we note that at the offline stage, eigenvalue problems is parameter free. Thus, generally the weighted averages $\overline{\kappa}$ and $\widetilde{\overline{\kappa}}$ will be used in the bilinear forms.

Below we provide several plausible eigenvalue problems in the space of snapshots:

$$A^{\text{off}}\Psi_k^{\text{off}} = \lambda_k^{\text{off}} M^{\text{off}}\Psi_k^{\text{off}} \tag{III.8}$$

$$A^{+,\text{off}}\Psi_k^{\text{off}} = \lambda_k^{\text{off}} M^{\text{off}}\Psi_k^{\text{off}} \tag{III.9}$$

$$A^{\text{off}}\Psi_k^{\text{off}} = \lambda_k^{\text{off}} M^{+,\text{off}}\Psi_k^{\text{off}} \tag{III.10}$$

$$A^{+,\text{off}}\Psi_k^{\text{off}} = \lambda_k^{\text{off}} M^{+,\text{off}}\Psi_k^{\text{off}} \tag{III.11}$$

where

$$A^{\text{off}} = \left[a_{mn}^{\text{off}}\right] = \int_{\omega_i} \overline{\kappa}(x;\mu)\nabla\psi_n^{\text{snap}} \cdot \nabla\psi_m^{\text{snap}} = R_{\text{snap}}^T \overline{A} R_{\text{snap}},$$

$$M^{\text{off}} = \left[m_{mn}^{\text{off}}\right] = \int_{\omega_i} \tilde{\overline{\kappa}}(x;\mu)\psi_n^{\text{snap}} \cdot \psi_m^{\text{snap}} = R_{\text{snap}}^T \overline{M} R_{\text{snap}},$$

$$A^{+,\text{off}} = \left[a_{mn}^{+,\text{off}}\right] = \int_{\omega_i^+} \overline{\kappa}(x;\mu)\nabla\psi_n^{+,\text{snap}} \cdot \nabla\psi_m^{+,\text{snap}} = (R_{\text{snap}}^+)^T \overline{A}^+ R_{\text{snap}}^+,$$

$$M^{+,\text{off}} = \left[m_{mn}^{+,\text{off}}\right] = \int_{\omega_i^+} \tilde{\overline{\kappa}}(x;\mu)\psi_n^{+,\text{snap}} \cdot \psi_m^{+,\text{snap}} = (R_{\text{snap}}^+)^T \overline{M}^+ R_{\text{snap}}^+.$$

We refer the interested reader to [6] for more convergence estimates associated with the above eigenvalue problems. We emphasize that the analysis and examples in [6] were built to treat isotropic problems, whereas the main goal of the present work is to offer a generalized framework which extends to highly anisotropic problems. Here, A^+ and A as defined in III.6 denote the fine-scale stiffness matrix on ω_i^+ and ω_i respectively, $\overline{A}^+$ and $\overline{A}$ are their corresponding matrices which used averaged coefficients in the construction. We note that the construction of the offline space is carried out independently on coarse cells which suggests that parallel computation can be utilized. Each eigenvalue problem above will individually produce a set of eigenvectors for generating the offline space V_{off}^+ by: 1. selecting L_{off} eigenvectors

corresponding to the smallest L_{off} eigenvalues from one of the eigenvalue problems (III.8-III.11); 2. computing the element $\psi_k^{+,\text{off}} = \sum_{j=1}^{L_{\text{snap}}} \Psi_{kj}^{\text{off}} \psi_j^{+,\text{snap}}$ for $k = 1, \cdots, L_{\text{off}}$, where Ψ_{kj}^{off} is the jth component of Ψ_k^{off}. Then the offline space in the oversampled region ω_i^+ is formed as

$$V_{\text{off}}^+ = \text{span}\{\psi_k^{+,\text{off}} : 1 \leqslant k \leqslant L_{\text{off}}\}. \tag{III.12}$$

We create the offline matrices by setting

$$R_{\text{off}}^+ = \left[\psi_1^{+,\text{off}}, \cdots, \psi_{L_{\text{off}}}^{+,\text{off}}\right] \quad \text{and} \quad R_{\text{off}} = \left[\psi_1^{\text{off}}, \cdots, \psi_{L_{\text{off}}}^{\text{off}}\right],$$

where $\psi_k^{\text{off}} = I^{\omega_i}(\psi_k^{+,\text{off}})$ is a natural projection of $\psi_k^{+,\text{off}}$ on ω_i.

Remark III.3.3. *For the parameter-independent case, there is inherently no need to average the stiffness matrix and the mass matrix in the offline stage. Also, the offline space is identical to the online space where we seek the global multiscale solution. Therefore, the online stage is limited to the parameter-dependent case only.*

Remark III.3.4. *In general, $L_{off} \leqslant L_{snap}$. In other words, the offline space is a subspace of the snapshot space which can suitably incorporate the multiscale information. As for a high-contrast anisotropic problem, our main concern is the field with high-energy. It is ideal that the coarse basis space can recover pertinent information to accurately approximate the fine-mesh solution. At the same time, a reduced-dimension approximation space is also desirable for efficient computation. The balance between accuracy and efficiency would definitely allow us to increase the simulation efficiency with a desired level of accuracy. As such, the dimension technique used in the offline stage can greatly benefit us in various multiscale problems.*

Remark III.3.5. *The convergence of GMsFEM is proportional to the maximum of*

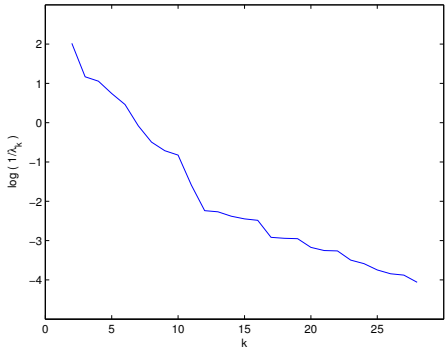

(a) Eigenvalue problem III.8 using harmonic snapshots

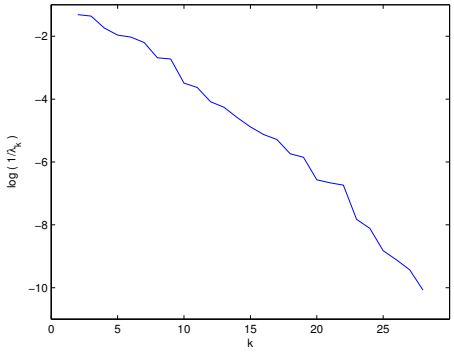

(b) Eigenvalues problem III.9 using harmonic snapshots

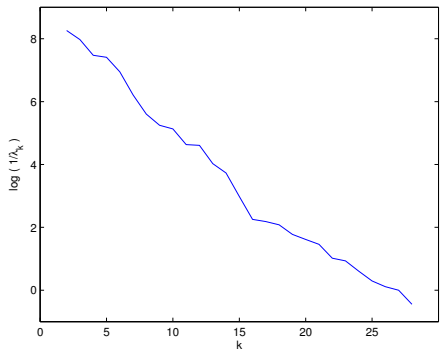

(c) Eigenvalues problem III.10 using harmonic snapshots

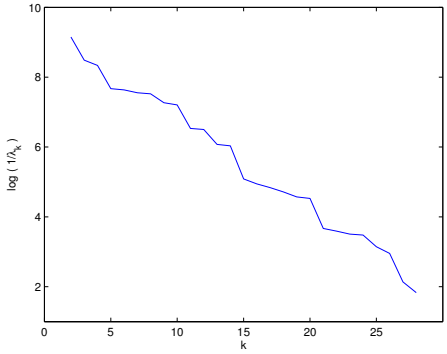

(d) Eigenvalues problem III.10 using spectral snapshots

Figure III.3: Eigenvalues decay on log-scale against the number of eigenvalues. $\mu = 0$. Coefficient $\kappa(x;\mu) = \kappa_1(x) = \text{diag}(1, \frac{1}{\epsilon_1})$ with $\epsilon_1 = 10^{-5}$ in red region, $\epsilon_1 = 1$ in the blue region, see Figure III.1 (b). Computation domain $\omega_i^+ = [0.4, 0.8] \times [0.4, 0.8]$ or $\omega_i = [0.5, 0.7] \times [0.5, 0.7]$. See [50].

the reciprocal of the eigenvalue whose corresponding eigenvector is ***not*** *included in the coarse space [33]. We test several choices of the bilinear forms for the eigenvalue problems* (III.8)-(III.11)*, and depict some respresentative results in Figure III.3. As we observe from the figure, the decay of eigenvalues is much faster when the eigenvalue problem is solved on oversampled domains.*

III.3.3 Online space

Our goal at the online stage is to construct a small dimensional subspace of the offline space that will yield suitable multiscale basis functions. The procedure of constructing online space is very similar to the one for offline space. A focal difference is that $\kappa(x;\mu)$ and $\tilde{\kappa}(x;\mu)$ are now taken to be parameter-dependent. In other words, the reduced dimension online space will be computed for each parameter value within the fixed offline space. In particular, for each oversampled region ω_i^+ and for each input parameter value μ^*, we seek a subspace $V_{\text{on}}^+(\mu^*)$ of V_{off}^+ via spectral decomposition. Below are a variety of eigenvalue problems that may be used at the online stage:

$$A^{\text{on}}(\mu^*)\Psi_k^{\text{on}} = \lambda_k^{\text{on}} M^{\text{on}}(\mu^*)\Psi_k^{\text{on}} \tag{III.13}$$

$$A^{+,\text{on}}(\mu^*)\Psi_k^{\text{on}} = \lambda_k^{\text{on}} M^{\text{on}}(\mu^*)\Psi_k^{\text{on}} \tag{III.14}$$

$$A^{\text{on}}(\mu^*)\Psi_k^{\text{on}} = \lambda_k^{\text{on}} M^{+,\text{on}}(\mu^*)\Psi_k^{\text{on}} \tag{III.15}$$

where

$$A^{\text{on}}(\mu^*) = [a_{mn}^{\text{on}}(\mu^*)] = \int_{\omega_i} \kappa(x;\mu^*)\nabla\psi_n^{\text{off}} \cdot \nabla\psi_m^{\text{off}} = R_{\text{off}}^T A(\mu^*) R_{\text{off}},$$

$$M^{\text{on}}(\mu^*) = [m_{mn}^{\text{on}}(\mu^*)] = \int_{\omega_i} \tilde{\kappa}(x;\mu^*)\psi_n^{\text{off}} \cdot \psi_m^{\text{off}} = R_{\text{off}}^T M(\mu^*) R_{\text{off}},$$

$$A^{+,\text{on}}(\mu^*) = \left[a_{mn}^{+,\text{on}}(\mu^*)\right] = \int_{\omega_i^+} \kappa(x;\mu^*)\nabla\psi_n^{+,\text{off}} \cdot \nabla\psi_m^{+,\text{off}} = (R_{\text{off}}^+)^T A^+(\mu^*) R_{\text{off}}^+,$$

$$M^{+,\text{on}}(\mu^*) = \left[m_{mn}^{+,\text{on}}(\mu^*)\right] = \int_{\omega_i^+} \tilde{\kappa}(x;\mu^*)\psi_n^{+,\text{off}} \cdot \psi_m^{+,\text{off}} = (R_{\text{off}}^+)^T M^+(\mu^*) R_{\text{off}}^+.$$

Each eigenvalue problem of (III.13-III.15) will individually produce a family of eigenvectors for generating the online space $V_{\text{on}}^{+}(\mu^*)$ by: 1. selecting L_{on} ($\leqslant L_{\text{off}}$) eigenvectors corresponding to the smallest L_{on} eigenvalues from one of the eigenvalue problems (III.13-III.15); 2. computing the projection $\psi_k^{+,\text{on}} = \sum_{j=1}^{L_{\text{off}}} \Psi_{kj}^{\text{on}} \psi_j^{+,\text{off}}$ for $k = 1, \cdots, L_{\text{on}}$, where Ψ_{kj}^{on} is the jth component of Ψ_k^{on}. Then when parameter $\mu = \mu^*$ the online space in the oversampled region ω_i^+ is formed as

$$V_{\text{on}}^{+}(\mu^*) = \text{span}\{\psi_k^{+,\text{on}} : 1 \leqslant k \leqslant L_{\text{on}}\}. \tag{III.16}$$

III.4 Numerical results

In this section, we offer a variety of numerical results for two-dimensional problem

$$-\text{div}(\kappa(x;\mu)\nabla u) = 1,$$

with boundary condition $u = x + y$. We solve the global problem on the two-dimensional unit square $\Omega = [0,1]\times[0,1]$. The coarse discretization $\mathcal{T}^H$ is constructed by dividing Ω into 10×10 or 20×20 equal square sub-domains such that $H = 1/10$ or $1/20$. The fine discretization $\mathcal{T}^h$ is obtained by splitting each coarse-grid sub-domain into 10×10 or 5×5 small equal squares, respectively, so that the fine mesh has size $h = 1/100$ for both cases. In all numerical cases, we let $\tilde{\kappa} = H^2 \sum_i \kappa \nabla \chi_i^+ \cdot \nabla \chi_i^+$ where the partition of unity is chosen as the multiscale basis functions χ_i^+ defined below:

$$-\text{div}(\kappa \nabla \chi_i^+) = 0 \ \text{ in } \omega_i^+, \quad \chi_i^+ = \chi_i^0 \ \text{ in } \partial\omega_i^+. \tag{III.17}$$

Here χ_i^0 is the bilinear basis function (and we use linear boundary conditions). We consider two types of oversampled regions for the local problems, denoted by $\omega_i^{+1\text{f}}$

and ω_i^{+1c}, respectively. ω_i^{+1f} is obtained by adding a single layer of fine-grid blocks around ω_i and ω_i^{+1c} is obtained by adding one layer of coarse-grid blocks around ω_i. The numerical errors will be measured in weighted L^2 and weighted H^1 (i.e., energy) norms defined as

$$\|u\|_{L^2} = \left(\int_\Omega \|\kappa\|_2 u^2 \, dx\right)^{1/2}, \quad \|u\|_{H^1} = \left(\int_\Omega \kappa \nabla u \cdot \nabla u \, dx\right)^{1/2}$$

respectively, where $\|\kappa\|_2 = \sqrt{\lambda_{\max}(\kappa^*\kappa)}$ (κ^* denotes the conjugate transpose of κ).

III.4.1 Parameter-independent case

In this subsection we test the parameter-independent case in which $\kappa(x;\mu) = \kappa_1(x)$ and $\epsilon_1 = 10^{-5}$. In this case we do not need to construct the online space and the offline space will be used as the multiscale basis space for the global Galerkin coupling.

First we test the offline space in 10×10 coarse triangulation with oversampled region ω_i^{+1c} by harmonic extensions. The offline space (online space) is constructed in the snapshot space using the eigenvalue problems (III.8), (III.9) and (III.10) in ω_i^{+1c}. The error description is given in Table III.1, III.2 and III.3. We also present the index Λ_* in each case, where $\Lambda_* = \min_{\omega_i} \lambda^+_{\mathrm{L_{off}}+1}$ (see [33]). As we expected, both weighted errors decrease to some extent when we increase the dimension of the offline space. The residual errors are a limitation of the snapshot space (and subsequent offline space) to capture *all* relevant behavior of the system. However, to show our selection of the offline space is suitable, in Table III.4 we present the error between the GMsFEM solutions approximated in the snapshot space (i.e., maximum dimensional offline space) and a variety of lower-dimensional offline spaces, where the eigenvalue problem (III.10) is used. These convergence results confirm that the selected offline space as a subspace of the snapshot space indeed can be a good approximation space

with dimension-reduced basis.

$\dim(V_{\text{off}}^{+})$	Λ_*	$\|u - u^{+,\text{off}}\|$	
		$L^2(\Omega)$	$H^1(\Omega)$
796	0.15	3.23	27.02
1494	2.02×10^2	3.14	19.22
2134	1.40×10^3	3.12	14.20
2774	4.23×10^4	3.10	9.06

Table III.1: Relative errors (in %) between the fine-scale solution and offline spaces; Eigenvalue problem (III.8), 10×10 coarse mesh, harmonic snapshots, $\omega_i^+ = \omega_i^{+1c}$. See [50].

$\dim(V_{\text{off}}^{+})$	Λ_*	$\|u - u^{+,\text{off}}\|$	
		$L^2(\Omega)$	$H^1(\Omega)$
796	0.15	3.23	27.03
1494	2.02×10^2	3.14	19.23
2134	1.40×10^3	3.12	14.20
2774	4.23×10^4	3.11	9.12

Table III.2: Relative errors (in %) between the fine-scale solution and offline spaces; Eigenvalue problem (III.9), 10×10 coarse mesh, harmonic snapshots, $\omega_i^+ = \omega_i^{+1c}$. See [50].

Next, we test the offline space constructed in space of snapshots by eigenvalue problems. This is implemented by first selecting the dominant eigenvectors of the eigenvalue problem (III.4) in ω_i^{+1c} as the snapshot space, then applying the eigenvalue problem (III.10) and identifying the dominant modes as the offline space. The numerical results are presented in Table III.5. We note that the selection of an eigenvalue snapshot space offers more flexibility (and possibly more accuracy) in

$\dim(V_{\text{off}}^+)$	Λ_*	$\|u - u^{+,\text{off}}\|$	
		$L^2(\Omega)$	$H^1(\Omega)$
796	2.47×10^{-4}	3.27	27.05
1494	5.98×10^{-3}	3.18	19.27
2134	0.018	3.16	14.25
2774	36.79	3.13	9.12

Table III.3: Relative errors (in %) between the fine-scale solution and offline spaces; Eigenvalue problem (III.10), 10×10 coarse mesh, harmonic snapshots, $\omega_i^+ = \omega_i^{+1c}$. See [50].

$\dim(V_{\text{off}}^+)$	Λ_*	$\|u^{+,2774} - u^{+,\text{off}}\|$	
		$L^2(\Omega)$	$H^1(\Omega)$
796	2.47×10^{-4}	0.40	25.47
1494	5.98×10^{-3}	0.12	16.97
2134	0.018	0.09	10.94
2504	0.27	0.05	4.17

Table III.4: Relative errors (in %) between the maximal dimension offline solution and offline spaces; Eigenvalue problem (III.10), 10×10 coarse mesh, harmonic snapshots, $\omega_i^+ = \omega_i^{+1c}$. See [50].

the construction. More specifically, more eigenfunctions may directly included in the eigenvalue snapshot space, whereas the size of the harmonic snapshot space is limited by the dimension of the target boundary.

We also consider a smaller oversampled region ω_i^{+1f} which includes one layer of fine-grid blocks (see results in Table III.6). We observe in this example similar results as those in the first set of examples. Though a smaller oversampled region allows us to obtain more independent eigenvectors on the target domain, the irreducible error stays around 10%.

In the next set of numerical examples, we compute the GMsFEM solution on 20×20 coarse grid. The numerical results in Table III.7 are obtained when eigen-

$\dim(V_{\text{off}}^+)$	Λ_*	$\|u - u^{+,\text{off}}\|$	
		$L^2(\Omega)$	$H^1(\Omega)$
899	0.0089	3.17	26.81
2519	0.16	3.06	19.52
3539	1.90×10^3	2.98	13.88
4829	4.06×10^4	2.43	8.41

Table III.5: Relative errors (in %) between the fine-scale solution and offline spaces; Eigenvalue problem (III.10), 10×10 coarse mesh, eigenvalue snapshots, $\omega_i^+ = \omega_i^{+1c}$. See [50].

$\dim(V_{\text{off}}^+)$	Λ_*	$\|u - u^{+,\text{off}}\|$	
		$L^2(\Omega)$	$H^1(\Omega)$
899	1.50	3.13	26.97
2519	102.71	3.08	19.21
4139	373.93	3.07	14.13
4949	5.08×10^3	3.07	11.41

Table III.6: Relative errors (in %) between the fine-scale solution and offline spaces; Eigenvalue problem (III.10), 10×10 coarse mesh, harmonic snapshots, $\omega_i^+ = \omega_i^{+1f}$. See [50].

value problem (III.10) is applied in order to construct the solution space. In this case, it is expected that the space of harmonic snapshots can approximate the fine-grid solution more accurately than the case of a coarser grid. We still observe an irreducible residual error, although it is reduced by half to roughly 5%. In Table III.8, we compare the GMsFEM solution to the maximal dimension offline solution approximated in the snapshot space. It is not a surprise that the weighted error becomes smaller and the irreducible residual error is reduced. As with the examples in Table III.5, in Table III.9 we present the case when the snapshot space consists of eigenvectors defined in (III.4). The numerical result does not reflect a significant improvement over the 10×10 case possibly because of the dependency of the eigen-

vectors due to a smaller target domain. A smaller oversampled region ω_i^{+1f} is also considered (see result in Table III.10). Compared to the result in region ω_i^{+1c}, we see that the addition of more eigenvectors does not guarantee better convergence.

$\dim(V_{\text{off}}^+)$	Λ_*	$\|u - u^{+,\text{off}}\|$	
		$L^2(\Omega)$	$H^1(\Omega)$
1834	0.078	1.92	34.93
2857	0.37	1.46	15.46
3549	1.92×10^3	1.42	11.44
4485	2.06×10^4	1.42	5.53

Table III.7: Relative errors (in %) between the fine-scale solution and offline spaces; Eigenvalue problem (III.10), 20×20 coarse mesh, harmonic snapshots, $\omega_i^+ = \omega_i^{+1c}$. See [50].

$\dim(V_{\text{off}}^+)$	Λ_*	$\|u^{+,4485} - u^{+,\text{off}}\|$	
		$L^2(\Omega)$	$H^1(\Omega)$
1834	0.078	0.84	34.49
2857	0.37	0.08	14.55
3549	1.92×10^3	0.02	10.19
4125	8.03×10^3	0.008	6.58

Table III.8: Relative errors (in %) between the maximal dimension offline solution ($u^{+,4485}$) and offline spaces; Eigenvalue problem (III.10), 20×20 coarse mesh, harmonic snapshots, $\omega_i^+ = \omega_i^{+1c}$. See [50].

The last result we show for the parameter-independent case is the correlation between the energy errors and $1/\Lambda_*$. It was demonstrated that the energy norm is proportionally controlled by $(1/\Lambda_*)^{\frac{1}{2}}$. We plot the correlation for the 10×10 case in Figure III.4(a) and III.4(c), for the 20×20 case in Figure III.4(b) and III.4(d) . We

$\dim(V_{\text{off}}^{+})$	Λ_*	$\|u - u^{+,\text{off}}\|$	
		$L^2(\Omega)$	$H^1(\Omega)$
2174	0.07	2.10	34.49
3978	0.58	1.43	15.68
5784	1.50	1.43	12.04
7589	67.26	1.42	9.78

Table III.9: Relative errors (in %) between the fine-scale solution and offline spaces; Eigenvalue problem (III.10), 20×20 coarse mesh, eigenvalue snapshots, $\omega_i^+ = \omega_i^{+1c}$. See [50].

$\dim(V_{\text{off}}^{+})$	Λ_*	$\|u - u^{+,\text{off}}\|$	
		$L^2(\Omega)$	$H^1(\Omega)$
2174	0.26	1.94	34.58
3979	1.39	1.43	15.41
6506	407.49	1.42	11.39
7368	3.41×10^3	1.42	5.76

Table III.10: Relative errors (in %) between the fine-scale solution and offline spaces; Eigenvalue problem (III.10), 20×20 coarse mesh, harmonic snapshots, $\omega_i^+ = \omega_i^{+1f}$. See [50].

see that 10×10 coarse mesh yields a weaker correlation (correlation coefficients of roughly 0.90) between the energy norm and $(1/\Lambda_*)^{\frac{1}{2}}$, as compared to the 20×20 finer mesh (correlation coefficient of roughly 0.98). However, the all plots illustrate a clear correlation between the proportionality of the energy error and spectral behavior of the system.

III.4.2 Parameter-dependent case

In this subsection, we consider a parameter-dependent example in which the distribution of the conductivity is controlled by a parameter. In particular, we assume

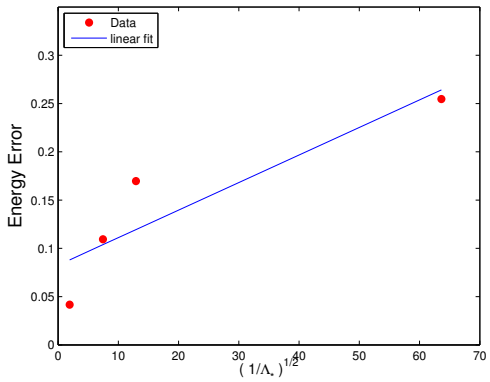

(a) Table III.4, corrcoef = 0.89

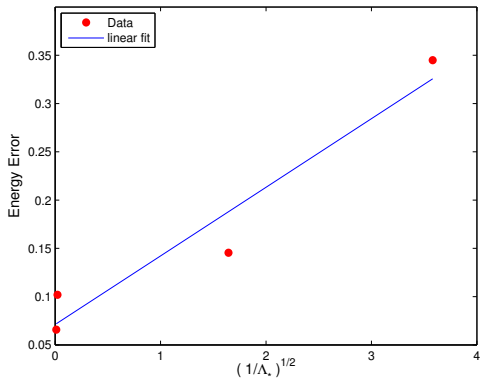

(b) Table III.8, corrcoef = 0.97

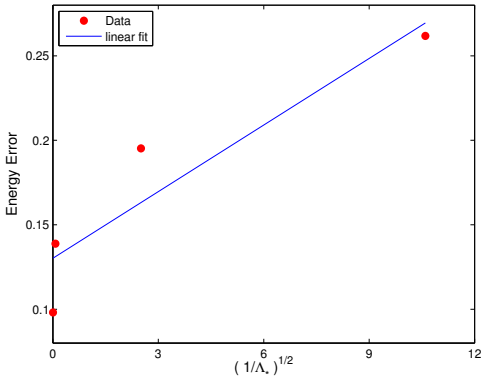

(c) Table III.5, corrcoef = 0.93

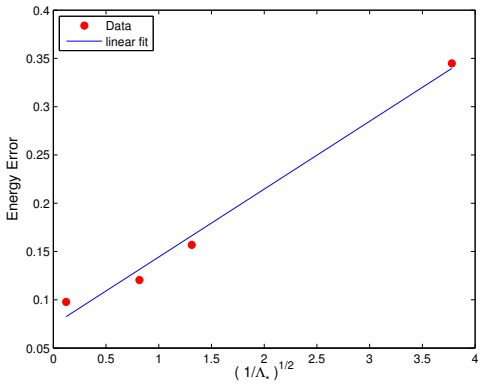

(d) Table III.9, corrcoef = 0.99

Figure III.4: Relation between relative energy error and Λ_* for Table III.4, III.8, III.5, and III.9 respectively. See [50].

that the conductivity takes the form

$$\kappa(x;\mu) = (1-\mu)\kappa_1(x) + \mu\kappa_2(x),$$

where $0 \leqslant \mu \leqslant 1$ and $\kappa_1(x)$, $\kappa_2(x)$ are shown in Figure III.1 ($\epsilon_1 = \epsilon_2 = 10^{-5}$). For this case, the construction of the snapshot space involves specifying nine fixed values of μ in order to create the snapshot functions on each coarse oversampled region. In the example, the online space is obtained by the following steps: 1. creating the snapshot

space by applying eigenvalue problem (III.4) and then removing the dependency of the nine sets of dominate eigenvectors; 2. forming the offline space by solving one of the eigenvalue problems (III.8), (III.9) and (III.10) with μ-averaged coefficients; 3. finally constructing the online space in the offline space by performing one of the eigenvalue problems (III.13), (III.14) and (III.15) with a fixed online parameter value $\mu^* = 0.5$. For the results in this subsection we use oversampled regions ω_i^{+1c}.

To further motivate more rigorous error comparisons, we first offer a representative set of solution plots in Figure III.5. As we can see, a coarse online space of too small a dimension yields a somewhat crude approximation to the fine scale solution. However, and increase in the size of the coarse dimension yields a solution that is essentially indistinguishable from the fine scale reference solution.

Detailed error comparisons are presented in Tables III.11, III.12 and III.13. The weighted errors between online solution and fine-scale solution (and offline solution) are shown to predictably decrease as we increase the dimension of the online space. Thus, we conclude that the variety of spectral problems posed in the oversampled regions, yield online GMsFEM solution spaces that accurately capture the fine scale solution.

$\dim(V_{\text{on}}^+)$	Λ_*	$\|u - u^{+,\text{on}}\|$		$\|u^{+,\text{off}} - u^{+,\text{on}}\|$	
		$L^2(\Omega)$	$H^1(\Omega)$	$L^2(\Omega)$	$H^1(\Omega)$
899	1.12	4.02	27.95	3.20	27.48
2519	277.76	3.78	20.50	3.10	19.88
4402	6.80×10^3	3.37	12.10	2.65	11.04
4984	-	1.70	5.32	0.029	1.01

Table III.11: Relative errors (in %) between the fine-scale solution (and offline solution) and online spaces; Eigenvalue problem (III.13), 10×10 coarse mesh, eigenvalue snapshots, $\omega_i^+ = \omega_i^{+1c}$. See [50].

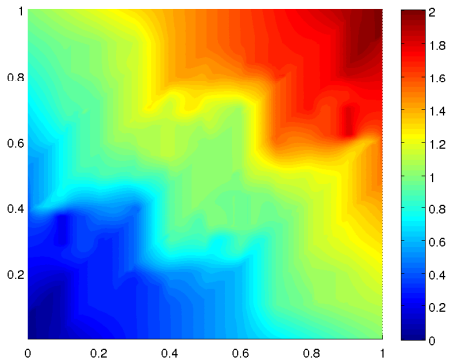

(a) GMsFEM solution, $\dim(V_{\text{on}}^{+}) = 251$

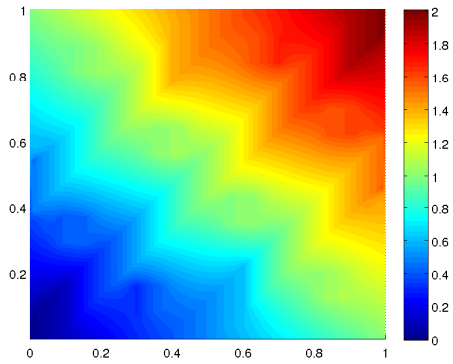

(b) GMsFEM solution, $\dim(V_{\text{on}}^{+}) = 2114$

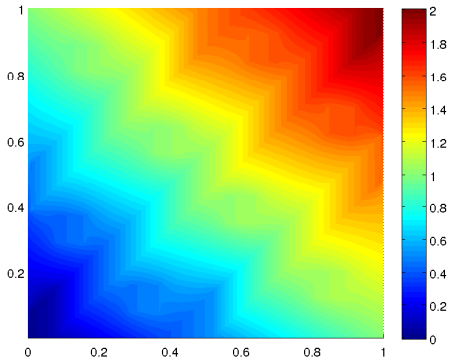

(c) Fine solution, $\dim(\mathcal{T}^h) = 10201$

Figure III.5: Solution plots corresponding to the error results in Table III.13. See [50].

III.5 Concluding remarks

In this chapter we have presented the Generalized Multiscale Finite Element Method (GMsFEM) aiming at the construction of accurate, reduced-dimensional approximation spaces for single-phase flow problems with high-contrast, high-anisotropy, and parameter-dependent coefficients. The framework uses an offline-online procedure in which the smaller-dimensional online space is computed in the fixed offline space using specified local eigenvalue problems. Several bilinear forms associated to

$\dim(V_{\text{on}}^+)$	Λ_*	$\|u - u^{+,\text{on}}\|$		$\|u^{+,\text{off}} - u^{+,\text{on}}\|$	
		$L^2(\Omega)$	$H^1(\Omega)$	$L^2(\Omega)$	$H^1(\Omega)$
899	1.14	4.17	27.97	3.27	27.43
2519	2.59	3.78	20.50	3.01	19.79
4402	6.80×10^3	3.67	12.10	2.56	10.88
4984	-	1.69	5.34	0.0055	0.90

Table III.12: Relative errors (in %) between the fine-scale solution (and offline solution) and online spaces; Eigenvalue problem (III.14), 10×10 coarse mesh, eigenvalue snapshots, $\omega_i^+ = \omega_i^{+1c}$. See [50].

$\dim(V_{\text{on}}^+)$	Λ_*	$\|u - u^{+,\text{on}}\|$		$\|u^{+,\text{off}} - u^{+,\text{on}}\|$	
		$L^2(\Omega)$	$H^1(\Omega)$	$L^2(\Omega)$	$H^1(\Omega)$
899	0.0064	4.70	29.18	3.63	28.67
2519	3.74	3.78	20.50	3.01	17.80
4402	6.80×10^3	3.37	12.09	2.56	10.89
4984	-	1.70	5.40	0.0039	0.63

Table III.13: Relative errors (in %) between the fine-scale solution (and offline solution) and online spaces; Eigenvalue problem (III.15), 10×10 coarse mesh, eigenvalue snapshots, $\omega_i^+ = \omega_i^{+1c}$. See [50].

the eigenvalue problems are presented. In particular, all such eigenvalue problems allow us to flexibly choose a set of online eigenvectors that offer a predictable error decline. In other words, the construction of larger dimension online spaces (by adding more eigenvectors) allows us to more accurately capture the behavior of the system. The supporting numerical examples show that GMsFEM offers an accurate and efficient framework for treating the high-contrast anisotropic problems considered in this chapter. Compared to our results in Chapter II, in this chapter, we consider the more general framework GMsFEM with the presence of parameter-dependent coefficients, harmonic snapshots, and oversampling techniques. This general framework can be helpful solving more general anisotropic problems in perforated domains, elasticity

field or in mixed forms.

IV A MULTILEVEL METHOD FOR THE GENERALIZED MULTISCALE FINITE ELEMENT METHOD

IV.1 Introduction

In this chapter, we present a multilevel method for constructing the coarse solution space in the framework of the Generalized Multiscale Finite Element Method (GMsFEM).

We have discussed some of the advantages of the GMsFEM and also refer to [25, 26, 28, 29, 40, 50]. Next, we briefly outline some of the aspects of the GMsFEM where some further improvements are needed. The systematic construction of multiscale basis functions in the GMsFEM [24] distinguishes this approach from the other multiscale finite methods. The multiscale basis functions are determined (following an offline-online procedure) by using local snapshot spaces and local spectral problems. At the offline stage, we construct the snapshot space by solving a set of local problems that involve all possible boundary conditions. The offline space is then generated by performing spectral decomposition in the snapshot space. The offline space is further used to construct the multiscale solution space at the online stage.

The GMsFEM discussed previously is a two-level method, where coarse basis functions are numerically computed within the coarse sub-domains on the fine grids. Though these local computations occurring at the offline stage could be viewed as a pre-computation process, it can be very expensive when the fine grid is sufficiently small. The strong anisotropy will further burden the local computations. To save the computational cost at the offline stage, we propose to employ a multilevel method to hierarchically compute the coarse basis functions. This is motivated by the fact that multilevel methods could significantly increase the computational speed be-

cause of the fewer degrees of freedom involved in the local couplings. There are various approaches within multilevel techniques can be used to speed-up the calculations. These can include multilevel snapshot calculations, multilevel eigenvalue solution techniques when the snapshot space consists of all fine-grid vectors, multilevel procedures in the online stage and so on. We refer to [31, 32, 53], where the authors proposed multilevel approaches for solving local spectral problems. In these approaches, the snapshot space is not used (or, the snapshot space consists of all fine-grid vectors). As a consequence, one of the challenges in these approaches is the construction of the partition of unity functions. The authors use partition of unity on the fine grid or their procedures can not guarantee the optimal partition of unity functions. The main idea of our proposed approach is to employ multilevel techniques in computing harmonic snapshots. As we discussed earlier, with harmonic snapshot functions, one can use oversampling techniques, which is not possible within previous approaches. Thus, the design of multilevel approaches for constructing harmonic snapshot functions is important, which is a focus of this chapter.

In order to compute multiscale basis functions, we design an algorithm for recursively constructing the snapshot spaces and the offline spaces. In particular, a nested sequence of snapshot spaces are computed where the snapshot space associated with the current grid is sought from the one related to the previous finer grid. We also prove that following such multilevel construction, the resulting multiscale solution space can adequately approximate the fine-scale solution up to the desired accuracy.

The rest of this chapter is organized as follows. In Section IV.2, we present preliminaries and a brief introduction of the two-level GMsFEM. Section IV.3 is devoted to the detailed multilevel construction of the multiscale solution space. Numerical experiments and the time complexity analysis are presented in Section IV.4. Some convergence analysis is provided in Section IV.5. We conclude this chapter by Section

IV.6.

IV.2 Preliminaries

IV.2.1 Problem formulation

Let $\Omega \subset R^d$, $d = 2, 3$, be a bounded polygonal domain. Consider the anisotropic high-contrast elliptical problem:

$$\begin{aligned} -\text{div}(\kappa(x)\nabla u) &= f \quad \text{in} \quad \Omega, \\ u(x) &= 0 \quad \text{on} \quad \partial\Omega, \end{aligned} \tag{IV.1}$$

where $\kappa(x)$ is a symmetric matrix with high-contrast and high-anisotropy. The variational formulation of problem (IV.1) is again given as finding $u \in V$ such that

$$a_\Omega(u, v) = (f, v), \quad \text{for all } v \in V, \tag{IV.2}$$

where $a_\Omega(u, v) = \displaystyle\int_\Omega \kappa(x)\nabla u \cdot \nabla v$, $(f, v) = \displaystyle\int_\Omega fv$, and $V = H_0^1(\Omega)$.

Here, we use the same notations $\mathcal{T}_h$ and $\mathcal{T}^H$ (defined in Section III.2) to respectively denote the fine and coarse triangulation, ω_i and ω_i^+ (defined in Chapter III) to respectively denote the neighborhood and oversampling region of the coarse node x_i. Then, the discrete problem, as before, consists of finding $u_H \in V_H$ such that

$$a_\Omega(u_H, v) = (f, v), \quad \text{for all } v \in V_H. \tag{IV.3}$$

Here $V_H \subset V$ is a conforming coarse solution space associated with $\mathcal{T}^H$. For the notational convenience, we will denote the continuous variables and the corresponding discrete quantities with the same symbols.

IV.2.2 Two-level GMsFEM

Though we have described this before, I briefly outline the GMsFEM and present the two-level construction of the coarse solution space V_H.

In the two-level GMsFEM framework, first, we construction of the local snapshot space $V_{\text{snap}}^{\omega_i^+}$. In particular, we numerically solve local problems for all possible boundary conditions on the oversampled region ω_i^+. The oversampling technique considered here increases the accuracy of approximated solutions. Now, let b_i be the collection of fine-grid boundary nodes on $\partial\omega_i^+$. Then, the local problem associated with ω_i can be formulated as

$$-\text{div}(\kappa(x)\nabla\psi_{\text{snap},p}^{i,+}) = 0 \quad \text{in} \quad \omega_i^+, \tag{IV.4}$$

$$\psi_{\text{snap},p}^{i,+} = \delta^p(x) \quad \text{on} \quad \partial\omega_i^+. \tag{IV.5}$$

Here, the fine-grid function $\delta^p(x)$ in (IV.5) is defined on b_i with value $\delta^p(x_q) = \delta_{pq}$ for $x_q \in b_i$. The local snapshot space $V_{\text{snap}}^{\omega_i^+}$ will consist of snapshot functions $\{\psi_{\text{snap},p}^{i,+} : x_p \in b_i\}$.

Next, a small dimensional offline space $V_{\text{off}}^{\omega_i^+}$ is sought in $V_{\text{snap}}^{\omega_i^+}$ by performing the following eigenvalue problem

$$A_{\text{off}}^+\Psi_k = \lambda_k M_{\text{off}}^+\Psi_k, \tag{IV.6}$$

where $A_{\text{off}}^+ = [a_{kl}] = \int_{\omega_i^+}\kappa(x)\nabla\psi_{\text{snap},k}^{i,+}\cdot\nabla\psi_{\text{snap},l}^{i,+}$ and $M_{\text{off}}^+ = [m_{kl}] = \int_{\omega_i^+}\tilde{\kappa}(x)\psi_{\text{snap},k}^{i,+}\cdot\psi_{\text{snap},l}^{i,+}$. Here, the weighted coefficient $\tilde{\kappa}(x)$ is defined in Chapter III. To form the offline space, we first pick the smallest N eigenvalues of the problem (IV.6), $\{\lambda_k\}_{k=1}^N$; then we set a function $\psi_{\text{off},k}^{i,+}$ to be a linear combination of the snapshot functions with weights $\{\Psi_{k,j}\}$. That is, $\psi_{\text{off},k}^{i,+} = \sum_j \Psi_{k,j}\psi_{\text{snap},j}^{i,+}$, $1 \le k \le N$, where $\Psi_{k,j}$ is the

jth component of Ψ_k. Then, the multiscale basis function associated with node x_i is defined by

$$\phi_j^{\omega_i} = \chi_i \psi^i_{\text{off},j}, \quad 1 \leq j \leq N, \tag{IV.7}$$

where $\{\chi_i\}_{i=1}^{N_v}$ is a partition of unity associated with $\{\omega_i : \ 1 \leq i \leq N_v\}$ and $\psi^i_{\text{off},j}$ is the restriction of $\psi^{i,+}_{\text{off},j}$ on ω_i. The offline space V_{off} can be generated by the set $\{\phi_j^{\omega_i} : \ 1 \leq j \leq N, \ 1 \leq i \leq N_v\}$. Because the problem (IV.1) is parameter independent, the coarse solution space V_H is chosen to be V_{off}. We remark that besides (IV.6), alternative eigenvalue problems can also be used (see III.13, III.14, and III.15).

IV.3 Multilevel methods

In this section, we extend our construction to a multilevel setting. We can recursively call the two-level construction. In particular, the output (snapshot space and offline space) obtained in the previous level is input data for the current level construction. Therefore, we can view a L-level problem as $L-1$ two-level problems.

We consider a polygonal 2-D domain Ω and assume that $\mathcal{T}^L \subset \cdots \subset \mathcal{T}^l \cdots \subset \mathcal{T}^1$, $1 < l < L$, are nested quadrilateral triangulations of Ω with grid size $h_L > \cdots > h_l \cdots > h_1$. $\mathcal{T}^1$ is the finest grid, and $\mathcal{T}^L$ is the coarsest (target) grid where the final multiscale solution space will be computed. Given $\mathcal{T}^{l+1}$, we generate a finer grid $\mathcal{T}^l$ by refining $\mathcal{T}^{l+1}$. Then, the discrete problem reads as follows. We seek a numerical approximation $u_L \in V^L_{\text{off}}$ such that

$$a_\Omega(u_L, v) = (f, v), \quad \text{for all } v \in V^L_{\text{off}}, \tag{IV.8}$$

where $V^L_{\text{off}} \subset V$ is a conforming multiscale solution space associated with $\mathcal{T}^L$.

The key ingredient of designing a robust and efficient multilevel method for solv-

ing (IV.8) is the construction of a sequence of multiscale solution spaces $V_{\text{off}}^1, \cdots, V_{\text{off}}^l, \cdots, V_{\text{off}}^L$, where V_{off}^l denotes the solution space associated with the mesh $\mathcal{T}^l$. Note that, here, V_{off}^1 is the standard finite element space associated the finest mesh. In order to obtain V_{off}^l, we need to construct a snapshot space $V_{\text{snap}}^{l,+}$ via local problems with harmonic extension boundary conditions. Once we have $V_{\text{snap}}^{l,+}$, V_{off}^l can be generated by a set of localized eigenvalue problems (IV.6) and corresponding restrictions. We emphasize, here, that our approach provides the construction of $V_{\text{snap}}^{l,+}$ only based on V_{off}^{l-1} and $V_{\text{snap}}^{l-1,+}$. The snapshot/offline spaces that are associated with the mesh $\mathcal{T}^1, \cdots \mathcal{T}^{l-2}$ will not be used. This construction yields savings because of the reduced-dimensional space V_{off}^{l-1}.

IV.3.1 Notations

To improve readability, we collect below the most relevant notations, while their precise definitions will be given later in the text.

$\mathcal{T}^l$: triangulation of Ω at level l.

h_l : grid size of $\mathcal{T}^l$.

x_i^l : i-th grid node in $\mathcal{T}^l$.

ω_i^l : neighborhood of the node x_i^l.

$\omega_i^{l,+}$: oversampling region of ω_i^l.

I_i^l : collection of inner nodes in $\omega_i^{l,+}$ over $\mathcal{T}^{l-1}$.

B_i^l : collection of the finest-grid boundary nodes on $\partial\omega_i^{l,+}$ over $\mathcal{T}^1$.

$\psi_{i,p}^{l,+}$: local snapshot function with respect to $\omega_i^{l,+}$.

$\psi_{i,p}^l$: restriction of $\psi_{i,j}^{l,+}$ to ω_i^l.

$V_{\text{snap},i}^{l,+}$: local snapshot space with respect to $\omega_i^{l,+}$.

V_{snap}^l : snapshot space with respect to $\mathcal{T}^l$.

$V_{\text{off},i}^l$: local solution space with respect to ω_i^l.

$\phi_{i,p}^l$: basis function of $V_{\text{off},i}^l$.

V_{off}^l : coarse solution space with respect to $\mathcal{T}^l$.

IV.3.2 Local problems

To obtain V_{off}^L, we need to construct $V_{\text{off}}^2, \cdots, V_{\text{off}}^{L-1}$ in a sequence. We assume that V_{off}^1 is the finite element solution space with respect to the finest grid. Therefore, we will run $L-1$ iterations to arrive at the target level L. Nevertheless, each iteration can be viewed as a two-level problem as we did for the construction in the GMsFEM. Assume now that for some l, $2 \leq l \leq L$, we are given $V_{\text{snap}}^{l-1,+}$ and V_{off}^{l-1}. Based on this, we can construct V_{off}^l as follows.

A local snapshot space $V_{\text{snap},i}^{l,+}$ is constructed by solving local problems on an oversampling domain $\omega_i^{l,+}$. The imposed boundary conditions should be able to capture all possible solution behaviors in $\omega_i^{l,+}$. A usual choice is to choose all the delta functions $\delta_p^1(x)$ that are defined on the finest-grid nodes on $\partial\omega_i^{l,+}$. The local problem to solve consists of finding a snapshot function $\psi_{i,p}^{l,+} \in V_{\text{off}}^{l-1}(\omega_i^{l,+}) \cup V_{\text{snap}}^{l-1,+}(\omega_i^{l,+})$, such that

$$\begin{aligned} -\text{div}(\kappa(x)\nabla\psi_{i,p}^{l,+}) = 0 \quad &\text{in} \quad \omega_i^{l,+}, \\ \psi_{i,p}^{l,+} = \delta_p^1 \quad &\text{on} \quad \partial\omega_i^{l,+}. \end{aligned} \tag{IV.9}$$

Here $\delta_p^1(x_j^1) = \delta_{pj}$, where x_j^1 is the finest-grid boundary node on $\partial\omega_i^{l,+}$. Note that the snapshot function to be sought is in the snapshot and offline space of the previous level $l-1$.

Due to the fact that the boundary condition is defined on the finest grid, we have to take into account all the finest-grid degrees of freedom on $\partial\omega_i^{l,+}$. Therefore, to define boundary basis functions becomes the key to solve (IV.9). Details of the creation of boundary basis functions will be discussed in the next subsection. Assume now with these boundary basis functions, denoted by $\widetilde{\phi}_j^{l-1}$, we consider solving (IV.9) in the space $V_{\text{off}}^{l-1}(\omega_i^{l,+})\bigcup\{\widetilde{\phi}_j^{l-1} : x_j^1 \in B_i^l\}$. More precisely, for an interior node x_j^{l-1} in $\omega_i^{l,+}$ (i.e., $x_j^{l-1} \in I_i^l$), we equip its basis functions with $\{\phi_{j,k}^{l-1} : k = 1, 2, \cdots\}$, where $\phi_{j,k}^{l-1} \in V_{\text{off}}^{l-1}(\omega_i^{l,+})$ is the basis function associated to the node x_j^{l-1}; for a boundary node x_j^1 on $\partial\omega_i^{l,+}$ (i.e., $x_j^1 \in B_i^l$), we let its basis function be $\widetilde{\phi}_j^{l-1}$. Then, the snapshot function $\psi_{i,p}^{l,+}$ solving (IV.9) is of the form:

$$\sum_{x_j^{l-1}\in I_i^l}\left(\sum_k c_{i,k}\phi_{j,k}^{l-1}\right) + \sum_{x_j^1\in B_i^l} d_j\widetilde{\phi}_j^{l-1}. \tag{IV.10}$$

Here, I_i^l denotes the collection of the interior nodes in $\omega_i^{l,+}$ over $\mathcal{T}^{l-1}$; B_i^l denotes the collection of the finest-grid boundary nodes on $\partial\omega_i^{l,+}$. Note that the coefficient $d_j = \delta_p^1(x_j^l) = \delta_{pj}$.

To obtain the snapshot space $V_{\text{snap},i}^{l,+}$, we impose boundary conditions $\delta_p^1(x)$ for all p (x_p^1 is on $\partial\omega_i^{l,+}$). Then, we obtain the local snapshot spaces

$$V_{\text{snap},i}^{l,+} \;=\; \text{span}\{\psi_{i,p}^{l,+} :\; x_p^1 \text{ on } \;\partial\omega_i^{l,+}\} \tag{IV.11}$$

and

$$V_{\text{snap},i}^{l} \;=\; \text{span}\{\psi_{i,p}^{l} :\; x_p^1 \text{ on } \;\partial\omega_i^{l,+}\}, \tag{IV.12}$$

where $\psi_{i,p}^l$ is the restriction of $\psi_{i,p}^{l,+}$ on ω_i^l.

To obtain the offline/solution space V_{off}^l, an auxiliary spectral decomposition is

used to identify the dominant modes in $V_{\text{snap},i}^{l,+}$. In particular, for each $\omega_i^{l,+}$, we define the following eigenvalue problems

$$A_i^{l,+}\Theta_k \;=\; \lambda_{i,k}^{l,+} M_i^{l,+}\Theta_k, \tag{IV.13}$$

$$A_i^{l,+}\Theta_k \;=\; \lambda_{i,k}^{l} M_i^{l}\Theta_k, \tag{IV.14}$$

$$A_i^{l}\Theta_k \;=\; \lambda_{i,k}^{l} M_i^{l}\Theta_k, \tag{IV.15}$$

where

$$A_i^{l,+} \;=\; [a_{pq}] \;=\; \int_{\omega_i^{l,+}} \kappa(x)\nabla\psi_{i,p}^{l,+}\cdot\nabla\psi_{i,q}^{l,+},$$

$$A_i^{l} \;=\; [a_{pq}] \;=\; \int_{\omega_i^{l}} \kappa(x)\nabla\psi_{i,p}^{l}\cdot\nabla\psi_{i,q}^{l},$$

$$M_i^{l,+} \;=\; [m_{pq}] \;=\; \int_{\omega_i^{l,+}} \widetilde{\kappa}(x)\psi_{i,p}^{l,+}\psi_{i,q}^{l,+},$$

$$M_i^{l} \;=\; [m_{pq}] \;=\; \int_{\omega_i^{l}} \widetilde{\kappa}(x)\psi_{i,p}^{l}\psi_{i,q}^{l}.$$

The coefficient $\widetilde{\kappa}(x)$ is a scalar weight associated with the coefficient $\kappa(x)$. In this chapter, we define $\widetilde{\kappa} = h_l^2 \sum_i \kappa\nabla\chi_i^l\cdot\nabla\chi_i^l$, where χ_i^l denotes the bilinear basis function in $\mathcal{T}^l$. We apply (IV.13) and identify the dominant modes by choosing the eigenvectors corresponding to the smallest s_i^l eigenvalues and setting

$$\widetilde{\psi}_{i,k}^{l,+} \;=\; \sum_p \Theta_{kp}\psi_{i,p}^{l,+}, \quad k = 1, 2, \cdots, s_i^l, \tag{IV.16}$$

where Θ_{kp} is the p-th component of Θ_k. Denote $\widetilde{\psi}_{i,k}^{l}$ as the restriction of $\widetilde{\psi}_{i,k}^{l,+}$ to ω_i^l. The coarse basis functions associated with the node x_i^l are obtained by multiplying

the dominant modes by χ_i^l, i.e., $\phi_{i,k}^l = \chi_i^l \widetilde{\psi}_{i,k}^l$. Then, we have the local solution space

$$V_{\text{off},i}^l \;=\; \text{span}\{\phi_{i,k}^l :\; k = 1, 2, \cdots, s_i^l\}, \tag{IV.17}$$

and the global coarse solution space is formed as

$$V_{\text{off}}^l \;=\; \bigcup_i V_{\text{off},i}^l \;=\; \text{span}\{\phi_{i,k}^l :\; i = 1, 2, \cdots, N^l, \;\; k = 1, 2, \cdots, s_i^l\}, \tag{IV.18}$$

where N^l is the number of grid nodes in $\mathcal{T}^l$.

Algorithm 1: Construction of the coarse solution space using a multilevel method.

Input : $\kappa(x)$, $\mathcal{T}^l (1 \le l \le L)$, V_{off}^1
Output: V_{off}^L

```
for l=2:L do
    V_snap^{l,+} = {},  V_off^l = {}.
    for ω_i^{l,+} ⊂ T^l do
        Build basis functions for the local problem (IV.9).
        for x_j^{l-1} ∈ I_i^l do
            Inner basis: φ_{j,k}^{l-1} (k = 1, 2, ···).
        end
        for x_j^1 ∈ B_i^l do
            Boundary basis: see Subsection IV.3.3.
        end
        Solve the local problem (IV.9) for ψ_{i,j}^{l,+}.
        Form a local snapshot space: V_{snap,i}^{l,+} = span{ψ_{i,j}^{l,+} : x_j^1 ∈ B_i^l}.
        Update V_snap^{l,+}.
        Form a local solution space V_{off,i}^l using spectral decomposition (IV.13).
        Update V_off^l.
    end
end
```

Remark IV.3.1. *Note that $V_{snap,i}^{l,+}$ and $V_{snap,i}^{l}$ fully represent the behavior of the multiscale solution in $\omega_i^{l,+}$ and ω_i^l, respectively; $V_{off,i}^{l}$ is a dimension-reduced local solution space. More precisely, $V_{off,i}^{l}$ is a subspace of $\chi_i^l \cdot V_{snap,i}^{l}$.*

IV.3.3 Boundary basis functions

The essential part of solving (IV.9) is to build the boundary basis functions $\widetilde{\phi}_j^{l-1}$, for all the finest-grid nodes x_j^1 on $\partial\omega_i^{l,+}$. Recall that the snapshot space consists of vectors that characterize the behavior of the multiscale solution. Hence, a reasonable boundary basis function should be able to capture the multiscale information of the solution near the boundary of $\omega_i^{l,+}$. This motivates us to solve additional local problems to seek a "good" boundary basis function. Fortunately, our approach below can manage to avoid solving these expensive local problems. Our algorithm

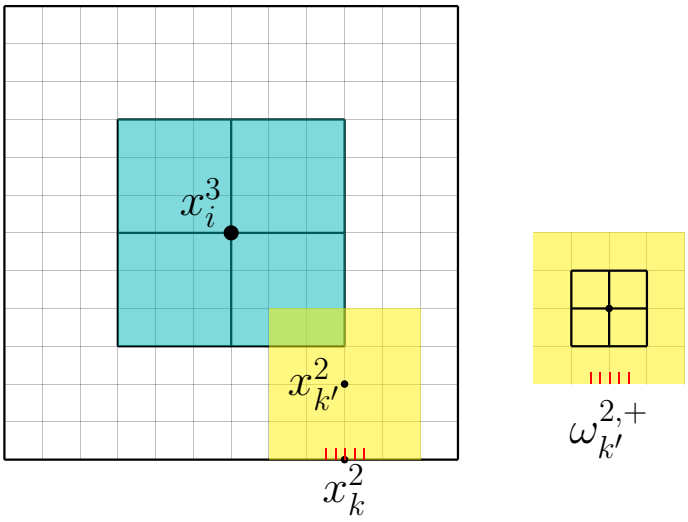

Figure IV.1: Left: an oversampling domain $\omega_i^{3,+}$ (the largest square) and a small oversampling domain $\omega_{k'}^{2,+} \subset \omega_i^{3,+}$. Right: $\omega_{k'}^{2,+}$, where the finest-grid boundary nodes to be considered on $\partial\omega_{k'}^{2,+}$ are marked in red.

is described below. First, for each x_k^{l-1} on $\partial\omega_i^{l,+}$, find the corresponding oversampling

domain $\omega_{k'}^{l-1,+} \subset \omega_i^{l,+}$. We require x_k^{l-1} to be located at the center of one edge of $\partial\omega_{k'}^{l-1,+}$ (in the case that x_k^{l-1} is around the corner of $\omega_i^{l,+}$, we let $\omega_{k'}^{l-1,+}$ to be also at the corner of $\omega_i^{l,+}$). Second, we find an interval F_k of length h_{l-1} on $\partial\omega_{k'}^{l-1,+}$, such that x_k^{l-1} is (close to) the center point of F_k. Next, we solve the following local problems on $\omega_{k'}^{l-1,+}$ with boundary conditions imposed on the finest-grid boundary nodes. For every finest-grid boundary node x_j^1 in F_k, find $\psi_{k',j}^{l-1,+}$ such that

$$\begin{aligned} -\mathrm{div}(\kappa(x)\nabla\psi_{k',j}^{l-1,+}) = 0 \quad &\text{in} \quad \omega_{k'}^{l-1,+}, \\ \psi_{k',j}^{l-1,+} = \delta_j^1 \quad &\text{on} \quad \partial\omega_{k'}^{l-1,+}. \end{aligned} \tag{IV.19}$$

We realize that the above problem has already been solved at the level $l-1$. In fact, $\psi_{k',j}^{l-1,+}$ is a snapshot function in $V_{\mathrm{snap},k'}^{l-1,+}$. In Figure IV.1, we illustrate a three-level sub-domain where $\omega_{k'}^{2,+}$ is filled in yellow and the needed boundary nodes in F_k are marked in red. Now, we define the boundary basis function as

$$\widetilde{\phi}_j^{l-1} = \chi_k^{l-1}\psi_{k',j}^{l-1,+}, \tag{IV.20}$$

where χ_k^{l-1} is the partition of unity function associated with x_k^{l-1}. After all x_k^{l-1} on $\partial\omega_i^{l,+}$ have been visited, the boundary basis functions can be created. The step-by-step algorithm is summarized in Algorithm 2.

Remark IV.3.2. *When x_k^{l-1} is around the corner of $\partial\omega_i^{l,+}$, the small oversampling domain $\omega_{k'}^{l-1,+}$ is located at the corner of $\omega_i^{l,+}$. In the case that x_k^{l-1} is a corner boundary node, the interval F_k will consist of two smaller segments that align with $\partial\omega_i^{l,+}$.*

Remark IV.3.3. *With the above construction of boundary basis functions, the non-zero boundary value for some snapshot functions $\psi_{i,p}^{l,+}$ of (IV.9) may differ from 1.*

Algorithm 2: Construction of boundary basis functions.

Input : $\omega_i^{l,+}$, $V_{\text{snap}}^{l-1,+}$, χ_k^{l-1}.

Output: $\widetilde{\phi}_j^{l-1}$, for x_j^1 on $\partial\omega_i^{l,+}$.

1 Step 1: for every node x_k^{l-1} on $\partial\omega_i^{l,+}$, determine the proper $\omega_{k'}^{l-1,+}$.

2 Step 2: find the interval F_k.

3 Step 3: for every finest-grid boundary node $x_j^1 \in F_k$, solve the problem (IV.19) for $\psi_{k',j}^{l-1,+}$.

4 Step 4: load $V_{\text{snap},k'}^{l-1,+}$.

5 Step 5: define $\widetilde{\phi}_j^{l-1} = \chi_k^{l-1}\psi_{k',j}^{l-1,+}$.

However, it does not matter since it only differs by a factor that is greater than or equal to $1/2$. *Such snapshot functions can still capture the multiscale information near the boundary of* $\omega_i^{l,+}$.

IV.4 Numerical results

IV.4.1 Numerical experiments

In this section, we present a variety of numerical experiments that demonstrate good performance of the GMsFEM in a multilevel manner. The computational domain Ω is chosen to be a unit square $[0,1] \times [0,1]$. We set the force term $f(x) = 1$, and use boundary condition $u = 0$. The numerical errors will be measured in weighted L^2 and energy norm H^1 defined as

$$\|u\|_{L^2} = \left(\int_\Omega ||\kappa||_2 u^2\right)^{1/2} \quad \text{and} \quad \|u\|_{H^1} = \left(\int_\Omega \kappa\nabla u \cdot \nabla u\right)^{1/2},$$

respectively.

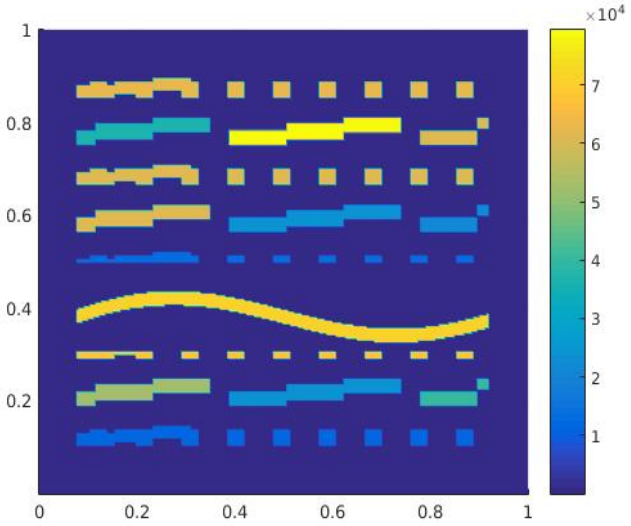

Figure IV.2: The component κ_{22} of $\kappa(x)$, where $\kappa(x) = \text{diag}(1, \kappa_{22})$.

$\dim(V_{\text{off}}^3)$	$\|u_3 - u_1\|$	
	$L^2(\Omega)$	$H^1(\Omega)$
1125	7.56	28.71
2250	5.49	22.08
4500	3.75	16.17
9000	1.14	10.65

Table IV.1: Relative errors (in %) between the fine-scale solution and the GMsFEM solutions. 3-level problem with mesh: $[256\times256, 64\times64, 16\times16]$. Degrees of freedom at the fine scale: 66049.

Our first experiment is tested on multilevel grids: $[256 \times 256, 64 \times 64, 16 \times 16]$. Each $n \times n$ represents that the domain is divided into n by n small identical squares. The permeability field κ is depicted in Figure IV.2. We assume that the fine-scale solution is obtained by discretizing problem (IV.1) using the standard piecewise bilinear finite elements on the finest-grid (256×256). The total degrees of freedom at the fine scale is 66049. In Table IV.1, we show the convergence result for the

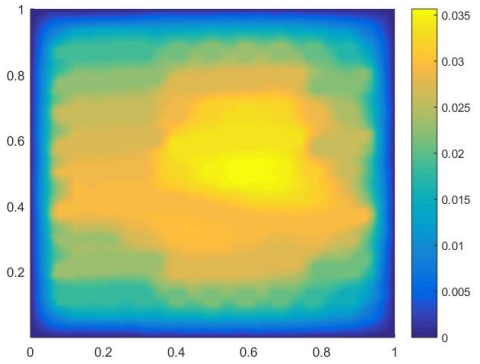

(a) GMsFEM solution, $\dim(V_{\text{off}}^3)$=1125.

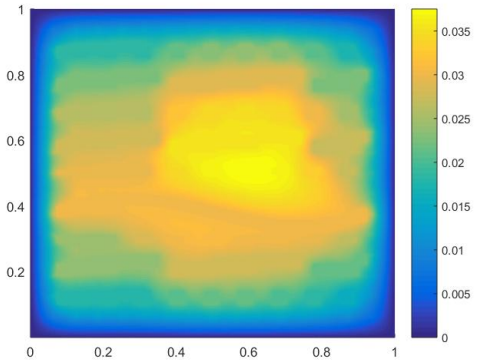

(b) GMsFEM solution, $\dim(V_{\text{off}}^3)$=4500.

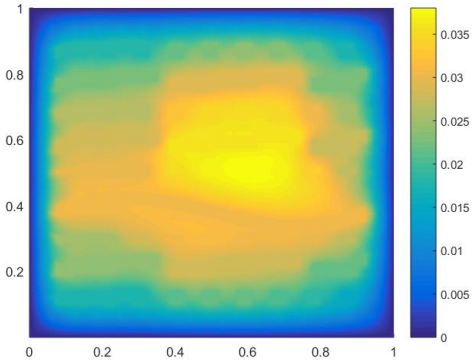

(c) GMsFEM solution, $\dim(V_{\text{off}}^3)$=9000.

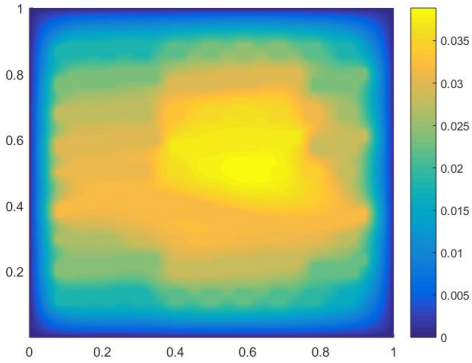

(d) Fine solution, $\dim(V_{\text{fine}})$=66049.

Figure IV.3: Solution plots corresponding to the error results in Table IV.1.

3-level problem. In the first column, we list the dimension of the offline space that is used to approximate the GMsFEM solution u_3. The dimension is determined by the number of dominant modes selected per coarse block, see (IV.13). In order to enrich the coarse solution space, we can add more dominant modes per interior coarse node. In the test, we increase the number of dominant modes per interior node from 5 to 40. Consequently, the dimension of the offline space increases from 1125 to 9000. We see that the weighted H^1 error decreases from 28.71% to 10.65%. Note that the GMsFEM has an irreducible error of order $O(H) \approx 6.25\%$. The error for u_3 decreases

to 10.65% when the coarse solution space is enriched with a dimension 9000 (out of 66049). The numerical result aligns with our convergence analysis that is presented in the next section. We plot the GMsFEM solutions as well as the fine-scale solution in Figure IV.3. In this experiment, we set the dimension of each local offline space to be 10 for the middle level (level 2).

$\dim(V_{\text{off}}^3)$	$\|u_3 - u_2^{\text{snap}}\|$	
	$L^2(\Omega)$	$H^1(\Omega)$
1125	2.13	14.65
2250	1.28	8.76
4500	0.35	7.73
9000	0.064	6.99

Table IV.2: Relative errors (in %) between the 3-level GMsFEM solution and the 2-level solution approximated in the full snapshot space. u_3: 3-level solution with mesh $[256\times256, 64\times64, 16\times16]$. u_2^{snap}: 2-level solution with mesh $[256\times256, 16\times16]$. The dimension of the 2-level snapshot space is 51456.

In Table IV.2, we compare the 3-level GMsFEM solution u_3 with the 2-level solution u_2^{snap}. Here, u_2^{snap} is approximated in the full snapshot space that is generated on the 2-level mesh $[256 \times 256, 16 \times 16]$. It is expected that the error between u_3 and u_2^{snap} is small due to the fact that the snapshot space can represent the fine-scale solution in some sense. Our results show that as we increase the coarse solution space, the error decreases consequently. The weighted L^2 and H^1 errors are less the ones in Table IV.1. In particular, the weighted L^2 error between u_3 and u_2^{snap} is much less compared with the one between u_3 and u_1. We also observe that the error is hard to decrease when the dimension if over 2250. This is due to the irreducible error of order $O(H) \approx 6.26\%$.

Our next experiment is to test a parameter-dependent permeability field. In

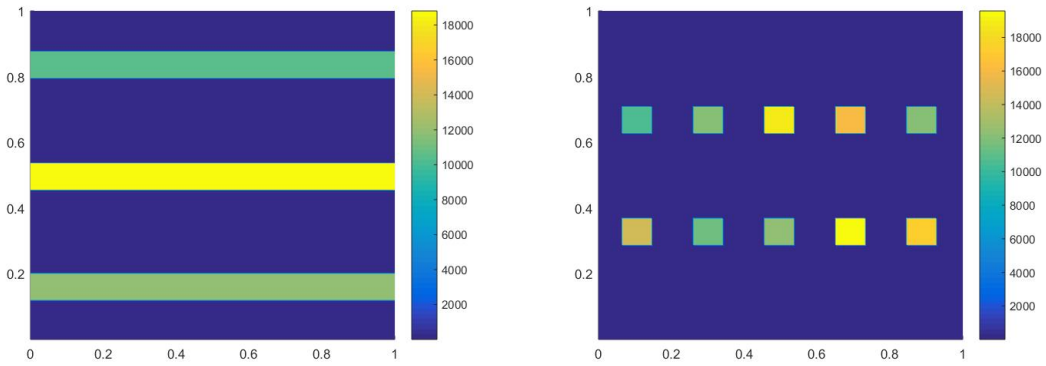

(a) $\kappa_{1,y}(x)$: y-direction in $\kappa_1(x)$ (b) $\kappa_{2,y}(x)$: y-direction in $\kappa_2(x)$

Figure IV.4: Left: $\kappa_1(x) = \text{diag}(1, \kappa_{1,y}(x))$. Right: $\kappa_2(x) = \text{diag}(1, \kappa_{2,y}(x))$.

particular, we assume the permeability is of the form $\kappa(x, \mu) = (1-\mu)\kappa_1(x)+\mu\kappa_2(x)$, where $0 \leq \mu \leq 1$ and $\kappa_1(x), \kappa_2(x)$ are shown in Figure IV.4 . For this case, the construction of multiscale solution space involves there stages (referred to Chapter III). First, specifying nine fixed values of μ to create the snapshot space at each level. Second, the construction of offline space is obtained by spectral decomposition with μ-averaged coefficients. Last, constructing the solution (online) space by performing eigenvalues problem with a fixed online parameter value $\mu^* = 1/2$. We offer a set of solution plots in Figure IV.5. As we increase the dimension of online space, it yields a solution that is essentially indistinguishable from the fine-scale solution. Detailed error comparisons are presented in Table IV.3. The weighted errors between the reference solution and the online solution are shown to predictably decrease as the dimension of the online space is increasing. Therefore, we can conclude that the 3-level GMsFEM solution accurately capture the fine scale solution.

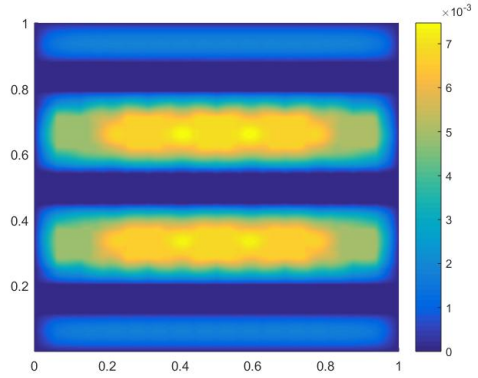

(a) GMsFEM solution, dim(V_{on}^3)=675.

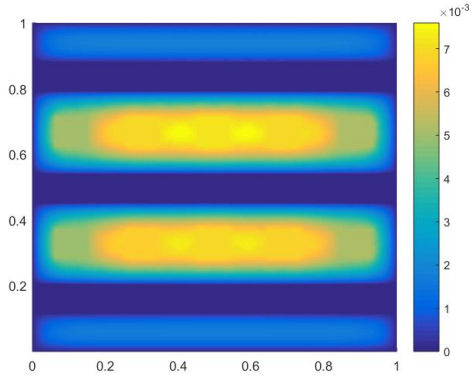

(b) GMsFEM solution, dim(V_{on}^3)=3375.

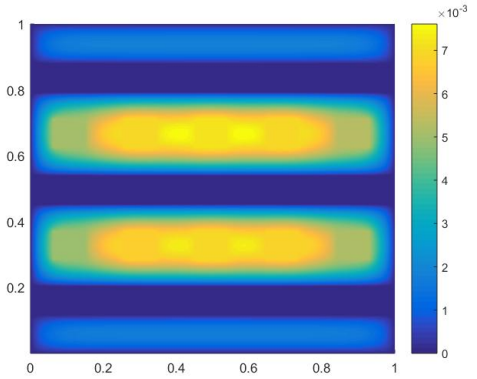

(c) Fine solution, dim(V_{fine})=66049.

Figure IV.5: Solution plots corresponding to the error results in Table IV.3.

IV.4.2 Complexity analysis

In this subsection, we briefly analyze the computational time complexity for the multilevel GMsFEM. The computational domain is a unit square. We assume: (1) the finest scale is the fixed length h, and the coarsest scale varies with the length $H = 10^n \cdot h,\ n \geq 1$; (2) we can access the global finest stiffness matrix A_h and the mass matrix M_h (note that the matrices A_h and M_h are assembled on the global domain using standard bilinear basis functions. Given a sub-domain, the corresponding local stiffness/mass matrix is the restriction of A_h/M_h to this sub-domain.); (3) if there

$\dim(V_{\text{on}}^3)$	$\|u_3 - u_1\|$	
	$L^2(\Omega)$	$H^1(\Omega)$
675	2.93	25.43
1800	0.47	9.20
3375	0.24	7.97

Table IV.3: Relative errors (in %) between the fine-scale solution and the GMsFEM solutions. 3-level problem with mesh: $[256\times256, 64\times64, 16\times16]$. Degrees of freedom at the fine scale: 66049.

are multiple levels, the scales of the middle levels are chosen such that the ratio $\frac{h_l}{h_{l-1}}$ possibly remains the same (in order to save the total cost); (4) we assume that in each local snapshot space, only the first 10 dominant modes are selected to form the corresponding offline space. With the above assumptions, we can calculate the time complexity as follows.

For each level, the construction of the coarse solution space involves two computations: the snapshot space and the offline space. In particular, to obtain a local snapshot space, it requires $\mathcal{O}\big(\text{dof}^2 + k\cdot\text{dof}\big) = \mathcal{O}\big(\text{dof}^2\big)$ flops. Here, k is the number of the finest-grid nodes along the boundary of this sub-domain, and dof stands for the number of degrees of freedom involved in this problem. We know that the local offline space is formed via a local eigenvalue problem. To solve the local eigenvalue problem, it needs $\mathcal{O}\big(10\cdot\text{dof}^2\big)$ flops. Here, the coefficient 10 is due to the fact that we only generate 10 eigenvectors (dominant modes) for each eigenvalue problem. Hence, to obtain a local coarse solution space, it requires $\mathcal{O}\big(10\cdot\text{dof}^2\big) + \mathcal{O}\big(\text{dof}^2\big) = \mathcal{O}\big(10\cdot\text{dof}^2\big)$ flops. Note that this cost is only for a local coarse solution space. As for the whole coarse solution space, the total cost depends on the number of sub-domains at that level. Below, we calculate the costs for the two-level case and three-level case.

Two-level GMsFEM:

In each sub-domain (oversampling domain) ω_i^+, the number of degrees of freedom is

$$\text{dof} = \mathcal{O}\big((4\frac{H}{h})^2\big).$$

The number of the sub-domains is

$$\#\text{ of sub-domains} = \mathcal{O}(1/H^2).$$

As a result, the computational cost for the two-level GMsFEM is

$$TC2 = \frac{1}{H^2}\mathcal{O}\big(10\cdot(\text{dof})^2\big) = \frac{1}{H^2}\mathcal{O}\big(10\cdot(4\frac{H}{h})^4\big) = \mathcal{O}\big(10\cdot 4^4\cdot\frac{H^2}{h^4}\big)$$

flops.

Three-level GMsFEM:

Now, we need to compute the coarse solution space for level 2 and level 3. From the analysis before, we know that the computational cost at the middle level (level 2) is $\mathcal{O}\big(10\cdot 4^4\cdot\frac{h_2^2}{h^4}\big)$, where h_2 denotes the length of the scale at the level 2. At the level 3, in each sub-domain $\omega_i^{3,+}$, the number of the degrees of freedom is

$$\text{dof}_3 = \mathcal{O}\big(10\cdot(4\frac{H}{h_2})^2\big),$$

where the number 10 indicates that each inner node in $\omega_i^{3,+}$ is equipped with 10 basis functions. The number of the sub-domains is

$$\#\text{ of sub-domains} = \mathcal{O}(1/H^2).$$

Hence, the computational cost at the level 3 is

$$\frac{1}{H^2}\mathcal{O}\big(10\cdot(\mathrm{dof}_3)^2\big)=\mathcal{O}\big(10^3\cdot 4^4\cdot\frac{H^2}{h_2^4}\big)$$

flops. Totally, the cost of the there-level GMsFEM is

$$TC3=\mathcal{O}\big(10\cdot 4^4\cdot\frac{h_2^2}{h^4}\big)+\mathcal{O}\big(10^3\cdot 4^4\cdot\frac{H^2}{h_2^4}\big)=\mathcal{O}\big(10\cdot 4^4\cdot\frac{H+10^2h}{h^3}\big)$$

flops. Here, we have used the assumption that $h_2/h=H/h_2$.

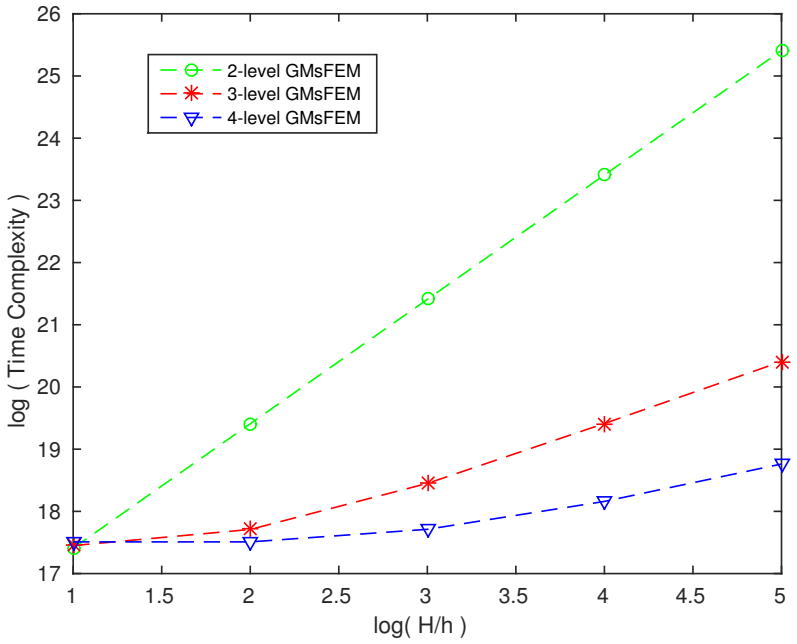

Figure IV.6: Time complexity for 2-level, 3-level, and 4-level GMsFEM. The finest scale h $= 10^{-6}$. x-label: log value of H/h; y-label: log value of the time complexity.

Now, we compare the costs for the two-level case and the three-level case. We

have

$$\begin{aligned}\frac{TC3}{TC2} &\approx \frac{10\cdot 4^4\cdot\frac{H+10^2h}{h^3}}{10\cdot 4^4\cdot\frac{H^2}{h^4}}\\ &= \frac{h(H+10^2h)}{H^2}\\ &\leq \frac{1}{2}\cdot\frac{h}{H} \qquad \text{(when } H\geq 10^2h\text{)}. \end{aligned} \tag{IV.21}$$

The above result implies that when the coarsest mesh is coarse enough, $H \geq 10^2 h$, the three-level GMsFEM takes a huge advantage over the standard two-level GMsFEM with respect to the cost. In Figure IV.6, we depict the time complexities for several multi-level GMsFEMs, where the finest scale is fixed to be $h = 1/10^6$ and the coarsest scale $H = 10^n h$. We observe that the time complexity drops significantly when one more level is added.

IV.5 Convergence analysis

In this section, we provide a convergence proof of the GMsFEM using the multi-level method. Throughout this section, we define $||\cdot||_D$ as the weighted energy norm on the domain D, i.e., $\|u\|_D = \left(\int_D \kappa\nabla u\cdot\nabla u\right)^{1/2}$. We use the notation $\alpha \preceq \beta$ when $\alpha \leq c\beta$, where the constant c is independent of the level and the spatial variation. we define χ_i^l and $\chi_i^{l,+}$ as partition of unity functions that are subordinated to ω_i^l and $\omega_i^{l,+}$, respectively. In particular, we can simply choose standard bilinear basis functions for a rectangular partition as χ_i^l and $\chi_i^{l,+}$. The size of $\omega_i^{l,+}$ is limited by the requirement

$$|\nabla\chi_i^l|^2 \preceq |\nabla\chi_i^{l,+}|^2. \tag{IV.22}$$

Using the triangle inequality, we know that

$$||u-u_L||_\Omega \leq ||u-u_{L-1}||_\Omega + ||u_{L-1}-u_L||_\Omega. \tag{IV.23}$$

Now, let us estimate $||u_{L-1} - u_L||_\Omega$.

For any $2 \leq l \leq L$, we define two interpolations $I^{\omega_i^l}$ and $I^{\omega_i^{l,+}}$ that will be chosen. We denote $\hat{u}_l$ as the multiscale solution at level l that is computed in the full snapshot space V_{snap}^l. Because the local snapshot space $V_{\text{snap},i}^l$ consists of the whole basis functions and the local snapshot space is constructed on $\omega_i^{l,+}$, we have $I^{\omega_i^{l,+}} \hat{u}_l = I^{\omega_i^l} \hat{u}_l$ in ω_i^l.

We borrow $\hat{u}_l$ and apply the triangle inequality, then

$$||u_{l-1} - u_l||_\Omega \leq \underbrace{||u_{l-1} - \hat{u}_l||_\Omega}_{\text{I}} + \underbrace{||\hat{u}_l - u_l||_\Omega}_{\text{II}}. \tag{IV.24}$$

Term I.

Applying the triangle inequality, we have

$$\begin{aligned} ||u_{l-1} - \hat{u}_l||_\Omega &\leq ||u_{l-1} - u||_\Omega + ||\hat{u}_l - u||_\Omega \\ &\preceq ||u_{l-1} - u||_\Omega \end{aligned} \tag{IV.25}$$

The inequality (IV.25) is easily induced by the fact that $\hat{u}_l$ is computed in the space $V_{\text{off}}^{l-1} \cup V_{\text{snap}}^{l-1,+}$ which implies that $||\hat{u}_l - u||_\Omega \preceq ||u_{l-1} - u||_\Omega$.

Term II.

Next, we derive a bound for the second term on the right hand size of the above inequality. Using the definition of $I^{\omega_i^l}$, we have

$$\begin{aligned} ||\hat{u}_l - u_l||_\Omega^2 &\preceq \sum_i ||\chi_i^l(\hat{u}_l - u_l)||_{\omega_i^l}^2 \\ &\preceq \sum_i \int_{\omega_i^l} \kappa |\chi_i^l|^2 |\nabla(\hat{u}_l - u_l)|^2 + \sum_i \int_{\omega_i^l} \kappa |\nabla \chi_i^l|^2 |\hat{u}_l - u_l|^2 \end{aligned} \tag{IV.26}$$

Let $-\text{div}(\kappa \nabla(\hat{u}_l - u_l)) = g(x)$ in ω_i^l. Multiplying both sides of this equation by

$|\chi_i^l|^2(\hat{u}_l - u_l)$, integrating by parts and rearranging the terms, we get

$$\begin{aligned} & \int_{\omega_i^l} \kappa|\chi_i^l|^2|\nabla(\hat{u}_l - u_l)|^2 \\ \leq \; & \frac{1}{c}\int_{\omega_i^l} \kappa|\nabla\chi_i^l|^2|\hat{u}_l - u_l|^2 + c\int_{\omega_i^l} \kappa|\chi_i^l|^2|\nabla(\hat{u}_l - u_l)|^2 + |\int_{\omega_i^l} g|\chi_i^l|^2|(\hat{u}_l - u_l)|, \end{aligned}$$

where the parameter $c < 1$ is independent of the level and the spatial variation. Rearranging the terms in above inequality, we have

$$\int_{\omega_i^l} \kappa|\chi_i^l|^2|\nabla(\hat{u}_l - u_l)|^2 \preceq \int_{\omega_i^l} \kappa|\nabla\chi_i^l|^2|\hat{u}_l - u_l|^2 + |\int_{\omega_i^l} g|\chi_i^l|^2(\hat{u}_l - u_l)|. \tag{IV.27}$$

From (IV.26) and (IV.27), we have

$$||\hat{u}_l - u_l||_\Omega^2 \preceq \sum_i \int_{\omega_i^l} \kappa|\nabla\chi_i^l|^2|\hat{u}_l - u_l|^2 + \sum_i |\int_{\omega_i^l} g|\chi_i^l|^2(\hat{u}_l - u_l)|. \tag{IV.28}$$

Note that the second term on the right hand side of the above inequality has the property

$$\begin{aligned} |\int_{\omega_i^l} g|\chi_i^l|^2(\hat{u}_l - u_l)| \; &\preceq \; |\int_{\omega_i^l} g(\hat{u}_l - u_l)| \\ &\preceq \; \int_{\omega_i^l} g\Big(\kappa|\nabla\chi_i^l|^2\Big)^{-1/2}\Big(\kappa^{1/2}|\nabla\chi_i^l|(\hat{u}_l - u_l)\Big) \\ &\preceq \; \int_{\omega_i^l} g^2\Big(\kappa|\nabla\chi_i^l|^2\Big)^{-1} + \int_{\omega_i^l} \kappa|\nabla\chi_i^l|^2|\hat{u}_l - u_l|^2. \end{aligned} \tag{IV.29}$$

With the assumption that $g \preceq 1$, we can show that $\int_{\omega_i^l} g^2\Big(\kappa|\nabla\chi_i^l|^2\Big)^{-1} \preceq h_l^2$. Combining this with (IV.28) and (IV.29), we obtain

$$||\hat{u}_l - u_l||_\Omega^2 \preceq \sum_i \int_{\omega_i^l} \kappa|\nabla\chi_i^l|^2|\hat{u}_l - u_l|^2 + h_l^2. \tag{IV.30}$$

Now we define $I^{\omega_i^{l,+}}\hat{u}_l$ and $I^{\omega_i^l}\hat{u}_l$ by choosing the dominant modes from eigenvalue problems (IV.13) and (IV.15), respectively. That is,

$$\int_{\omega_i^{l,+}} \kappa|\nabla\chi_i^{l,+}|^2|(\hat{u}_l - I^{\omega_i^{l,+}}\hat{u}_l)|^2 \preceq \frac{1}{\lambda_{i,s_i^l}^{l,+}}\int_{\omega_i^{l,+}} \kappa|\nabla(\hat{u}_l - I^{\omega_i^{l,+}}\hat{u}_l)|^2 \preceq \frac{1}{\lambda_{i,s_i^l}^{l,+}}\int_{\omega_i^{l,+}} \kappa|\nabla\hat{u}_l|^2, \tag{IV.31}$$

$$\int_{\omega_i^{l}} \kappa|\nabla\chi_i^{l}|^2|(\hat{u}_l - I^{\omega_i^{l}}\hat{u}_l)|^2 \preceq \frac{1}{\lambda_{i,s_i^l}^{l}}\int_{\omega_i^{l}} \kappa|\nabla(\hat{u}_l - I^{\omega_i^{l}}\hat{u}_l)|^2 \preceq \frac{1}{\lambda_{i,s_i^l}^{l}}\int_{\omega_i^{l}} \kappa|\nabla\hat{u}_l|^2. \tag{IV.32}$$

Here $\lambda_{i,s_i^l}^l$ is the s_i^l-th smallest eigenvalue of the corresponding eigenvalue problem. Note also that the $\lambda_{i,s_i^l}^l$-th eigenvector is the first one that is not selected for the dominant modes. We define

$$u_l = I^{\omega_i^{l,+}}\hat{u}_l + I^{\omega_i^l}(\hat{u}_l - I^{\omega_i^{l,+}}\hat{u}_l).$$

Using the inequality (25) in [29], we have

$$\sum_i \int_{\omega_i^l} \kappa|\nabla\chi_i^l|^2|\hat{u}_l - u_l|^2 \preceq \frac{1}{\Lambda_*^l}\frac{1}{\Lambda_*^{l,+}}\int_\Omega \kappa|\nabla\hat{u}_l|^2, \tag{IV.33}$$

where $\Lambda_*^l = \min_i \lambda_{i,s_i^l}^l$ and $\Lambda_*^{l,+} = \min_i \lambda_{i,s_i^l}^{l,+}$. Hence, if Λ_*^l and $\Lambda_*^{l,+}$ are chosen sufficiently large of the order $\mathcal{O}(1/h_l)$, we have the following estimate for (IV.30)

$$||\hat{u}_l - u_l||_\Omega^2 \preceq h_l^2||\hat{u}_l||_\Omega^2 + h_l^2. \tag{IV.34}$$

Therefore, with (IV.25) and (IV.34), we have an estimate for (IV.24)

$$||u_{l-1} - u_l||_\Omega \preceq ||u_{l-1} - u||_\Omega + h_l(||\hat{u}_l||_\Omega + 1) \preceq ||u_{l-1} - u||_\Omega + h_l(||u_l||_\Omega + 1). \tag{IV.35}$$

In particular,

$$||u_{L-1} - u_L||_\Omega \preceq ||u_{L-1} - u||_\Omega + h_L(||u_L||_\Omega + 1). \tag{IV.36}$$

Hence, the inequality (IV.23) follows

$$||u - u_L||_\Omega \preceq ||u - u_{L-1}||_\Omega + h_L(||u_L||_\Omega + 1) \tag{IV.37}$$

We are aware that when $L = 2$,

$$||u - u_2||_\Omega \ \preceq \ h_2(||u||_\Omega + 1). \tag{IV.38}$$

By the induction and the fact that $h_1 < h_2 < \cdots < h_L$, we obtain the convergence rate for the multilevel GMsFEM solution

$$||u - u_L||_\Omega \preceq h_L(||u_L||_\Omega + 1) \preceq h_L(||u||_\Omega + 1). \tag{IV.39}$$

IV.6 Concluding remarks

In this chapter, we present a multilevel method for computing coarse basis functions hierarchically in the GMsFEM framework. Our objective is to approximate snapshot vectors in a multilevel fashion. This work differs from previous findings [31, 32, 53], where the authors work with special snapshot vectors. In our construction, at each level, we compute the snapshot space and the offline space by solving a set of local problems. The computation of snapshot functions of current level is based on the snapshot space and the offline space of the previous level only. We also develop an innovative algorithm to create boundary basis functions related to the local problems. Such algorithm can avoid tremendous expensive computation and

offer a speedup in constructing coarse solution spaces. Some convergence analysis is presented. Both numerical experiments and computational time complexity analysis are provided to support our proposed approach.

V MULTISCALE SIMULATIONS OF FLOW AND TRANSPORT USING THE GENERALIZED MULTISCALE FINITE ELEMENT METHOD

V.1 Introduction

In this chapter, we consider a multiscale method for a coupled flow and transport system, where the flow equation for the pressure field is described by a steady state elliptic equation (derived by Darcy law) and the transport equation for the concentration field is described by a convection-dominated parabolic equation [17].

Our approach derives its foundation from rigorous methods developed recently [2, 4, 7, 10, 11, 12, 14, 15, 18, 19, 37, 43, 44, 45]. In these approaches, multiscale basis functions are computed and used to solve flow equations. The main contributions of this chapter are (1) to use multiscale basis functions for both flow and transport equations and (2) a design of a novel mixed multiscale methods for convection-dominated transport equation within the context of the GMsFEM. In our proposed approach, we use a mixed formulation for both the flow and the transport equations. The use of a mixed formulation is important for the transport equation as it helps with the stabilization of it. In particular, by adding more flux basis functions, we can achieve a better stability. In the mixed formulation for a coupled system, we first define snapshot spaces for the pressure and the concentration. The snapshot space represents the solution space in each coarse region and provides a mass conservative approach. In the snapshot space, we perform a local spectral decomposition to identify multiscale basis functions. The functions corresponding to dominant modes are used to construct coarse spaces. In particular, we use only a few degrees of freedom in each coarse region. For the test functions for the convection-dominated transport, we use the solutions of adjoint problem. As a result, we have a full coarse-

grid approximation for the coupled flow and transport system.

My contributions can be summarized as follows.

- The development of Generalized Multiscale Finite Element Method for a mixed formulation of the convection-diffusion equation using different test and trial spaces, giving better stabilization.

- The development and implementation of a mass conservative mixed GMsFEM for the coupled flow and transport equations.

We consider several numerical examples by considering three different hydraulic conductivity fields. In our numerical examples, we use a relatively coarse grid with the coarsening factor of 10 or 5. We study the numerical errors in the concentration field and depict concentration profiles. Our numerical results show that the use of only one basis function per coarse region (which is similar to numerical upscaling of hydraulic conductivity) does not produce an accurate solution, while if we use 3 or more basis functions, we can obtain an accurate approximation of the solution. All numerical results show that our fully coarse-grid model for the coupled flow and transport equations can accurately predict the solution using only a few degrees of freedom in each coarse region.

The rest of this chapter is organized as follows. In Section V.2, we present preliminaries and describe coarse and fine grids as well as a mixed formulation. Section V.3 is devoted to the construction of multiscale basis functions. Numerical results for three different hydraulic conductivity fields are presented in Section V.4. Finally, concluding remarks are given in Section V.5.

V.2 Preliminaries and notations

We consider a coupled flow and transport system that arises in many hydrological applications

$$\begin{aligned} \frac{\partial c}{\partial t} + v \cdot \nabla c - D\Delta c &= f_c \quad && \text{in } \Omega \times (0,T), \\ v + \kappa \nabla p &= 0 && \text{in } \Omega, \\ \nabla \cdot v &= f_q && \text{in } \Omega. \end{aligned} \tag{V.1}$$

Here Ω is the computational domain, $T > 0$ is a fixed time, κ is a hydraulic conductivity, c is the concentration, p is the pressure, D is a constant diffusivity of the medium, and f_c, f_q are source terms. The equations are subject to the boundary conditions $c(x,t) = 0$ on $\partial\Omega \times [0,T]$, $p(x) = g$ on $\partial\Omega$ and the initial condition $c(x,0) = 0$ in Ω. In order to have a mass conservation, we re-write the system in a mixed formulation

$$\begin{aligned} \frac{\partial c}{\partial t} + \nabla \cdot q &= f_c + c f_q \quad && \text{in } \Omega \times (0,T), \\ q + D\nabla c - vc &= 0 && \text{in } \Omega \times (0,T), \\ v + \kappa \nabla p &= 0 && \text{in } \Omega, \\ \nabla \cdot v &= f_q && \text{in } \Omega. \end{aligned} \tag{V.2}$$

Here q is an auxiliary variable, we call it flux. It is well known that the Galerkin method inherits the stability of the continuous problem and it yields to spurious oscillation when the convection coefficient is larger than the diffusive one ($v \gg D$). The mixed finite element methods can be used to achieve a mass conservation. In this chapter, we aim to construct multiscale basis functions for the flux q and the velocity v. As for the concentration c and the pressure p, we choose piecewise constant functions for the approximation.

Next, we introduce the discrete form of the problem (V.2). We first comment on some notations of the coarse and the fine mesh. The coarse grid configuration differs from those introduced in previous chapters because of a mixed formulation. We assume that Ω is partitioned in the usual way into a union of rectangles (in 2-D) or hexadedrals (in 3-D) denoted by $\mathcal{T}^H$, where H is the coarse mesh size. The fine mesh is obtained by splitting each coarse block in $\mathcal{T}^H$ into a connected union of fine-grid blocks, and we denote it by $\mathcal{T}^h$ with mesh size h, $h < H$. In addition, we denote by $\mathcal{E}^H$ the set of all edges/faces of elements in $\mathcal{T}^H$, i.e., $\mathcal{E}^H = \{E_i : 1 \leq i \leq N_e\}$, where N_e is the number of coarse edges/faces. Note that each $E_i \in \mathcal{E}^H$ is the union of some fine-grid edges/faces. That is, $E_i = \{e_j : e_j \text{ is on } E_i\}$, where e_j are the fine-grid edges/faces lying on E_i. We also define the coarse neighborhood of the edge/face E_i by

$$\omega_i = \{K \in \mathcal{T}^H : \partial K \cap E_i \neq \phi\}. \tag{V.3}$$

See Figure V.1 for an illustration of a coarse neighborhood associated with one coarse edge, where the coarse mesh and the fine mesh are represented by black lines and gray lines, respectively.

Next, we define the coarse trial spaces for q, v, c, and p. The concentration c and the pressure p are approximated in the space of piecewise constant functions with respect to the coarse grid $\mathcal{T}^H$. We denote this space by Q_H, and

$$Q_H = \{\psi : \psi|_{K_i} \in \mathcal{P}_0(K_i) \text{ for all } K_i \in \mathcal{T}^H\}. \tag{V.4}$$

As for the flux q and the velocity v, the basis functions are associated with coarse edges and are supported in the corresponding coarse neighborhoods. In particular, to obtain the basis functions for a coarse edge E_i, we will solve a local problem in

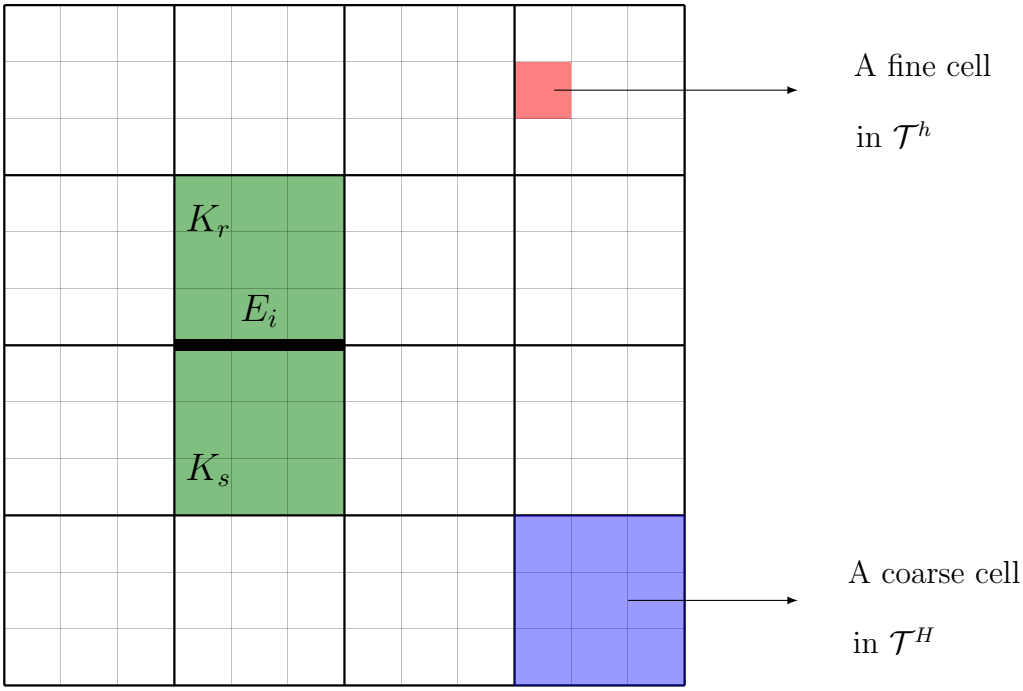

Figure V.1: An illustration of a coarse neighborhood ω_i (in green) corresponding to the coarse edge E_i.

the coarse neighborhood ω_i. Let Φ_i^q and Φ_i^v be the set of multiscale basis functions for q and v with respect to E_i, respectively. Then, we define the multiscale solution space for q and v as

$$V_H^q = \bigcup_{E_i} \Phi_i^q \quad \text{and} \quad V_H^v = \bigcup_{E_i} \Phi_i^v. \tag{V.5}$$

Furthermore, we discretize the time interval $[0, T]$ uniformly by the points

$$t^n = n\tau, \quad n = 0, 1, \cdots, N,$$

where τ is the time step and $N = T/\tau$. Using the above spaces, the GMsFEM approximation of (V.2) can be given as follows. For all $n \geq 1$, find $(c_H^n, q_H^n, p_H, v_H) \in$

$Q_H \times V_H^q \times Q_H \times V_H^v$, such that

$$\begin{aligned}
\int_\Omega \frac{c_H^n - c_H^{n-1}}{\tau}\tilde{c} + \int_\Omega (\nabla \cdot q_H^{n-\theta})\tilde{c} &= \int_\Omega (f_c^{n-\theta} + c_H^{n-\theta} f_q)\tilde{c} && \text{for } \forall \tilde{c} \in Q_H, \\
\int_\Omega \frac{1}{D} q_H^{n-\theta} \cdot \tilde{q} &= \int_\Omega (\nabla \cdot \tilde{q} + \frac{v_H}{D} \cdot \tilde{q}) c_H^{n-\theta} && \text{for } \forall \tilde{q} \in W_H^q, \\
\int_\Omega \frac{1}{\kappa} v_H \cdot \tilde{v} &= \int_\Omega (\nabla \cdot \tilde{v}) p_H && \text{for } \forall \tilde{v} \in V_H^v, \\
\int_\Omega (\nabla \cdot v_H)\tilde{p} &= \int_\Omega f_q \tilde{p} && \text{for } \forall \tilde{p} \in Q_H,
\end{aligned} \tag{V.6}$$

subject to the boundary condition $p_H = g$. Here, we let $z^{n-\theta} = \theta z^{n-1} + (1-\theta) z^n$, where $z = c_H$ or q_H. For $\theta = 0, 1/2$ and 1, we get the Backward Euler, Crank-Nicolson and Forward Euler Methods respectively. Note that W_H^q is the testing space for q_H^n. We emphasize here that in general, $W_H^q \neq V_H^q$, which allows better stability. The construction of V_H^q, V_H^v, and W_H^q will be discussed in the next section.

In addition, to get the fine-scale solution, we use the standard lowest-order Raviart-Thomas space $Q_h \times V_h^q \times Q_h \times V_h^v$ for the approximation of (V.2) on the fine grid $\mathcal{T}^h$. The fine-scale solution (c_h, q_h) will be considered as a reference solution for the comparison with the multiscale solution (c_H, q_H).

V.3 Generalized multiscale finite element methods

In this section, we will discuss the construction of the vector solution spaces V_H^q, V_H^v, and the testing space W_H^q. Note that solving q_H in (V.6) requires v_H. Therefore, we will first compute v_H using the last two equations of (V.6).

We recall that the objective of the GMsFEM is (1) to construct the snapshot space obtained by solutions of local problems with all possible boundary conditions, which are resolvable by the fine-grid; (2) to identify a subspace of the snapshot space by selecting dominant modes via some local spectral decompositions. The resulting reduced-dimensional space, called the offline space, will be used to approximate the

multiscale solution. We remark that for parameter dependent problems, one needs to construct an online space using the offline space and an appropriate spectral problem.

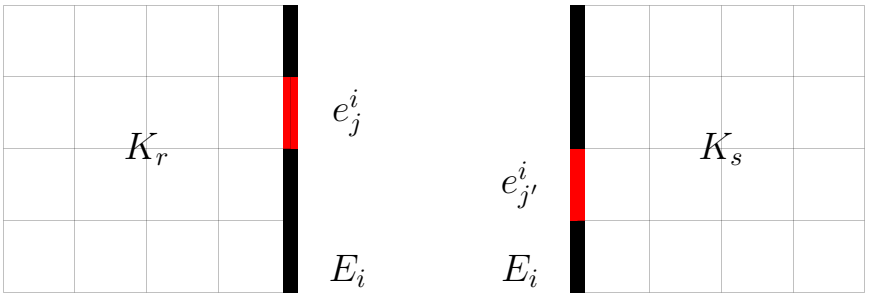

Figure V.2: Neighboring coarse cells K_r and K_s corresponding to the coarse-grid edge E_i. The fine-grid edge e_j^i and $e_{j'}^i$ are in red.

V.3.1 Multiscale solution space V_H^v

We form the multiscale solution space V_H^v for v_H. In order to build V_H^v, we first construct the snapshot space, denoted by V_{snap}^v. For each coarse-grid edge $E_i \in \mathcal{E}^H$, a local problem is defined on each of its neighboring coarse cells. Because the snapshot space is supposed to capture the multiscale information within this local domain, the corresponding boundary conditions of the local problem should cover all possibilities. Formally, the local problem is defined as: for each $E_i \in \mathcal{E}^H$, on its neighboring coarse cell $K = K_r$ or K_s (see Figure V.2), find $(p_j^i, \psi_{v,j}^i) \in Q_h \times V_h^v$, such that

$$\begin{aligned} \psi_{v,j}^i + \kappa \nabla p_j^i &= 0 \qquad \text{in } K, \\ \nabla \cdot \psi_{v,j}^i &= \alpha_j^i \qquad \text{in } K, \\ \psi_{v,j}^i \cdot n &= 0 \qquad \text{on } \partial K \backslash E_i, \\ \psi_{v,j}^i \cdot n &= \delta_j^i \qquad \text{on } E_i. \end{aligned} \tag{V.7}$$

For convenience, we use the same notations as the solution to denote local snapshot fields. Here α_j^i is a constant defined on K, n is a fixed unit-normal vector on ∂K, and $\delta_j^i(x)$ is defined on E_i with respect to the fine-grid edges. Note that $E_i = \{e_j^i : e_j^i \text{ in } E_i\}$. We require δ_j^i has value 1 on e_j^i and 0 on the other fine-grid edges, $1 \le j \le J_i$, where J_i is the number of the fine-grid edges on E_i. That is,

$$\delta_j^i = \begin{cases} 1, & \text{on } e_j^i, \\ 0, & \text{on the other fine-grid edges.} \end{cases}$$

Note that the constant α_j^i in (V.7) is chosen so that the compatibility condition $\int_K \alpha_j^i = (\pm) \int_{E_i} \delta_j^i$ is satisfied, for $K = K_r$ or K_s. The above local problem (V.7) can be solved numerically on the underlying fine grid of K by the lowest-order Raviart-Thomas element method.

After solving the local problems (on K_r and K_s) with respect to E_i, a local snapshot $V_{\text{snap}}^{v,i}$ is generated by the solutions of (V.7). That is

$$V_{\text{snap}}^{v,i} = \text{span}\{\psi_{v,j}^i : 1 \le j \le J_i\}.$$

Then, the snapshot space V_{snap}^v is formed as

$$V_{\text{snap}}^v = \bigcup_{E_i} V_{\text{snap}}^{v,i} = \text{span}\{\psi_{v,j}^i : 1 \le j \le J_i, 1 \le i \le N_e\}. \tag{V.8}$$

We re-numerate the snapshot functions by a single index to create the snapshot matrix

$$R_{\text{snap}}^v = \left[\psi_1^v, \psi_2^v, \cdots, \psi_{L_{\text{snap}}}^v\right],$$

where $L_{\text{snap}} = \sum_{i=1}^{N_e} J_i$ is the dimension of the snapshot space V_{snap}^v. Note that the

matrix R^v_{snap} maps from the coarse space to the fine space.

The next step is to construct the offline space V^v_{off} for v_H. For a coarse-grid edge E_i, we define the following eigenvalue problem in $V^{v,i}_{\text{snap}}$:

$$A^{\text{off}}_v \Psi^v_k = \lambda_k M^{\text{off}}_v \Psi^v_k, \tag{V.9}$$

where

$$A^{\text{off}}_v = [a_{st}] = \int_{E_i} (\psi^i_{v,s} \cdot n)(\psi^i_{v,t} \cdot n),$$

and

$$M^{\text{off}}_v = [m_{st}] = \int_{\omega_i} \frac{1}{\kappa} \psi^i_{v,s} \cdot \psi^i_{v,t}.$$

The eigenvalue problem (V.9) will produce a set of eigenvectors for generating the local offline space $V^{v,i}_{\text{off}}$ by first selecting L^i_{off} eigenvectors corresponding (as before) to the smallest L^i_{off} eigenvalues, and then computing the element $\phi^i_{v,k} = \sum_{j=1}^{J_i} \Psi^v_{kj} \psi^i_{v,j}$ for $k = 1, 2, \cdots, L^i_{\text{off}}$, where Ψ^v_{kj} is the j-th component of Ψ^v_k. Then the local offline space with respect to E_i is formed as

$$V^{v,i}_{\text{off}} = \text{span}\{\phi^i_{v,k} : 1 \leq k \leq L^i_{\text{off}}\}.$$

and the offline space V^v_{off} is formed as

$$V^v_{\text{off}} = \bigcup_{E_i} V^{v,i}_{\text{off}} = \text{span}\{\phi^i_{v,k} : 1 \leq k \leq L^i_{\text{off}},\ 1 \leq i \leq N_e\}. \tag{V.10}$$

We re-numerate the basis functions by a single index to create the offline matrix

$$R^v_{\text{off}} = \left[\phi^v_1, \phi^v_2, \cdots, \phi^v_{L_{\text{off}}}\right],$$

where $L_{\text{off}} = \sum_{i=1}^{N_e} L_{\text{off}}^i$ is the dimension of the offline space V_{off}^v.

We take the multiscale solution space as

$$V_H^v = V_{\text{off}}^v.$$

Then v_H is approximated by solving the problem as follows. We seek $(p_H, v_H) \in Q_H \times V_H^v$ such that

$$\begin{aligned} \int_\Omega \frac{1}{\kappa} v_H \cdot \tilde{v} &= \int_\Omega (\nabla \cdot \tilde{v}) p_H \qquad \text{for } \forall \tilde{v} \in V_H^v, \\ \int_\Omega (\nabla \cdot v_H) \tilde{q} &= \int_\Omega f_q \tilde{q} \qquad \text{for } \forall \tilde{q} \in Q_H, \end{aligned} \tag{V.11}$$

subject to the boundary condition $p_H = g$.

Remark V.3.1. *The design of a "good" eigenvalue problem is a key ingredient of the GMsFEM. It plays a critical role in reducing the dimension of the coarse solution space. After applying such eigenvalue problem, the few dominant modes should sufficiently capture the multiscale behavior of the multiscale solution up to some certain extent.*

Remark V.3.2. *Generally, the offline space should contain a constant basis function. Therefore, the local snapshot space $V_{snap}^{v,i}$, as a solution space of the eigenvalue problem (V.9), can be decomposed into $V_1^{v,i} \bigoplus V_2^{v,i}$, where $V_1^{v,i} = \{(1, 1, \cdots, 1)\}$ and $V_2^{v,i} = \{\psi : \int_{E_i} \psi \cdot n_i = 0, \psi \in V_{snap}^{v,i}\}$. We put $(1, 1, \cdots, 1) \in V_1^{v,i}$ as the first basis function of the offline space, and identify the other dominant modes in the space $V_2^{v,i}$.*

V.3.2 Multiscale solution space V_H^q

We construct the solution space V_H^q and the testing space W_H^q for q_H. They follow a similar procedure to the one for v_H. In order to build V_H^q, the snapshot space V_{snap}^q

is to be constructed. We define a local problem corresponding to each coarse-grid edge $E_i \in \mathcal{E}^H$ as follows. We seek $(c_j^i, \psi_{q,j}^i) \in Q_h \times V_h^q$, such that

$$\begin{aligned} \psi_{q,j}^i + D\nabla c_j^i - v_H c_j^i &= 0 \qquad \text{in } K, \\ \nabla \cdot \psi_{q,j}^i &= \alpha_j^i \qquad \text{in } K, \\ \psi_{q,j}^i \cdot n &= 0 \qquad \text{on } \partial K \backslash E_i, \\ \psi_{q,j}^i \cdot n &= \delta_j^i \qquad \text{on } E_i, \end{aligned} \tag{V.12}$$

where $K = K_r$ or K_s depicted in Figure V.2. The local snapshot space $V_{\text{snap}}^{q,i}$, the snapshot space V_{snap}^q, and the snapshot matrix R_{snap}^q are formed as

$$V_{\text{snap}}^{q,i} = \text{span}\{\psi_{q,j}^i : 1 \le j \le J_i\},$$

$$V_{\text{snap}}^q = \bigcup_{E_i} V_{\text{snap}}^{q,i} = \text{span}\{\psi_{q,j}^i : 1 \le j \le J_i,\ 1 \le i \le N_e\}. \tag{V.13}$$

$$R_{\text{snap}}^q = \left[\psi_1^q, \psi_2^q, \cdots, \psi_{L_{\text{snap}}}^q\right],$$

respectively.

To construct the testing space W_H^q, a snapshot space W_{snap}^q is also needed. We solve the adjoint problem of (V.12)

$$\begin{aligned} w_{q,j}^i - D\nabla p_j^i &= 0 \qquad \text{in } K, \\ \nabla \cdot w_{q,j}^i + \frac{1}{D} v_H \cdot w_{q,j}^i &= \frac{1}{D}\alpha_j^i \qquad \text{in } K, \\ w_{q,j}^i \cdot n &= 0 \qquad \text{on } K \backslash E_i, \\ w_{q,j}^i \cdot n &= \delta_j^i \qquad \text{on } E_i. \end{aligned} \tag{V.14}$$

Then the snapshot space W_{snap}^q is formed by the snapshot functions $\omega_{q,j}^i$ for all $E_i \in$

$\mathcal{T}^H$.

The local offline space $V_{\text{off}}^{q,i}$ for u_H is obtained by solving the following eigenvalue problem in $V_{\text{snap}}^{q,i}$:

$$A_q^{\text{off}}\Psi_k^q = \lambda_k M_q^{\text{off}}\Psi_k^q, \tag{V.15}$$

where

$$A_q^{\text{off}} = [a_{st}] = \int_{E_i} (\psi_{q,s}^i \cdot n)(\psi_{q,t}^i \cdot n),$$

and

$$M_q^{\text{off}} = [m_{st}] = \int_{\omega_i} \tilde{D}\psi_{q,s}^i \cdot \psi_{q,t}^i.$$

Here, we let $\tilde{D} = \frac{1+|v_H|}{D}$, where $|v_H|$ denotes the vector l^2 norm of v_H. Then the local offline space $V_{\text{off}}^{q,i}$, the offline space V_{off}^q, and the offline matrix R_{off}^q are formed as:

$$V_{\text{off}}^{q,i} = \text{span}\{\phi_{q,k}^i : 1 \le k \le L_{\text{off}}^i\},$$

$$V_{\text{off}}^q = \bigcup_{E_i} V_{\text{off}}^{q,i} = \text{span}\{\phi_{q,k}^i : 1 \le k \le L_{\text{off}}^i, 1 \le i \le N_e\}, \tag{V.16}$$

$$R_{\text{off}}^q = \left[\phi_1^q, \phi_2^q, \cdots, \phi_{L_{\text{off}}}^q\right],$$

respectively. Here $\phi_{q,k}^i = \sum_{j=1}^{J_i} \Psi_{kj}^q \psi_{q,j}^i$, $k = 1, 2, \cdots, L_{\text{off}}^i$, is the dominant mode in the space $V_{\text{snap}}^{q,i}$.

We let $V_H^q = V_{\text{off}}^q$ and define the testing space as

$$W_H^q = \{w \in W_{\text{snap}}^q : (w - q) \cdot n|_E = 0, \quad \text{for all } E \in \mathcal{E}^H, \quad \text{for some } q \in V_H^q\}, \tag{V.17}$$

where n is the unit-normal vector of the coarse-grid edge E. Now, we have the multiscale solution space V_H^q and the testing space W_H^q. The GMsFEM solution

(c_H, q_H) can be computed through (V.6).

Remark V.3.3. *We remark that the fine-scale velocity field is constructed and used in computing multiscale basis functions for the concentration. In future, we plan to study joint multiscale basis construction procedures, which can compute multiscale basis functions for the concentration without solving the velocity field. Because the concentration field is a nonlinear function of the velocity field, an online procedure for computing multiscale basis functions for the concentration will be employed.*

V.4 Numerical results

We present a representative set of numerical experiments that demonstrate the performance of the mixed GMsFEM for approximating the coupled flow and transport equations (V.2). The computational domain $\Omega = [0,1] \times [0,1]$. We consider two different permeability fields κ, as depicted in Figure V.3(a-b). The source term f_c to be used are plotted in Figure V.3(c-d), and f_q is chosen to be 0. In all experiments below, the fine grid $\mathcal{T}^h$ is fixed to be 200×200 uniform mesh, i.e., $h = 1/200$. The coarse grid consists of 20×20 uniform meshes, i.e., $H = 1/20$. As for the time discretization, the time step is chosen to be $\tau = 1 \times 10^{-4}$ and the Crank-Nicolson scheme is used. We denote $\overline{c_h}$ as the average value of c_h in each coarse cell, i.e., $\overline{c_h} = \frac{1}{|K|}\int_K c_h$, for every $K \in \mathcal{T}^H$. The relative numerical errors are measured in L^2 norm for the concentration.

In our numerical experiments, we approximate the velocity v_H and the flux q_H (at any time instant) in the offline space V_H^v and V_H^q in which each coarse edge is equipped with L^i_{off} basis functions. We choose at most $L^i_{\text{off}} = 2$ and compare concentration profiles with $L^i_{\text{off}} = 1$. Note that there are H/h basis functions associated with each coarse edge. We only select up to the two dominant modes per edge to form the offline space.

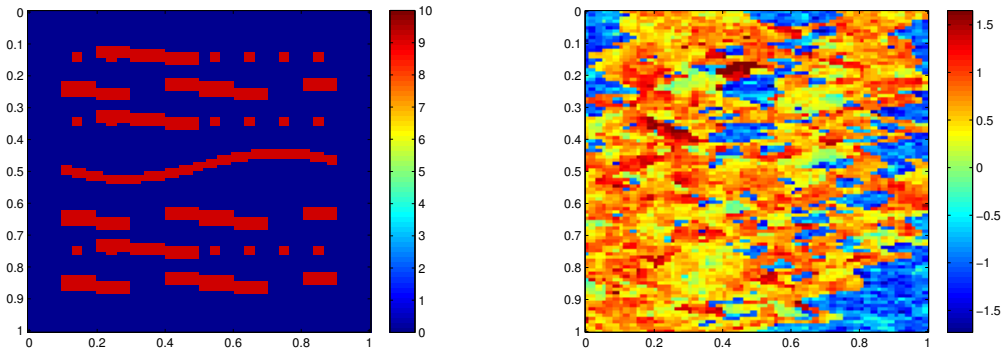

(a) κ_1 in $\log_{10}$ scale

(b) κ_2 in $\log_{10}$ scale

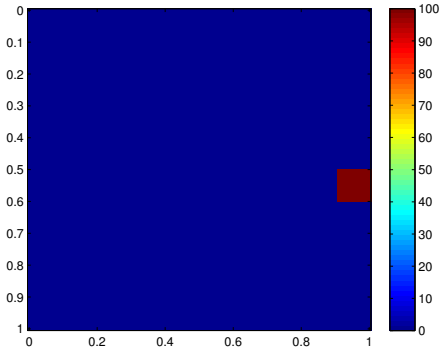

(c) f_1

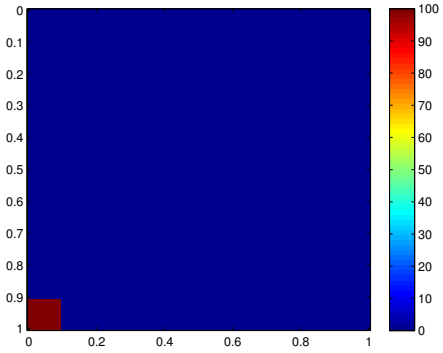

(d) f_2

Figure V.3: Two permeability fields (top) and two source terms (bottom).

The first experiment is for the problem (V.2), where the diffusivity $D = 1$, the source term $f_c = f_1$, the permeability field $\kappa = \kappa_1$, and the boundary condition $g = 7xy$. The boundary condition represents the flow from lower left corner to upper right corner. In Figure V.4, we depict the averaged fine-scale solutions and the GMsFEM solutions at the time $T = 0.015$, 0.04, and 0.1. We choose the averaged fine-scale solution since piecewise constant basis functions are used in the approximation of the concentration on a coarse grid. The averaged fine-scale solution is depicted on the top of Figure V.4. In the middle row, we depict the GMsFEM solution, where only one basis function is used for the approximation of the velocity and one basis

function is used for the approximation of the flux-concentration field. The L^2 errors in the concentration field are 21.22%, 30.16%, and 27.19% at $T = 0.015$, 0.04, and 0.1. At the bottom row of Figure V.4, we depict the concentrations computed using two basis functions for the velocity and two basis functions for the flux-concentration field. As we observe, the results look much better when two basis functions are used. For example, at $T = 0.1$, we can observe that the concentration profile is similar to the averaged fine-scale concetration profile. The L^2 errors in the concentration field are 8.1%, 11.1%, and 8.44% at $T = 0.015$, 0.04, and 0.1. Note that since we use 20×20 coarse grid and piecewise constant basis functions for the concentration, one expects a first order convergence with respect to the coarse mesh (i.e., about 5% error in our case).

In our second set of numerical examples, we consider the permeability $\kappa = \kappa_2$, a source term $f_c = f_2$, and a boundary condition $g = 8(x - y)$. We let the diffusivity to be $D = 1$. In this case, the problem becomes convection-dominated, where the coarse-grid Peclet number has a maximum value around 8.1. The numerical results are shown in Figure V.5, where the top row shows the averaged fine-scale concentration profiles, the middle row shows the GMsFEM solution with one velocity basis and one flux-concentration basis functions, and the bottow row shows the GMsFEM solution, which uses two velocity basis functions and two flux-concentration basis functions. In all numerical results, we use piecewise constant pressure and piecewise constant concentration basis functions, as mentioned earlier. Thus, for the concentration field, there is an irreducable error of order H (5% in our case). First, we study the numerical results using only one multiscale basis function (the middle row of Figure V.5). The L^2 errors in the concentration field are 77.6%, 82.53%, and 77.96% at $T = 0.01$, 0.02, and 0.1. We observe from the figure that the coarse space consisting one basis function per edge does not work well in capturing the averaged

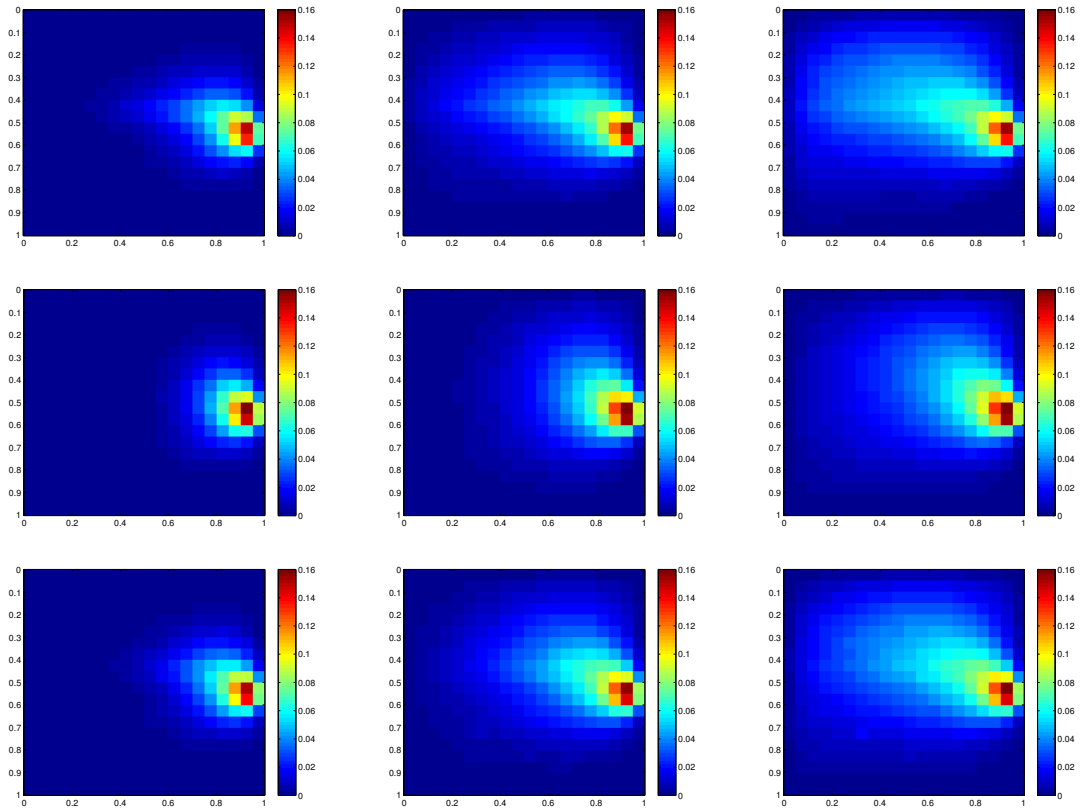

Figure V.4: First row: Fine-scale solutons $\overline{c_h}$. Second row: GMsFEM solutions c_H (one multiscale basis function per edge for both velocity and flux-concentration). Third row: GMsFEM solutions c_H (two multiscale basis function per edge for both velocity and flux-concentration). From left column to right column: $T = 0.015,\ 0.04,\ 0.1$. We use $\kappa = \kappa_1$, $f_c = f_1$, H=1/20.

fine-scale solution behavior. On the other hand, we observe a good agreement when two multiscale basis functions are used (the bottom row of Figure V.5). We observe that the main features of the concentration profile are captured. The L^2 errors in the concentration field are 14.9%, 18.24%, and 15.71% at $T = 0.01$, 0.02, and 0.1.

In our numerical simulations, we limit ourselves to piecewise constant (lowest order) concentration basis functions. This allows a low computational cost and avoid a design of more complex concentration basis functions, which can satisfy inf-sup con-

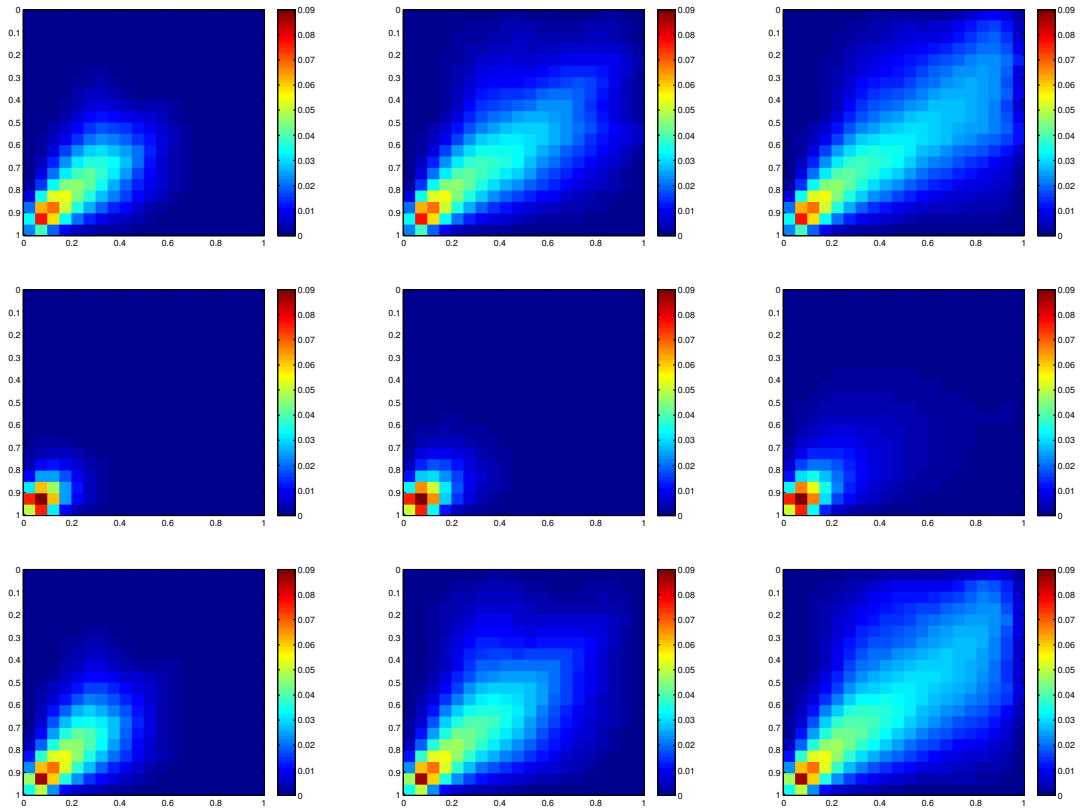

Figure V.5: First row: Fine-scale solutons $\overline{c_h}$. Second row: GMsFEM solutions c_H (one multiscale basis function per edge for both velocity and flux-concentration). Third row: GMsFEM solutions c_H (two multiscale basis function per edge for both velocity and flux-concentration). From left column to right column: $T = 0.01,\ 0.02,\ 0.1$. We use $\kappa = \kappa_2$, $f_c = f_2$, H=1/20.

ditions (see e.g., [13]). Since we use lowest order basis functions for the concentration, the accuracy is limited to $O(H)$. This is reasonable as in large-scale simulations (due to very detailed κ), the coarse grid sizes can be taken sufficiently small. In general, the numerical results shown above can be improved using more basis functions for the flux-concentration and designing multiscale basis functions for the concentration field. One of our main objectives is to show that the results with one basis function (which is similar to flow-based upscaling) can be substantially improved if one uses

more multiscale basis functions and we also provide a procedure for computing the multiscale basis functions and suitable global formulations.

V.5 Concluding remarks

In this chapter, we develop a Generalized Multiscale Finite Element Method (GMsFEM) for coupled flow and transport equations. The transport equation is convection dominated and we choose an appropriate test space to achieve a stability and improved numerical results. We study a mixed formulation for both flow and transport, which guarantees mass conservation. The multiscale spaces for the flux and the velocity fields are constructed by appropriately choosing the snapshot spaces and performing local spectral decompositions. The design of the local problem for generating the snapshot space is one of our novel contributions. From the numerical experiments, we observe that the mixed GMsFEM offers an accurate and efficient approach for treating high-contrast convection diffusion problem considered in this chapter.

VI CONCLUSIONS

In this dissertation, GMsFEMs for high-contrast and high-anisotropy problems are investigated. In Chapter II, we introduce the notion of material contrast and anisotropy. We describe the concept of coarse space and discuss the robust two-level domain decomposition preconditioners for highly anisotropic heterogeneous multiscale problems. We observe that, distinct from isotropic materials, anisotropic inclusions and channels bring an additional dimension to the coarse space. To obtain a reduced-dimensional coarse space, we construct two spectral coarse spaces, where standard bilinear basis functions and multiscale basis functions are employed as the partition of unity, respectively. Based on the numerical results, we see that the two spectral coarse spaces work well in reduction of the dimension and provide robust preconditioners in the sense that the width, angle, and number of anisotropic channels do not affect much the number of iterations. Furthermore, the spectral coarse space using multiscale basis functions, compared to the one using the blinear basis functions, has smaller dimension as the underlying physical properties become more complicated.

In Chapter III, we study a more general flow problem with high-contrast, high-anisotropy, and parameter-dependent coefficients. We describe the GMsFEM framework and investigate the application of the GMsFEM to this more general flow problem. Two types of snapshot spaces, harmonic and eigenvalue, are presented for building the multiscale coarse space. Note that our previous approach is limited and can not handle general snapshot spaces as we discussed in the chapter. To obtain a reduced-dimensional coarse space, we use a multiscale model reduction technique, which is based on localized spectral decompositions in the snapshot space. Several

bilinear forms associated to the eigenvalue problems are presented and the numerical experiments have shown that all problems work well for selecting the dominant eigenvectors. In particular, all cases allows us to flexibly choose a set of eigenvectors that offer a predictable error decline. In addition, when an oversampling technique is used in the harmonic computations and localized eigenvalue problems, we observe a faster convergence. Both parameter-independent and parameter-dependent cases are discussed. The supporting numerical examples show that the GMsFEM offers an accurate and efficient framework for treating high-contrast anisotropic problems considered in this chapter.

In Chapter IV, we present a multilevel method in the GMsFEM framework for hierarchically computing coarse basis functions. As the two-level GMsFEM, we attempt to construct the snapshot space for the later use of building multiscale coarse space. In this chapter, we develop an innovative algorithm to approximate snapshot vectors in a multilevel fashion. More precisely, on grids of each level, we compute the snapshot space by solving a set of local problems with harmonic extensions. For a given level, the snapshot functions are computed only based on the snapshot space and offline space of the previous level. This algorithm has the benefit of avoiding tremendous expensive fine-grid computation and offering a speed-up in constructing the multiscale coarse space. The use of oversampling techniques in the algorithm brings a faster convergence for the resulting coarse space. Both numerical experiments and computational time complexity analysis support our proposed approach.

In Chapter V, based on the GMsFEM, we develop a mixed GMsFEM for coupled flow and transport in heterogeneous porous media. The flow equation involves high-contrast coefficients and the transport equation is convection dominated. The convection-dominated flow equation is a challenging anisotropic problem, where the convection direction bring a high anisotropy to the problem. We study a mixed

formulation for both flow and transport and construct the multiscale coarse spaces for the flux and the velocity fields. We design (1) local problems for computing the snapshot spaces and (2) localized eigenvalue problems for performing local spectral decompositions. In addition, we choose an appropriate test space to achieve a stability and improve numerical accuracy. Numerical results show that with only a few basis functions per coarse block, we can achieve a good approximation. The mixed GMsFEM provides an accurate and efficient approach for treating high-contrast convection diffusion problem considered in this chapter.

REFERENCES

[1] J. E. Aarnes. On the use of a mixed multiscale finite element method for greater flexibility and increased speed or improved accuracy in reservoir simulation. *SIAM J. Multiscale Modeling and Simulation*, 2:421–439, 2004.

[2] J. E. Aarnes, S. Krogstad, and K.-A. Lie. A hierarchical multiscale method for two-phase flow based upon mixed finite elements and nonuniform grids. *SIAM J. Multiscale Modeling and Simulation*, 5(2):337–363, 2006.

[3] A. Abdulle and W. E. Finite difference heterogeneous multi-scale method for homogenization problems. *J. Comput. Phys.*, 191:18–39, 2003.

[4] T. Arbogast, G. Pencheva, M.F. Wheeler, and I. Yotov. A multiscale mortar mixed finite element method. *SIAM J. Multiscale Modeling and Simulation*, 6(1):319–346, 2007.

[5] S. C. Brenner and L. Ridgway Scott. *The mathematical theory of finite element methods. Third edition. Texts in Applied Mathematics*, 15. Springer, New York, 2008.

[6] V. Calo, Y. Efendiev and J. Galvis. A note on variational multiscale methods for high-contrast heterogeneous flows with rough source terms. *Advances in Water Resources*, 34(9):1177–1185, 2011.

[7] Ho Yuen Chan, Eric T Chung, and Yalchin Efendiev. Adaptive mixed gmsfem for flows in heterogeneous media. *arXiv preprint arXiv:1507.01659*, 2015.

[8] Y. Chen and L. Durlofsky. An ensemble level upscaling approach for efficient estimation of fine-scale production statistics using coarse-scale simulations. In

SPE Reservoir Simulation Symposium, number 106086-MS, Houston, Texas, U.S.A., 2 2007. Society of Petroleum Engineers.

[9] Y. Chen, L. Durlofsky, M. Gerritsen, and X. Wen. A coupled local-global upscaling approach for simulating flow in highly heterogeneous formations. *Advances in Water Resources*, 26:1041–1060, 2003.

[10] E. Chung and Y. Efendiev. Reduced-contrast approximations for high-contrast multiscale flow problems. *SIAM J. Multiscale Modeling and Simulation*, 8:1128–1153, 2010.

[11] E. Chung and W. Leung. A sub-grid structure enhanced discontinuous galerkin method for multiscale diffusion and convection-diffusion problems. *Comput. Phys*, 14:370–392, 2013.

[12] E. Chung, Y. Efendiev, and S. Fu. Generalized multiscale finite element method for elasticity equations. *GEM-International Journal on Geomathematics*, 5(2):225–254, 2014.

[13] E. Chung, Y. Efendiev, and C. S. Lee. Mixed generalized multiscale finite element methods and applications. *SIAM Multiscale Modeling and Simulation*, 13:338–366, 2015.

[14] E. Chung, Y. Efendiev, and W. Leung. An online generalized multiscale discontinuous galerkin method (gmsdgm) for flows in heterogeneous media. *arXiv preprint arXiv:1504.04417*, 2015.

[15] E. Chung, Y. Efendiev, and W. Leung. Residual-driven online generalized multiscale finite element methods. *arXiv preprint arXiv:1501.04565*, 2015.

[16] E. Chung, Y. Efendiev, and W. Leung. Generalized multiscale finite element methods for wave propagation in heterogeneous media. *arXiv preprint*

arXiv:1307.0123, 2013.

[17] Eric T. Chung, Yalchin Efendiev, Wing Tat Leung, and Jun Ren. Multiscale Simulations For Coupled Flow And Transport Using The Generalized Multiscale Finite Element Method. *Computation*, submitted, 2015.

[18] E. Chung, Y. Efendiev, G. Li, and M. Vasilyeva. Generalized multiscale finite element methods for problems in perforated heterogeneous domains. *Applicable Analysis*, to appear, 2015.

[19] E. Chung, Y. Efendiev, and G. Li. An adaptive GMsFEM for high-contrast flow problems. *Journal of Computational Physics*, 273:54–76, 2014.

[20] L. J. Durlofsky. Numerical calculation of equivalent grid block permeability tensors for heterogeneous porous media. *Water Resour. Res.*, 27:699–708, 1991.

[21] L. J. Durlofsky, Y. Efendiev, and V. Ginting. An adaptive local-global multiscale finite volume element method for two-phase flow. *Advances in Water Resources*, 30:576–588, 2007.

[22] L. J. Durlofsky and W. J. Milliken. Upscaling of geologic models for reservoir simulation. *Proceedings of the 19th Annual International Energy Agency Workshop and Symposium*, Carmel, Oct. 4-7 (1998).

[23] Y. Efendiev and J. Galvis. A domain decomposition preconditioner for multiscale high-contrast problems. *Domain Decomposition Methods in Science and Engineering XIX, Huang, Y.; Kornhuber, R.; Widlund, O.; Xu, J. (Eds.)*, Volume 78 of Lecture Notes in Computational Science and Engineering, Springer-Verlag, 2011, Part 2, pp. 189-196.

[24] Y. Efendiev, J. Galvis and T. Y. Hou. Generalized Multiscale Finite Element Methods (GMsFEM). *J. Comput. Phys.*, 251:116–135, 2013.

[25] Y. Efendiev, J. Galvis, R. Lazarov, S. Margenov, and J. Ren. Robust two-level domain decomposition preconditioners for high-contrast anisotropic flows in multiscale media. *Comput. Methods Appl. Math.*, 12(4):415–436, 2012.

[26] Y. Efendiev, J. Galvis, R. Lazarov, M. Moon, and M. Sarkis. Generalized Multiscale Finite Element Method. Symmetric Interior Penalty Coupling. *J. Comput. Phys.*, 255:1–15, 2013.

[27] Y. Efendiev, J. Galvis, R. Lazarov, and J. Willems. Robust domain decomposition preconditioners for abstract symmetric positive definite bilinear forms. *ESAIM: Math. Modelling and Numer. Anal.*, 46:1175–1199, 2012.

[28] Y. Efendiev, J. Galvis, G. Li, and M. Presho. Generalized multiscale finite element methods. nonlinear elliptic equations. *Commun. Comput. Phys.*, 15:733–755, 2014.

[29] Y. Efendiev, J. Galvis, G. Li, and M. Presho. Generalized multiscale finite element methods. oversampling strategies. *International Journal for Multiscale Computational Engineering*, 12(6):465–484, 2014.

[30] Y. Efendiev, J. Galvis, and F. Thomines. A systematic coarse-scale model reduction technique for parameter-dependent flows in highly heterogeneous media and its applications. *Multiscale Model. Simul.*, 10(4):1317–1343, 2012.

[31] Y. Efendiev, J. Galvis and P. Vassielvski. Spectral element agglomerate algebraic multigrid methods for elliptic problems with high-Contrast coefficients. *Domain Decomposition Methods in Science and Engineering XIX, Huang, Y.; Kornhuber, R.; Widlund, O.; Xu, J. (Eds.)*, Volume 78 of Lecture Notes in Computational Science and Engineering, Springer-Verlag, 2011, Part 3, pp. 407-414.

[32] Y. Efendiev, J. Galvis and P. Vassielvski. Multiscale spectral AMGe solvers for high-contrast flow problems. *Institute for Scientific Computation*, Technical Report 2012-02, 2012.

[33] Y. Efendiev, J. Galvis, and X.H. Wu. Multiscale finite element methods for high-contrast problems using local spectral basis functions. *J. Comput. Phys.*, 230(4):937–955, 2011.

[34] Y. Efendiev, V. Ginting, T. Hou, and R. Ewing. Accurate multiscale finite element methods for two-phase flow simulations. *J. Comput. Phys.*, 220:155–174, 2006.

[35] Y. Efendiev and T. Hou. Multiscale finite element methods. Theory and applications. *Springer*, 2009.

[36] Y. Efendiev, T. Hou, and V. Ginting. Multiscale finite element methods for nonlinear problems and their applications. *Comm. Math. Sci.*, 2:553–589, 2004.

[37] Y. Efendiev, T. Y. Hou, and X. H. Wu. Convergence of a nonconforming multiscale finite element method. *SIAM J. Num. Anal.*, 37:888–910, 2000.

[38] J. Galvis and Y. Efendiev. Domain decomposition preconditioners for multiscale flows in high contrast media. *SIAM J. Multiscale Modeling and Simulation*, 8(4):1461–1483, 2010.

[39] J. Galvis and Y. Efendiev. Domain decomposition preconditioners for multiscale flows in high-contrast media: Reduced dimension coarse spaces. *SIAM J. Multiscale Modeling and Simulation*, 8(5):1621–1644, 2010.

[40] J. Galvis, G. Li, and K. Shi. A generalized multiscale finite element method for the brinkman equation. *Journal of Computational and Applied Mathematics*, 280:294–309, 2015.

[41] I. G. Graham, P. O. Lechner, and R. Scheichl. Domain decomposition for multiscale PDEs. *Numer. Math.*, 106(4):589–626, 2007.

[42] I. G. Graham and R. Scheichl. Robust domain decomposition algorithms for multiscale PDEs. *Numer. Methods Partial Differential Equations*, 23(4):859–878, 2007.

[43] H. Hajibeygi, D. Kavounis, and P. Jenny. A hierarchical fracture model for the iterative multiscale finite volume method. *Journal of Computational Physics*, 230(4):8729–8743, 2011.

[44] T. Y. Hou and X. H. Wu. A multiscale finite element method for elliptic problems in composite materials and porous media. *J. Comput. Phys.*, 134:169–189, 1997.

[45] P. Jenny, S. H. Lee, and H. A. Tchelepi. Multi-scale finite-volume method for elliptic problems in subsurface flow simulation. *J. Comput. Phys.*, 187:47–67, 2003.

[46] M. J. King, P. R. King, C. A. McGill, and J. K. Williams. Effective properties for flow calculations. *Transport in Porous Media*, 20:169–196, 1995.

[47] S. H. Lee, C. Wolfsteiner, and H. A. Tchelepi. Multiscale finite-volume formulation for multiphase flow in porous media: Black oil formulation of compressible, three-phase flow with gravity. *Comput. Geosci.*, 12:351–366, 2008.

[48] I. Lunati and P. Jenny. Multiscale finite-volume method for compressible multiphase flow in porous media. *J. Comput. Phys.*, 216:616–636, 2006.

[49] F. Marcondes and K. Sepehrnoori. An element-based finite-volume method approach for heterogeneous and anisotropic compositional reservoir simulation. *J. Pet. Sci. Eng.*, 73:99–106, 2010.

[50] J. Ren and M. Presho. A generalized multiscale finite element method for high-contrast single-phase flow problems in anisotropic media. *Journal of Computational and Applied Mathematics*, 277:202–214, 2015.

[51] N. Spillane, V. Dolean, P. Hauret, F. Nataf, C. Pechstein and R. Scheichl. A robust two level domain decomposition preconditioner for systems of PDEs. *Comptes Rendus Mathematique*, 349(23-24):1255–1259, 2011.

[52] A. Toselli and O. Widlund. Domain Decomposition Methods—Algorithms and Theory. *Vol. 34 of Springer Series in Comput. Mathematics*, Springer-Verlag, Berlin, 2005.

[53] J. Willems. Robust multilevel methods for general symmetric positive definite operators. *Johann Radon Institute for Computational and Applied Mathematics Technical Reports*, 12-06 (2011), 1–20.

[54] X. H. Wu, Y. Efendiev, and T. Y. Hou. Analysis of upscaling absolute permeability. *Discrete and Continuous Dynamical Systems - Series B*, 2:185–204, 2002.